The Astrophysical Journal Supplement Series, 243:3 (29pp), 2019 July https://doi.org/10.3847/1538-4365/ab22a8


# X-Ray Binary Luminosity Function Scaling Relations for Local Galaxies Based on Subgalactic Modeling

Bret D. Lehmer[1], Rafael T. Eufrasio[1], Panayiotis Tzanavaris[2,3], Antara Basu-Zych[2,3], Tassos Fragos[4], Andrea Prestwich[5], Mihoko Yukita[6], Andreas Zezas[5,7,8], Ann E. Hornschemeier[2,6], and Andrew Ptak[2,6]
[1] Department of Physics, University of Arkansas, 226 Physics Building, 825 West Dickson Street, Fayetteville, AR 72701, USA; lehmer@uark.edu
[2] NASA Goddard Space Flight Center, Code 662, Greenbelt, MD 20771, USA
[3] Center for Space Science and Technology, University of Maryland Baltimore County, 1000 Hilltop Circle, Baltimore, MD 21250, USA
[4] Geneva Observatory, Geneva University, Chemin des Maillettes 51, 1290 Sauverny, Switzerland
[5] Harvard-Smithsonian Center for Astrophysics, 60 Garden Street, Cambridge, MA 02138, USA
[6] The Johns Hopkins University, Homewood Campus, Baltimore, MD 21218, USA
[7] Foundation for Research and Technology-Hellas, 100 Nikolaou Plastira Street, 71110 Heraklion, Crete, Greece
[8] Physics Department & Institute of Theoretical & Computational Physics, P.O. Box 2208, 71003 Heraklion, Crete, Greece
*Received 2019 March 11; revised 2019 April 27; accepted 2019 May 11; published 2019 June 26*

## Abstract

We present new *Chandra* constraints on the X-ray luminosity functions (XLFs) of X-ray binary (XRB) populations, as well as their scaling relations, for a sample of 38 nearby galaxies ($D = 3.4$–$29$ Mpc). Our galaxy sample is drawn primarily from the *Spitzer* Infrared Nearby Galaxies Survey (SINGS) and contains a wealth of *Chandra* (5.8 Ms total) and multiwavelength data, allowing for star formation rates (SFRs) and stellar masses ($M_\star$) to be measured on subgalactic scales. We divided the 2478 X-ray-detected sources into 21 subsamples in bins of specific SFR ($\mathrm{sSFR} \equiv \mathrm{SFR}/M_\star$) and constructed XLFs. To model the XLF dependence on sSFR, we fit a global XLF model, containing contributions from high-mass XRBs (HMXBs), low-mass XRBs (LMXBs), and background sources from the cosmic X-ray background that respectively scale with SFR, $M_\star$, and sky area. We find an HMXB XLF that is more complex in shape than previously reported and an LMXB XLF that likely varies with sSFR, potentially due to an age dependence. When applying our global model to XLF data for each individual galaxy, we discover a few galaxy XLFs that significantly deviate from our model beyond statistical scatter. Most notably, relatively low-metallicity galaxies have an excess of HMXBs above $\approx 10^{38}$ erg s$^{-1}$, and elliptical galaxies that have relatively rich populations of globular clusters (GCs) show excesses of LMXBs compared to the global model. Additional modeling of how the XRB XLF depends on stellar age, metallicity, and GC specific frequency is required to sufficiently characterize the XLFs of galaxies.

*Key words:* galaxies: evolution – stars: formation – X-rays: binaries – X-rays: galaxies

*Supporting material:* machine-readable tables

## 1. Introduction

X-ray binaries (XRBs) provide a direct probe of compact object (i.e., black hole (BH) and neutron star (NS)) populations and close binary systems in galaxies. The XRB phase of close binary evolution results when mass is transferred from a normal star (secondary) to an accreting compact object remnant (primary), via Roche lobe overflow or stellar wind mass transfer. Depending on the binary parameters, subsequent evolution beyond the XRB phase is expected to result in a variety of astrophysical systems, including, e.g., gravitational-wave (GW) mergers, millisecond pulsars, and short gamma-ray bursts (GRBs). Recent discoveries of GWs from merging BHs and NSs from LIGO (e.g., Abbott et al. 2016, 2017) have prompted a resurgence in efforts to self-consistently model close binary populations and their evolution (e.g., Belczynski et al. 2016, 2018; Mandel & de Mink 2016; Marchant et al. 2017; Kruckow et al. 2018; Mapelli & Giacobbo 2018). As such, statistically meaningful constraints on XRB populations are critical to such efforts.

Thanks largely to data collected over the past two decades by *Chandra* and *XMM-Newton*, substantial insight has been gained into how the XRB phase is manifested within a variety of galactic environments beyond the Milky Way and Magellanic Clouds. Several studies of XRB emission from galaxies in the nearby universe ($D \lesssim 50$ Mpc) have established that the X-ray luminosity functions (XLFs) and population-integrated luminosities of high-mass XRBs (HMXBs) and low-mass XRBs (LMXBs) scale with star formation rate (SFR) and stellar mass ($M_\star$), respectively (e.g., Grimm et al. 2003; Ranalli et al. 2003; Colbert et al. 2004; Gilfanov 2004; Lehmer et al. 2010; Boroson et al. 2011; Mineo et al. 2012a, 2012b; Zhang et al. 2012). These scaling relations have been assumed to be "universal" in applications outside of studies focused on XRBs. For example, studies of distant active galactic nuclei (AGNs) routinely utilize local scaling relations when assessing the levels of XRB emission in distant populations (see, e.g., Section 2.2 of Hickox & Alexander 2018).

However, more recently it has been suggested that the scatter in basic XRB scaling relations would be larger than expected if the correlations were universal. XRB population synthesis models have indicated that universal scaling relations are unrealistic on physical grounds (e.g., Linden et al. 2010; Fragos et al. 2008, 2013a, 2013b; Zuo et al. 2014). For example, the population synthesis models from Fragos et al. (2013b) predict order-of-magnitude variations of $L_X(\mathrm{HMXB})/\mathrm{SFR}$ and $L_X(\mathrm{LMXB})/M_\star$ with metallicity and stellar age, respectively, over ranges of these quantities present in the observable universe.

Since the ranges of metallicities and mean stellar ages for typical galaxies in the local universe are relatively narrow,

empirically measuring the predicted deviations of the scaling relations with these parameters has been challenging. Nonetheless, targeted observations of relatively rare, low-metallicity late-type galaxies (e.g., Basu-Zych et al. 2013a, 2016; Douna et al. 2015; Brorby et al. 2016; Tzanavaris et al. 2016) and early-type galaxies with a range of stellar ages (e.g., Kim & Fabbiano 2010; Lehmer et al. 2014) have provided tantalizing evidence of variations in the scaling relations in line with those predicted by population synthesis models. New studies of XRB formation rates within very nearby galaxies (e.g., Magellanic Clouds, M33, M51, NGC 3310, and NGC 2276) have revealed similar variations with physical properties on subgalactic scales (e.g., Antoniou & Zezas 2016; Lehmer et al. 2017; Garofali et al. 2018; Anastasopoulou et al. 2019; Antoniou et al. 2019). Furthermore, X-ray stacking analyses of distant galaxy populations in deep *Chandra* surveys (e.g., the *Chandra* Deep Fields and *Chandra* COSMOS surveys) have claimed that there is redshift evolution in the scaling relations, potentially due to the corresponding decline in mean stellar population age and metallicity with lookback time (e.g., Lehmer et al. 2007, 2016; Basu-Zych et al. 2013b; Kaaret 2014; Aird et al. 2017).

The measured evolution of $L_{\rm X}({\rm HMXB})/{\rm SFR} \propto (1+z)$ and $L_{\rm X}({\rm LMXB})/M_\star \propto (1+z)^{2-3}$ out to $z \approx 2$–4 (Lehmer et al. 2016; Aird et al. 2017) is only loosely constrained, but consistent with the population synthesis predictions from Fragos et al. (2013a); however, see Fornasini et al. (2018) for caveats. Extrapolation of the theoretical predictions into the very early universe at $z \gtrsim 10$, when the universe was of very low metallicity ($\lesssim 1/10\,Z_\odot$, e.g., based on the Millenium II simulations; Guo et al. 2011), indicates that XRBs were likely the most luminous X-ray-emitting population in the universe (e.g., Fragos et al. 2013b; Lehmer et al. 2016; Madau & Fragos 2017). In fact, emission from XRBs is thought to play a dominant role in heating the IGM at $z \approx 10$–20 (e.g., Mirabel et al. 2011; Mesinger et al. 2013; Pacucci et al. 2014; Das et al. 2017; Greig & Mesinger 2018).

The studies outlined above indicate that XRBs play an important role in a variety of astrophysical systems and that the XRB scaling relations have non-negligible dependencies on galaxy physical properties. Although we now have some indications of how the XRB emission and scaling relations vary with important physical properties, there is still large uncertainty in how the *distributions* of XRB populations (i.e., XLFs) vary with these physical properties. In particular, we do not know precisely how the XRB XLFs vary with age and metallicity. There are some indications that the HMXB XLF in low-metallicity galaxies contains an excess of ultraluminous X-ray sources (ULXs) above $10^{39}$ erg s$^{-1}$ (Mapelli et al. 2010; Kaaret et al. 2011; Prestwich et al. 2013; Basu-Zych et al. 2016) and the bright end of the LMXB XLF for young elliptical galaxies contains more LMXBs with $\gtrsim 10^{39}$ erg s$^{-1}$ than older ellipticals (e.g., Kim & Fabbiano 2010; Lehmer et al. 2014, 2017). But for both HMXBs and LMXBs, it is not clear whether there is an excess of XRBs over the full range of luminosities that are important to the galaxy-wide global X-ray power output, and to what extent these populations are elevated (due to small number statistics). These details are powerful constraints for population synthesis models, as they provide several additional degrees of freedom for modeling XRB populations, beyond scalings with integrated $L_{\rm X}$.

The most recent large-scale measurements of the XRB XLFs and their scalings with galaxy properties have employed a strategy of selecting galaxy samples with high specific SFR (sSFR $\equiv$ SFR$/M_\star$) to isolate HMXB populations (Mineo et al. 2012b, hereafter M12; Sazonov & Khabibullin 2017a, 2017b) and elliptical galaxy populations that lack HMXBs to isolate LMXB populations (Zhang et al. 2012; hereafter Z12; Peacock et al. 2017). By design, such a strategy excludes data from more representative populations of galaxies that are likely to have a mix of populations and has the potential to yield misleading results for a number of physical reasons. For example, late-type galaxies generally have younger mean stellar ages and could have larger contributions from LMXBs than elliptical galaxies, since the LMXB emission per unit mass is expected to decline with increasing age (e.g., Fragos et al. 2008). Similarly, massive elliptical galaxies, which dominate studies of LMXB scaling relations, tend to have larger numbers of globular clusters (GCs) per unit mass than lower-mass late-type galaxies (e.g., Brodie & Strader 2006). GCs very efficiently produce LMXBs through dynamical interactions (Clark 1975; Fabian et al. 1975; Sivakoff et al. 2007; Cheng et al. 2018a, 2018b) and can even dominate the LMXB population of massive ellipticals (e.g., Irwin 2005; Kim et al. 2009; Voss et al. 2009; Lehmer et al. 2014) and produce XLFs that are different in shape from those of the LMXB population found in the galactic field.

In this paper, we delve into the *Chandra* archive of local ($D \lesssim 30$ Mpc) galaxies to establish XRB XLF correlations with physical properties that are representative of the local galaxy population that makes up most of the mass of the local universe (e.g., Blanton & Moustakas 2009). We make use of 5.8 Ms of *Chandra* ACIS imaging data across 38 galaxies to simultaneously constrain the HMXB and LMXB XLF shapes and scalings with SFR and $M_\star$, respectively. We employ a galaxy decomposition technique, developed in Lehmer et al. (2017), to statistically extract the contributions from HMXBs, LMXBs, and unrelated background sources (e.g., AGNs and Galactic stars). This technique uses spatially resolved maps of SFR and $M_\star$ for the galaxies in our sample to extract XRB population statistics from a range of local sSFRs and then self-consistently models the XRB XLFs across the entire sSFR range.

Our goal here is to establish a baseline XLF model, for which we can compare observed XLFs of other galaxies and identify outliers to study in more detail. Furthermore, in subsequent studies we will expand our sample and will investigate quantitatively how metallicity, stellar age, and GC populations influence the XRB XLFs. Our paper is organized as follows. In Section 2, we discuss the galaxy sample selection. In Section 3, we outline our analysis procedures for constructing maps of SFR and $M_\star$, as well as our detailed X-ray data reduction and point-source cataloging procedure. In Section 4, we present the XLFs for our galaxies and culled regions selected by sSFR and provide model fits to the XLFs. In Section 5, we make comparisons of our HMXB and LMXB XLFs with past observational estimates and XRB population synthesis models, identify interesting galaxies with XRB populations that are outliers to the average, and discuss possible physical trends that explain these deviations. We also characterize the galaxy-to-galaxy scatter of the integrated XRB luminosity implied by our XLFs. Finally, we summarize our

results in Section 6. Full catalogs of the *Chandra* sources are available in the online Journal, and the *Chandra* images, as well as our SFR and $M_\star$ maps, are provided publicly[9] and archived in Zenodo [doi:10.5281/zenodo.2875827].

## 2. Galaxy Sample Selection and Properties

We started by selecting a sample of nearby galaxies with *Chandra* coverage, as well as far-UV to IR multiwavelength data that were sufficient for measuring accurate SFR and $M_\star$ values on subgalactic scales. To this end, we searched for galaxies in the *Spitzer* Infrared Nearby Galaxies Survey (SINGS; Kennicutt et al. 2003) that also contained *Chandra* ACIS imaging data in the archive. The SINGS sample itself contains 75 nearby ($\lesssim$30 Mpc) galaxies, which were selected to be diverse in properties and were well resolved and efficiently observed by *Spitzer* and other multiwavelength facilities (covering angular sizes of 5′–15′). We first limited our search to galaxies with $B$-band absolute magnitudes of $M_B < -19$ mag (as provided by Moustakas et al. 2010), which includes galaxies that are $\approx$1 mag below the knee of the $B$-band luminosity function and are in the range of galaxies that dominate the stellar mass density of the local universe (e.g., Blanton et al. 2003). We further restricted our sample to galaxies with inclinations to our line of sight that are $\lesssim$70°. Inclination, $i$, was estimated as $\sin(i) = \sqrt{1 - (b/a)^2}$, where $a$ and $b$ are the semimajor and semiminor axes, as defined in the $K_s$ band by Jarrett et al. (2003). This criterion is motivated by the fact that extinction due to a thin disk rapidly increases for inclinations above this value (e.g., Tuffs et al. 2004). Since we are unable to accurately correct for intrinsic extinction for the point sources, and we expect that this extinction could have substantial effects on the observed XLFs, we have elected to exclude these galaxies.

The above selection resulted in 45 SINGS galaxies, with 36 of them having sufficient *Chandra* data. In addition to these galaxies, we elected to add to our sample NGC 5236 (M83) and NGC 5474 (M101), both of which have properties consistent with those selected in the SINGS galaxy sample and also have outstanding X-ray coverage due to large *Chandra* campaigns (Kuntz & Snowden 2010; Long et al. 2014). We note that the overall selection of galaxies is driven by the presence of excellent multiwavelength data mainly available through SINGS. The SINGS sample has 80% *Chandra* completeness, with many of the galaxies being observed owing to their SINGS coverage (e.g., via the XSINGS program; PI: L. Jenkins; Tzanavaris et al. 2013), suggesting that our sample is not significantly biased toward X-ray-bright galaxies. In total, our final sample contains 38 nearby galaxies.

In Figure 1, we show cutout optical images of the galaxy sample, and in Table 1 we summarize the basic properties of each galaxy. Here we are interested in XLF scaling relations with the basic properties: SFR and $M_\star$. Calculations of galaxy-wide SFR and $M_\star$ values for our sample are detailed in Section 3.1 below, and in Figure 2(a) we graphically show their values on the SFR–$M_\star$ plane. Our sample spans 2.5 dex in SFR and $M_\star$, and by design these galaxies were chosen to be diverse and do not strictly follow the galaxy "main sequence" (e.g., Elbaz et al. 2007; Noeske et al. 2007; Karim et al. 2011; Whitaker et al. 2014).

[9] https://lehmer.uark.edu/downloads/

Since we expect that the HMXB-to-LMXB ratio will be dependent on sSFR, this quantity is of particular interest. In Figure 2(b) we show the distribution of galaxy-wide sSFR (i.e., total galaxy SFR/$M_\star$) values for the 38 galaxies in our sample. Past studies have shown that around sSFR $\approx 10^{-10}$ yr$^{-1}$ the relative X-ray luminosities from HMXBs and LMXBs are nearly equal, while at higher and lower sSFR values HMXBs and LMXBs, respectively, dominate the XRB population luminosities (see, e.g., Colbert et al. 2004; Lehmer et al. 2010; M12). Our galaxy sample contains 15 and 23 galaxies, respectively, above and below this threshold, with the most extreme cases being NGC 337 (sSFR $\approx 5 \times 10^{-10}$ yr$^{-1}$) and NGC 1404 (sSFR $\approx 10^{-12}$ yr$^{-1}$). As we will show below, we can quantify the HMXB and LMXB contributions to the XLFs of all late-type galaxies based on a self-consistent "global" model of the HMXB and LMXB XLF scaling with SFR and $M_\star$, respectively.

## 3. Data Analysis and Products

### 3.1. Multiwavelength Tracer Maps

For each galaxy in our sample, we generated SFR and $M_\star$ maps, using multiwavelength tracers of these quantities. For SFR, we made use of FUV *GALEX* and 24 $\mu$m *Spitzer* maps, and for $M_\star$, we utilized $K$-band data from the Two Micron All Sky Survey (2MASS) combined with optical $g$- and $i$-band data from the Sloan Digital Sky Survey (SDSS), when available. In the absence of SDSS, we utilized $B$- and $V$-band data available from the SINGS Collaboration,[10] which originated from either the Kitt Peak National Observatory (KPNO) or Cerro Tololo Inter-American Observatory (CTIO), or in the case of NGC 6946, we made use of $B$- and $V$-band data from *Swift*. Our data preparation procedure, including the identification and subtraction of foreground Galactic stars, background subtraction, and convolution techniques, followed closely that outlined in Sections 2.1–2.4 of Eufrasio et al. (2017) with a few minor differences. All images were convolved to a common Gaussian point-spread function (PSF) with a 15″ FWHM, which is significantly larger than the 24 $\mu$m PSF to comfortably remove all PSF features and produce a Gaussian PSF. The images were projected to a common pixel scale of 3″ pixel$^{-1}$. For a galaxy at 30 Mpc, just beyond the most distant galaxy in our sample, this pixel scale results in a physical size of 436 pc pixel$^{-1}$.

To calculate SFRs, we made use of the Hao et al. (2011) relation (implied by their Table 3):

$$\left(\frac{\mathrm{SFR}}{M_\odot\ \mathrm{yr}^{-1}}\right) = 1.6 \times 10^{-10}\left[\left(\frac{L_{\mathrm{FUV}}^{\mathrm{obs}}}{L_\odot}\right) + 3.89\left(\frac{L_{24\,\mu\mathrm{m}}^{\mathrm{obs}}}{L_\odot}\right)\right], \quad (1)$$

where $L_{\mathrm{FUV}}^{\mathrm{obs}}$ and $L_{24\,\mu\mathrm{m}}^{\mathrm{obs}}$ are the observed (i.e., corrected only for Galactic extinction and not intrinsic extinction) monochromatic luminosities (e.g., $\nu L_\nu$) at 1528 Å and 24 $\mu$m, respectively. For each pixel, values of $L_{\mathrm{FUV}}^{\mathrm{obs}}$ and $L_{24\,\mu\mathrm{m}}^{\mathrm{obs}}$ are determined from the *GALEX* FUV and *Spitzer* 24 $\mu$m maps, respectively. In the case of NGC 7552, *Herschel* 70 $\mu$m data were used instead of the *Spitzer* 24 $\mu$m data, due to strong PSF contributions from the 24 $\mu$m bright nuclear starburst at large galactocentric radii. For this galaxy, we converted $L_{70}^{\mathrm{obs}}$ to $L_{24}^{\mathrm{obs}}$, using scaling relations from Kennicutt & Evans (2012) and Galametz et al. (2013).

[10] https://irsa.ipac.caltech.edu/data/SPITZER/SINGS/doc/sings_fifth_delivery_v2.pdf

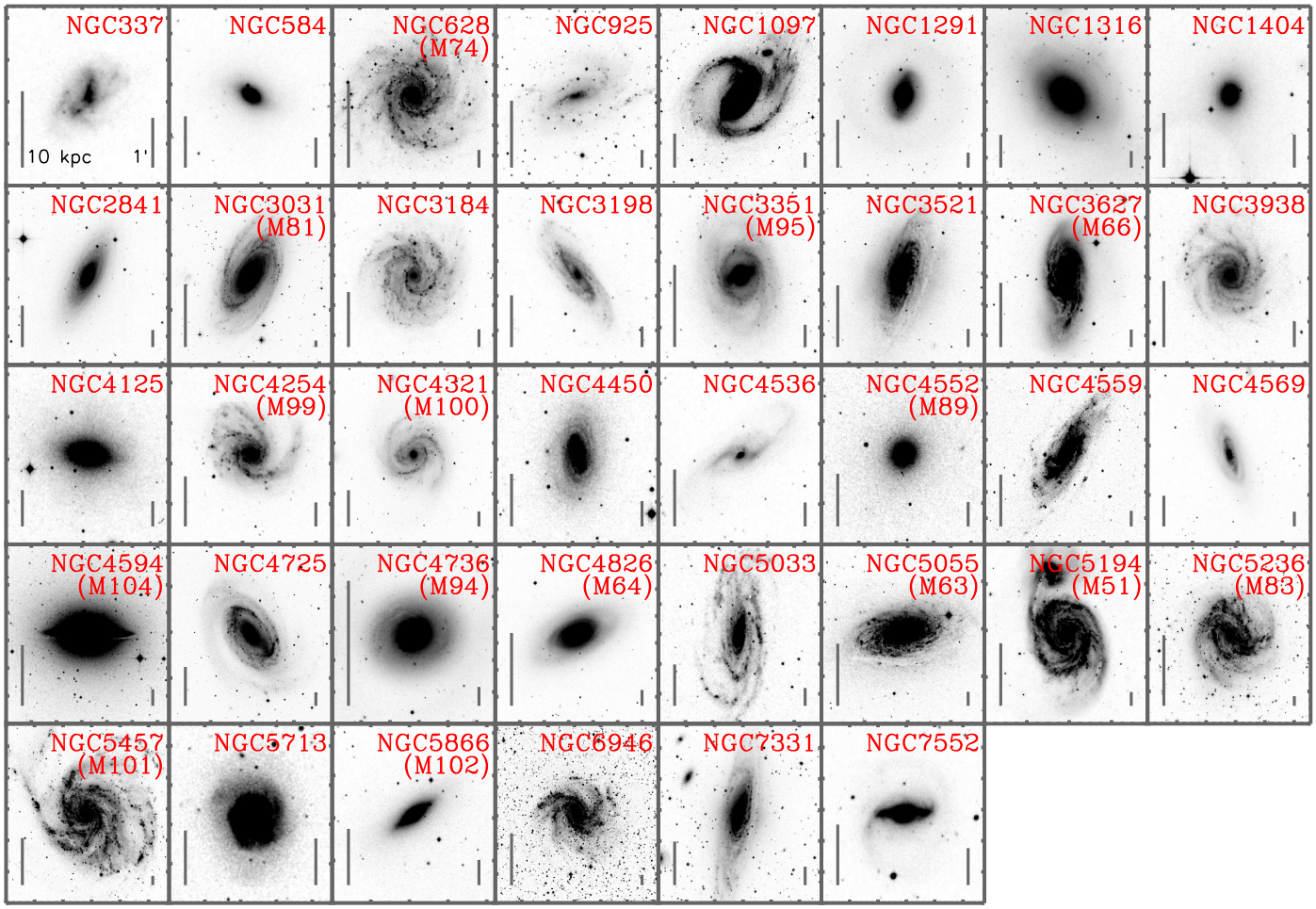


**Figure 1.** Digitized Sky Survey (DSS) images of the 38 galaxies in our sample. All images have square dimensions, with the length of each side being equal to 1.1 times the total $K_s$-band major axis (as reported by Jarrett et al. 2003). For reference, vertical bars of size 10 kpc and 1′ are provided in the lower left and lower right corners of each panel, respectively.

These SFRs are based on an assumed constant star formation history with duration of 100 Myr, a Kroupa (2001) initial mass function (IMF), and solar metallicity (i.e., $Z = 0.02$). The calibration is reported to have a $1\sigma$ uncertainty of 0.1 dex.

Stellar masses ($M_\star$) were computed following the relations in Zibetti et al. (2009; see their Table B1):

$$\log(M_\star/M_\odot) = \log(L_K/L_{K,\odot}) - 1.321 + 0.754(g-i), \quad (2)$$

$$\log(M_\star/M_\odot) = \log(L_K/L_{K,\odot}) - 1.390 + 1.176(B-V). \quad (3)$$

We utilized Equation (2) for 30 of our galaxies, and this was our preferred calibration. Equation (3) was applied for the remaining eight galaxies in our sample. Both equations are reported to have $1\sigma$ calibration uncertainties of $\approx$0.13 dex. For 17 of the galaxies, both $g-i$ and $B-V$ colors were available. We generated maps based on both calibrations and found good agreement between tracers and consistent with the uncertainty in the Zibetti et al. (2009) calibration.

### 3.2. Chandra *Data Reduction and Catalog Production*

For our X-ray point-source measurements, we use *Chandra* ACIS imaging data (both ACIS-S and ACIS-I) of the galaxies in our sample. In Table 2, we tabulate the full *Chandra* observing log used in this paper. We restricted our analyses to *Chandra* data sets that had aim points within 5′ of the central coordinates of the galaxy. This restriction ensures that the ObsID combined images reach deep limits with a sharp PSF ($\lesssim$1.″5 90% encircled counts fraction (ECF) radii) in the central nuclear regions of the galaxies, where source confusion could potentially be problematic. Some of the galaxies in our sample have much more extensive archives than we utilize here. For example, for M81, we make use of only 18 of the 27 ObsIDs that were available in the archive, as a result of us excluding observations from a large program to observe the periphery of the galaxy (PI: D. Swartz).

Our *Chandra* data reduction was carried out using CIAO v. 4.8 with `CALDB` v. 4.7.1,[11] and our procedure followed closely the methods outlined in Section 2.2 of Lehmer et al. (2017). Briefly, we (1) reprocessed pipeline products using the `chandra_repro` script; (2) removed bad pixels and columns and filtered the events list to include only good time intervals without significant ($>3\sigma$) flares above the background level; (3) when applicable, aligned events lists and aspect histograms, via `wcs_match` and `wcs_update`, to the deepest *Chandra* ObsID for a given galaxy, using small translations (median shifts and $1\sigma$ standard deviations of $\delta$R.A. $= 0.''16 \pm 0.''14$ and $\delta$decl. $= 0.''16 \pm 0.''18$); (4) constructed merged events lists and

[11] http://cxc.harvard.edu/ciao/

**Table 1**
Nearby Galaxy Sample and Properties

| Galaxy | | | Central Position | | | Size Parameters | | | | | | | | |
|---|---|---|---|---|---|---|---|---|---|---|---|---|---|---|
| Name (NGC) (1) | Alt. Name (2) | Morph. Type (3) | $\alpha_{J2000}$ (4) | $\delta_{J2000}$ (5) | $D$ (Mpc) (6) | $a$ (arcmin) (7) | $b$ (arcmin) (8) | PA (deg) (9) | $r_{remove}$ (arcsec) (10) | SFR ($M_\odot$ yr$^{-1}$) (11) | log $M_\star$ ($M_\odot$) (12) | log sSFR (yr$^{-1}$) (13) | 12 + log [O/H] (dex) (14) | $S_N$ (15) |
| 337 | ⋯ | SBd | 00 59 50.1 | −07 34 40.7 | 22.40 ± 2.30 | 0.87 | 0.49 | −22.5 | 0 | 1.09 | 9.32 | −9.28 | 8.44 ± 0.07 | … |
| 584 | ⋯ | E4 | 01 31 20.8 | −06 52 05.0 | 20.10 ± 1.90 | 1.47 | 0.91 | 62.5 | 0 | 0.05 | 10.48 | −11.77 | 8.75* | 1.69 ± 0.67 |
| 628 | M74 | SAc | 01 36 41.8 | +15 47 00.5 | 7.30 ± 1.40 | 2.10 | 1.80 | 87.5 | 3 | 0.33 | 9.48 | −9.96 | 8.54 ± 0.15 | … |
| 925 | ⋯ | SABd | 02 27 16.9 | +33 34 44.0 | 9.12 ± 0.17 | 1.87 | 0.82 | −75.0 | 0 | 0.18 | 9.03 | −9.78 | 8.38 ± 0.15 | … |
| 1097 | ⋯ | SBb | 02 46 19.1 | −30 16 29.7 | 17.10 ± 2.30 | 2.63 | 1.44 | −35.0 | 5 | 4.51 | 10.76 | −10.11 | 8.83 ± 0.05 | … |
| 1291 | ⋯ | SB0/a | 03 17 18.6 | −41 06 29.1 | 10.80 ± 2.30 | 2.39 | 1.70 | −10.0 | 3 | 0.08 | 10.81 | −11.89 | 9.20* | … |
| 1316 | ⋯ | SAB0 | 03 22 41.8 | −37 12 29.5 | 21.50 ± 1.70 | 2.77 | 1.99 | 47.5 | 3 | 0.49 | 11.48 | −11.79 | 9.52* | 0.54 ± 0.27 |
| 1404 | ⋯ | E1 | 03 38 51.9 | −35 35 39.8 | 20.80 ± 1.70 | 1.38 | 1.24 | −17.5 | 3 | 0.10 | 10.98 | −11.99 | 9.21* | 1.78 ± 0.32 |
| 2841 | ⋯ | SAb | 09 22 02.7 | +50 58 35.3 | 14.10 ± 1.50 | 3.02 | 1.36 | −30.0 | 0 | 0.61 | 10.67 | −10.89 | 8.89 ± 0.05 | … |
| 3031 | M81 | SAab | 09 55 33.2 | +69 03 54.9 | 3.55 ± 0.13 | 8.13 | 4.14 | −31.0 | 12 | 0.25 | 10.39 | −10.98 | 8.60 ± 0.09 | 1.11 ± 0.37 |
| 3184 | ⋯ | SABcd | 10 18 17.0 | +41 25 27.8 | 11.10 ± 1.90 | 1.91 | 1.62 | 117.5 | 0 | 0.48 | 9.68 | −10.00 | 8.75 ± 0.12 | … |
| 3198 | ⋯ | SBc | 10 19 55.0 | +45 32 58.9 | 13.68 ± 0.50 | 1.91 | 0.67 | 40.0 | 0 | 0.55 | 9.70 | −9.96 | 8.43 ± 0.15 | … |
| 3351 | M95 | SBb | 10 43 57.7 | +11 42 13.0 | 9.33 ± 0.39 | 1.94 | 1.71 | −17.0 | 0 | 0.57 | 9.95 | −10.19 | 9.21 ± 0.05 | … |
| 3521 | ⋯ | SABbc | 11 05 48.6 | −00 02 09.2 | 10.10 ± 2.30 | 2.74 | 1.40 | −14.5 | 0 | 1.43 | 10.41 | −10.25 | 8.74 ± 0.09 | … |
| 3627 | M66 | SABb | 11 20 15.0 | +12 59 28.6 | 9.38 ± 0.35 | 3.08 | 1.70 | 6.5 | 3 | 1.83 | 10.30 | −10.04 | 8.66 ± 0.11 | … |
| 3938 | ⋯ | SAc | 11 52 49.5 | +44 07 14.6 | 13.40 ± 2.30 | 1.30 | 1.23 | 28.5 | 0 | 0.58 | 9.64 | −9.88 | 8.74* | … |
| 4125 | ⋯ | E6 pec | 12 08 06.0 | +65 10 26.9 | 23.90 ± 2.80 | 1.76 | 1.11 | 82.5 | 0 | 0.13 | 10.84 | −11.73 | 9.30* | … |
| 4254 | M99 | SAc | 12 18 49.6 | +14 24 59.4 | 16.50 ± 0.60 | 1.70 | 1.62 | 23.5 | 0 | 3.17 | 10.21 | −9.71 | 8.77 ± 0.11 | … |
| 4321 | M100 | SABbc | 12 22 54.9 | +15 49 20.6 | 14.32 ± 0.46 | 2.51 | 1.96 | −72.5 | 0 | 2.04 | 10.24 | −9.93 | 8.81 ± 0.07 | … |
| 4450 | ⋯ | SAab | 12 28 29.6 | +17 05 05.3 | 16.50 ± 0.60 | 1.87 | 1.18 | 2.5 | 3 | 0.19 | 10.40 | −11.12 | 8.82* | … |
| 4536 | ⋯ | SABbc | 12 34 27.1 | +02 11 16.4 | 14.45 ± 0.27 | 1.89 | 0.98 | −85.0 | 0 | 1.88 | 10.13 | −9.86 | 8.45 ± 0.23 | … |
| 4552 | M89 | E | 12 35 39.9 | +12 33 21.7 | 15.92 ± 0.81 | 1.48 | 1.39 | −30.0 | 3 | 0.08 | 10.54 | −11.66 | 8.83* | 7.68 ± 1.40 |
| 4559 | ⋯ | SABcd | 12 35 57.7 | +27 57 35.1 | 10.30 ± 2.30 | 2.04 | 0.96 | −32.5 | 0 | 0.45 | 9.34 | −9.68 | 8.40 ± 0.13 | … |
| 4569 | ⋯ | SABab | 12 36 49.8 | +13 09 46.3 | 16.50 ± 0.60 | 2.75 | 1.10 | 15.0 | 2 | 1.06 | 10.48 | −10.45 | 9.26* | … |
| 4594 | M104 | SAa | 12 39 59.5 | −11 37 23.1 | 9.33 ± 0.34 | 3.36 | 1.82 | 87.5 | 3 | 0.18 | 10.86 | −11.59 | 9.22* | 2.70 ± 0.28 |
| 4725 | ⋯ | SABab pec | 12 50 26.6 | +25 30 02.7 | 11.91 ± 0.33 | 2.91 | 1.51 | 50.0 | 0 | 0.37 | 10.38 | −10.81 | 8.79 ± 0.08 | … |
| 4736 | M94 | SAab | 12 50 53.1 | +41 07 12.5 | 5.20 ± 0.43 | 2.87 | 2.27 | 85.0 | 0 | 0.50 | 10.13 | −10.43 | 8.72 ± 0.04 | … |
| 4826 | M64 | SAab | 12 56 43.7 | +21 40 57.6 | 7.48 ± 0.69 | 3.58 | 2.04 | −70.0 | 0 | 0.42 | 10.41 | −10.79 | 9.24 ± 0.04 | … |
| 5033 | ⋯ | SAc | 13 13 27.5 | +36 35 37.1 | 14.80 ± 2.30 | 1.79 | 0.80 | −5.0 | 5 | 0.84 | 10.37 | −10.44 | 8.55 ± 0.13 | … |
| 5055 | M63 | SAbc | 13 15 49.3 | +42 01 45.4 | 7.80 ± 2.30 | 3.40 | 1.97 | −82.5 | 0 | 0.94 | 10.26 | −10.29 | 8.80 ± 0.10 | … |
| 5194 | M51 | SABbc pec | 13 29 52.7 | +47 11 42.9 | 8.58 ± 0.10 | 3.29 | 2.24 | 57.5 | 3 | 2.61 | 10.24 | −9.83 | 8.87 ± 0.11 | 0.76 ± 0.15 |
| 5236 | M83 | SABc | 13 37 00.9 | −29 51 56.7 | 4.66 ± 0.33 | 5.21 | 4.01 | 45.0 | 0 | 2.48 | 10.33 | −9.94 | 8.95 ± 0.03‡ | 0.17 ± 0.05 |
| 5457 | M101 | SABcd | 14 03 12.5 | +54 20 55.5 | 6.81 ± 0.03 | 3.94 | 3.90 | 28.5 | 0 | 1.07 | 9.91 | −9.88 | 9.10 ± 0.08‡ | 0.43 ± 0.11 |
| 5713 | ⋯ | SABbc pec | 14 40 11.5 | −00 17 21.2 | 29.40 ± 2.30 | 0.90 | 0.89 | −20.0 | 0 | 5.48 | 10.15 | −9.41 | 8.63 ± 0.06 | … |
| 5866 | M102 | S0 | 15 06 29.6 | +55 45 47.9 | 15.42 ± 0.85 | 1.86 | 0.78 | −57.0 | 0 | 0.14 | 10.46 | −11.32 | 8.81* | 1.37 ± 0.26 |
| 6946 | ⋯ | SABcd | 20 34 52.3 | +60 09 13.2 | 6.80 ± 1.70 | 4.21 | 2.95 | 52.5 | 0 | 2.46 | 10.01 | −9.61 | 8.66 ± 0.11 | 0.29 ± 0.13 |
| 7331 | ⋯ | SAb | 22 37 04.1 | +34 24 57.3 | 14.52 ± 0.60 | 2.60 | 1.27 | −12.5 | 0 | 2.12 | 10.75 | −10.42 | 8.73 ± 0.05 | 0.43 ± 0.27 |
| 7552 | ⋯ | SBab | 23 16 10.8 | −42 35 05.4 | 21.00 ± 2.30 | 1.27 | 0.75 | −85.0 | 15 | 3.58 | 10.04 | −9.48 | 8.85 ± 0.01 | … |
| Total | … | … | … | … | … | … | … | … | … | 45.4 | 12.10 | −10.44 | … | … |

**Note.** Col. (1): NGC number of galaxy. Col. (2): alternative Messier designation, if applicable. Col. (3): morphological type as provided in the Third Reference Catalog of Bright Galaxies (RC3; de Vaucouleurs et al. 1991). Cols. (4) and (5): R.A. and decl. of the galactic center based on the 2MASS positions derived by Jarrett et al. (2003). Col. (6): adopted distance and 1$\sigma$ error in units of Mpc. Distances were adopted from the SINGS values provided from Col. (9) of Table 1 in Moustakas et al. (2010), except for NGC 5194, NGC 5236, and NGC 5457, which were provided by McQuinn et al. (2016), Tully et al. (2013), and Nataf (2015), respectively. Cols. (7)–(9): $K_s$-band isophotal ellipse parameters, including, respectively, semimajor axis, $a$, semiminor axis, $b$, and position angle east from north, PA. The ellipses estimate the 20 mag arcsec$^{-2}$ surface brightness contour of each galaxy (derived by Jarrett et al. 2003). Col. (10): radius of central region removed from the galaxy due to either the presence of an AGN or extreme crowding. Cols. (11)–(13): SFR, $M_\star$, and sSFR values derived using the maps described in Section 3.1, and corresponding to areal coverage within the regions defined by Cols. (7)–(10) (i.e., with contributions from $r_{remove}$ excluded). Col. (14): estimated average oxygen abundances, 12 + log [O/H], from Moustakas et al. (2010), except for M83 and M101, which are based on the central metallicities from Bresolin et al. (2009) and Hu et al. (2018), respectively (denoted as ‡). Most oxygen abundances are based on strong line indicators, with the exception of those denoted with asterisks, which are from the optical luminosity–metallicity correlation. For consistency with other studies of XRB scaling relations that include metallicity, we have converted the Moustakas et al. (2010) abundances based on the Kobulnicky & Kewley (2004; KK04) calibration to the Pettini & Pagel (2004; PP04) calibration following the prescriptions in Kewley & Ellison (2008). Col. (15): GC specific frequency, $S_N$, as reported by Harris et al. (2013).

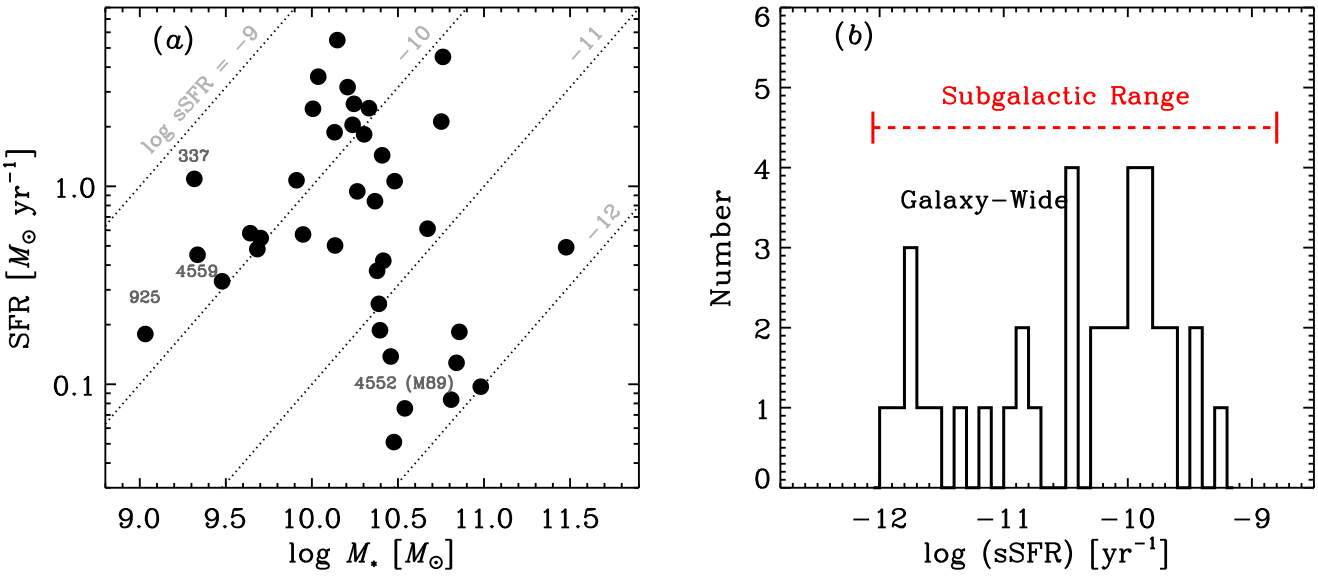


**Figure 2.** (a) Galaxy-wide SFR vs. $M_\star$ for the 38 galaxies in our sample. Dotted lines show locations of objects with log sSFR (yr$^{-1}$) = −9, −10, −11, and −12 (see annotations). (b) Distribution of sSFR values for whole galaxies (solid black histogram; see Section 2) and range of subgalactic regions used (dashed horizontal bar; see Section 4.2). As expected, the range of environments is broader for the subgalactic regions, allowing us to more cleanly probe how the XRB luminosity function varies with sSFR.

astrometric solutions using the `merge_obs` script; and (5) created additional products, including images, exposure maps, and exposure-weighted PSF maps with a 90% ECF, appropriate for the 0.5–2 keV, 2–7 keV, and 0.5–7 keV bands, which we hereafter refer to as the soft band (SB), hard band (HB), and full band (FB), respectively.

Merged 0.5–7 keV images were searched using `wavdetect` at a false-positive probability threshold of $1 \times 10^{-6}$ over seven wavelet scales from 1 to 8 pixels in a $\sqrt{2}$ sequence (i.e., 1, $\sqrt{2}$, 2, $2\sqrt{2}$, 4, $4\sqrt{2}$, and 8 pixels). We ran `wavdetect` using the merged exposure maps and 90% ECF PSF maps, which resulted in an initial source catalog with properties (e.g., positions and counts) appropriate for point sources. We inspected images from the three bands (i.e., SB, HB, and FB) by eye with source candidates indicated to ensure that this process produced sensible source candidates. We found in the case of M81 that several sources were identified along read-out streaks associated with the piled-up central AGN. Unless the sources were obviously real (based on having spatial count distributions consistent with the PSF and clear multiband detections), the sources along these streaks were removed from further consideration. Finally, for 14 galaxies, we found that point-source crowding in the central region of the galaxy (near the galactic nuclei) was prohibitively large (e.g., NGC 7552), or the central AGN was bright (e.g., M81). In such cases, we identified circular regions around these sources, within which we excluded the sources, as well as the SFR and $M_\star$ contributions, from our X-ray luminosity function analyses (see Col. 10 of Table 1). For completeness, these X-ray sources are included in our catalogs, with a flag indicating that the source was excluded from our analyses for the above reasons.

Source photometry was computed for all sources using the `ACIS Extract` (`AE`) v. 2016sep22 software package (Broos et al. 2010, 2012).[12] `AE` extracts source events and exposure times from all pixels that have exposure within polygonal regions that nominally trace the ≈90% ECF. These polygonal contours are constructed by `AE`, for each source, using 1.497 keV PSFs generated by the `MARX` v. 5.3.2[13] ray-tracing code. In a number of cases, the 90% polygonal regions overlapped, and `AE` iteratively generated nonoverlapping polygonal regions that encompassed a smaller fraction of the PSF and kept track of those PSF fractions. Local background events files were extracted by `AE` by first masking the source events within a circular masking region that is 1.1× the size of the 99.9% ECF at 1.497 keV and then extracting events from a larger circular aperture centered around the sources. The larger circular aperture size is determined by requiring that the summed exposure map value of the background pixels (i.e., those not masked), $T_{\rm bkg}$, is 5–10 times that determined for the source extraction pixels, $T_{\rm src}$, and also contains a minimum number of 5 counts. The latter criterion is generally met for $T_{\rm bkg} = 5 \times T_{\rm src}$, but if it is not, then the background aperture is increased up until $T_{\rm bkg} = 10 \times T_{\rm src}$, regardless of whether the aperture contains 5 counts or more.

For sources near the `wavdetect` threshold, we found that the `AE` photometry would sometimes provide negative counts in the detection bandpass. Instead of reevaluating the significance of these sources with `AE` and culling low-significance sources from the catalog, we chose to include them and utilize the `wavdetect` photometry. The primary reason for such discrepancies is likely due to the fact that `AE` evaluates photometry based on events within the 90% ECF, while `wavdetect` uses wavelets of various scales to identify sources (sometimes based on scales smaller than the 90% ECF) and reconstructs a model of the source counts. Thus, `wavdetect` will be somewhat more sensitive than `AE` in identifying sources when only the core of the PSF is significant compared to the background. Our choice to keep the low-significance sources is also motivated by our later use of `wavdetect` in calculating the completeness of a given galaxy's detected sources as a function of counts and location,

[12] The `ACIS Extract` software package and User's Guide are available at http://www.astro.psu.edu/xray/acis/acis_analysis.html.

[13] http://space.mit.edu/ASC/MARX/

**Table 2**
*Chandra* Advanced CCD Imaging Spectrometer (ACIS) Observation Log

| Obs. ID | Aim Point $\alpha_{J2000}$ | Aim Point $\delta_{J2000}$ | Obs. Start (UT) | Exposure[a] (ks) | Flaring[b] Intervals | $\Delta\alpha$ (arcsec) | $\Delta\delta$ (arcsec) | Obs. Mode[c] |
|---|---|---|---|---|---|---|---|---|
| | | | NGC 0337 | | | | | |
| 12979[d] | 00 59 49.29 | −07 34 28.15 | 2011 Jul 19T23:07:02 | 10 | … | … | … | F |
| | | | NGC 0584 | | | | | |
| 12175[d] | 01 31 20.38 | −06 51 38.45 | 2010 Sep 7T01:40:53 | 10 | … | … | … | V |
| | | | NGC 0628 | | | | | |
| 14801 | 01 36 47.41 | +15 45 32.58 | 2013 Aug 21T15:40:51 | 10 | … | +0.05 | +0.01 | V |
| 16000 | 01 36 47.37 | +15 45 31.61 | 2013 Sep 21T06:40:27 | 40 | … | +0.56 | −0.24 | V |
| 16001 | 01 36 47.39 | +15 45 29.57 | 2013 Oct 7T23:56:17 | 15 | … | +0.24 | −0.07 | V |
| 16002 | 01 36 48.85 | +15 45 26.66 | 2013 Nov 14T20:10:48 | 38 | … | +0.08 | +0.16 | V |
| 16003 | 01 36 48.89 | +15 45 28.36 | 2013 Dec 15T15:55:42 | 40 | … | +0.04 | −0.11 | V |
| 16484 | 01 36 47.38 | +15 45 29.36 | 2013 Oct 10T14:31:23 | 15 | … | +0.45 | +0.14 | V |
| 16485 | 01 36 47.39 | +15 45 29.44 | 2013 Oct 11T11:13:35 | 9 | … | +0.32 | +0.06 | V |
| 2057 | 01 36 40.35 | +15 48 17.73 | 2001 Jun 19T19:03:09 | 46 | 1, 0.5 | −0.05 | −0.05 | F |
| 2058[d] | 01 36 36.11 | +15 46 51.99 | 2001 Oct 19T04:08:30 | 46 | … | … | … | F |
| 4753 | 01 36 51.21 | +15 45 12.44 | 2003 Nov 20T04:14:02 | 5 | … | −0.10 | −0.03 | F |
| 4754 | 01 36 51.51 | +15 45 12.89 | 2003 Dec 29T13:07:58 | 5 | … | +0.09 | +0.07 | F |
| Merged[e] | 01 36 44.82 | +15 46 11.67 | | 269 | 1, 0.5 | … | … | … |

**Notes.** The full version of this table contains entries for all 38 galaxies and 164 ObsIDs and is available in the electronic edition. An abbreviated version of the table is displayed here to illustrate its form and content.
[a] All observations were continuous. These times have been corrected for removed data that were affected by high background; see Section 3.2.
[b] Number of flaring intervals and their combined duration. These intervals were rejected from further analyses.
[c] The observing mode (F = Faint mode; V = Very Faint mode).
[d] Indicates Obs. ID by which all other observations are reprojected to for alignment purposes. This Obs. ID was chosen for reprojection as it had the longest initial exposure time, before flaring intervals were removed.
[e] Aim point represents exposure-time-weighted value.

(This table is available in its entirety in machine-readable form.)

using large simulations of fake sources (see Section 3.3 for details). Such completeness calculations are not feasible using the computationally intensive AE photometry procedure.

For sources with >20 net counts, we performed basic spectral modeling of the data within AE, using xspec v. 12.9.1 (Arnaud 1996). We adopted an absorbed power-law model with both a fixed component of Galactic absorption and a free variable intrinsic absorption component (TBABS × TBABS × POW in xspec). The free parameters include the intrinsic column density, $N_{\rm H,int}$, and photon index, $\Gamma$. The Galactic absorption column, $N_{\rm H,gal}$, for each source was fixed to the value appropriate for the location of each galaxy, as derived by Dickey & Lockman (1990).[14] All spectral fits were derived by minimizing the *C*-statistic within xspec (Cash 1979), with both the on-source events (i.e., those within the AE extraction regions discussed above) and background events supplied. AE simultaneously fits the background spectrum, using a piecewise linear model, and the on-source spectrum, including the background spectrum model plus the physical source model (i.e., the absorbed power law).

For the subsample of sources where spectral fitting was possible, we found median and interquartile ranges of $\log N_{\rm H,int} = 21.3^{+0.5}_{-0.7}$ and $\Gamma = 1.7^{+0.3}_{-0.5}$. Whenever possible, we computed 0.5–8 keV X-ray fluxes and corresponding luminosities using these best-fit models. For sources where spectral fitting was not possible, we converted the 0.5–7 keV count rates to 0.5–8 keV fluxes using the median model (i.e., $\log N_{\rm H,int} = 21.3$ and $\Gamma = 1.7$).

In the Appendix, we provide the properties of 4442 X-ray point sources in all 38 galaxies in our sample. Of these X-ray sources, 2478 had $L > 10^{35}$ erg s$^{-1}$ and were determined to lie within the galactic footprints of our sample. The galactic footprints were taken to be the ellipses that trace the $K_s \approx 20$ mag arcsec$^{-2}$ galactic surface brightness (see Jarrett et al. 2003), with some central regions excised owing to the presence of AGNs or substantial source crowding. These detailed regions, including exclusion region radii, $r_{\rm remove}$, are provided in Table 1. The remaining sources were located either outside the *K*-band-based regions or within the central regions removed from further analysis (i.e., AGNs and clearly crowded sources). We note that a substantial number of sources that we have excluded from our XLF analyses are outside the designated $K_s \approx 20$ mag arcsec$^{-2}$ region, yet within the larger "total" $K_s$-band ellipse, defined by Jarrett et al. (2003), or the generally larger RC3 regions, defined by de Vaucouleurs et al. (1991). Such sources still have some reasonable probability of being associated with the galaxy, so we report them in our X-ray point-source catalogs; however, their numbers are expected to be small compared with the number of CXB sources in those areas and are therefore not included in our XLF analyses. For convenience, we flag sources in our X-ray catalog that lie within the total $K_s$-band ellipse but outside the 20 mag arcsec$^{-2}$ ellipse (Flag = 3).

[14] Galactic column density values were extracted using the colden tool at http://cxc.harvard.edu/toolkit/colden.jsp.

### 3.3. Catalog Completeness Functions

Since our X-ray data sets span a broad range of *Chandra* depths, in terms of intrinsic X-ray point-source luminosity, it is essential to understand well the completeness of each of our data sets when fitting XLF models. To address this, we first derive radially dependent completeness functions for each galaxy using simulations, in which fake sources are added to the FB images and searched for using `wavdetect` following the prescription adopted in Section 3.2. For a given galaxy, we generated 700 simulated images in total. Each image consisted of our original 0.5–7 keV *Chandra* image plus 400 fake X-ray point sources, each of which contained a fixed number of source counts. Each fake X-ray source was placed randomly within the boundaries of a single box in a $20 \times 20$ grid of boxes that spanned the image in equal intervals of R.A. and decl. A given simulated image would thus contain 400 fake X-ray sources with one source per box and an equal number of X-ray counts per source. Fifty simulated images were created for each of 14 different choices of simulated source counts with nearly logarithmic spacing (spanning 3–500 source counts). Source counts were probabilistically placed onto the base image using the nearest `MARX`-based, exposure-weighted PSF that was generated in the `AE` runs (see Section 3.2) for the original source catalog. This method was adopted as a practical compromise between running very accurate time-consuming PSF models for a small number of simulated sources and having a robust characterization of the completeness functions based on many sources with slightly inaccurate local PSFs.

To construct the completeness functions themselves, we (1) repeated the source detection procedure described in Section 3.2 for all 700 mock images and (2) compared the mock catalogs with the input catalogs to determine whether a given source was recovered. In a general sense, the completeness functions, for a given galaxy, vary with off-axis angle with respect to the mean aim point and local background and point-source density. In Section 4 below, we describe how we use our completeness functions when measuring XRB XLFs.

## 4. X-Ray Luminosity Function Measurements

### 4.1. Galaxy-wide X-Ray Luminosity Function Properties

We began our XLF analyses by fitting the galaxy-wide 0.5–8 keV XLFs for each of the galaxies. As discussed above, we utilized only X-ray point sources and galaxy properties that are appropriate for the regions defined in Table 1, which in some cases means excluding central regions (due to source crowding and AGNs). In Figure 3, we display the galaxy-wide *observed* cumulative XLFs (gray filled circles with $1\sigma$ Poisson error bars) for the galaxies in our sample. The data used here are simply raw counts and not corrected for incompleteness. Furthermore, the X-ray point sources will contain contributions from not only objects that are intrinsic to the galaxies but also background X-ray point sources from the cosmic X-ray background (CXB; e.g., Kim et al. 2007; Georgakakis et al. 2008) and occasionally foreground stars that are X-ray detected.

We fit the observed galaxy-wide XLFs following a forward-fitting approach, in which we include contributions from the intrinsic X-ray sources (the vast majority of which we expect to be XRBs) and CXB sources, with incompleteness folded into our models. For the *intrinsic* point-source XLF, we began by fitting the data to single and broken power-law models of the respective forms:

$$\frac{dN}{dL} = K_{\rm PL}\begin{cases} L^{-\alpha}, & (L < L_c) \\ 0, & (L \geqslant L_c) \end{cases}, \tag{4}$$

$$\frac{dN}{dL} = K_{\rm BKNPL}\begin{cases} L^{-\alpha_1} & (L < L_b) \\ L_b^{\alpha_2-\alpha_1}L^{-\alpha_2}, & (L_b \leqslant L < L_c), \\ 0, & (L \geqslant L_c) \end{cases} \tag{5}$$

where $K_{\rm PL}$ and $\alpha$ are the single power-law normalization and slope, respectively, and $K_{\rm BKNPL}$, $\alpha_1$, $L_b$, and $\alpha_2$ are the broken power-law normalization, low-luminosity slope, break luminosity, and high-luminosity slope, respectively; both XLF models are truncated above $L_c$, the cutoff luminosity. To make the numbers more intuitive, we take $L$, $L_b$, and $L_c$ to be in units of $10^{38}$ erg s$^{-1}$, when quoting and describing normalization values. For a given galaxy, we fit the data to determine all constants, except for the break and cutoff luminosities, which we fix at $L_b = 10^{38}$ erg s$^{-1}$ and $L_c = 2 \times 10^{40}$ erg s$^{-1}$. Also, when the luminosity of the 50% completeness limit (see below for completeness description), $L_{50}$, was larger than $0.5 \times L_b$, the fit to $\alpha_1$ was unreliable. For these cases, $\alpha_1$ was fixed to either 1.2 or 1.6 for galaxies that are respectively below or above sSFR $= 10^{-10}$ yr$^{-1}$. Similarly, in some cases, $L_{50}$ was above the $L_b$ and $\alpha_2$ was unreliable. For these cases, $\alpha_2$ was fixed to either 2.2 or 1.6 for galaxies that are below or above sSFR $= 10^{-10}$ yr$^{-1}$, respectively.

In principle, we can fit for these values for each galaxy, and we have made attempts to free these parameters; however, in most cases, $L_b$ is not well constrained, and the best-fit value of $L_c$ often ends up being a lower limit constraint at the highest-luminosity point source for each galaxy. We therefore chose to fix these parameters near sample-averaged values, which we determine in Section 4.2 below. There are thus three free parameters, namely, $K_{\rm BKNPL}$, $\alpha_1$, and $\alpha_2$.

For the CXB contribution, we implemented a fixed form for the number counts, provided by Kim et al. (2007). The Kim et al. (2007) extragalactic number counts provide estimates of the number of sources per unit area versus 0.5–8 keV flux. The best-fit function follows a broken power-law distribution with parameters derived from the combined *Chandra* Multiwavelength Project (ChaMP) and *Chandra* Deep Field-South (CDF-S) extragalactic survey data sets (see Table 4 of Kim et al. 2007). For each galaxy, the number counts were converted to an observed 0.5–8 keV XLF contribution by multiplying the number counts by the areal extent of the galaxy, as defined in Table 1, and converting CXB model fluxes to X-ray luminosities, given the distance to the galaxy.

A complete model of the observed XLF, $dN/dL$(obs), consists of the intrinsic XLF component, $dN/dL$(int), e.g., from Equation (4), plus the fixed CXB curve, $dN/dL$(CXB), convolved with a galaxy-wide weighted completeness function, $\xi(L)$, which was constructed using the radial-dependent completeness functions calculated in Section 4. Specifically, $\xi(L)$ was calculated by statistically weighting the contributions from the model XLF at each annulus according to the observed distributions of X-ray point sources. Formally, we computed $\xi(L)$ using the following relation:

$$\xi(L) = \sum_i \xi_i(L) \times w_i, \tag{6}$$

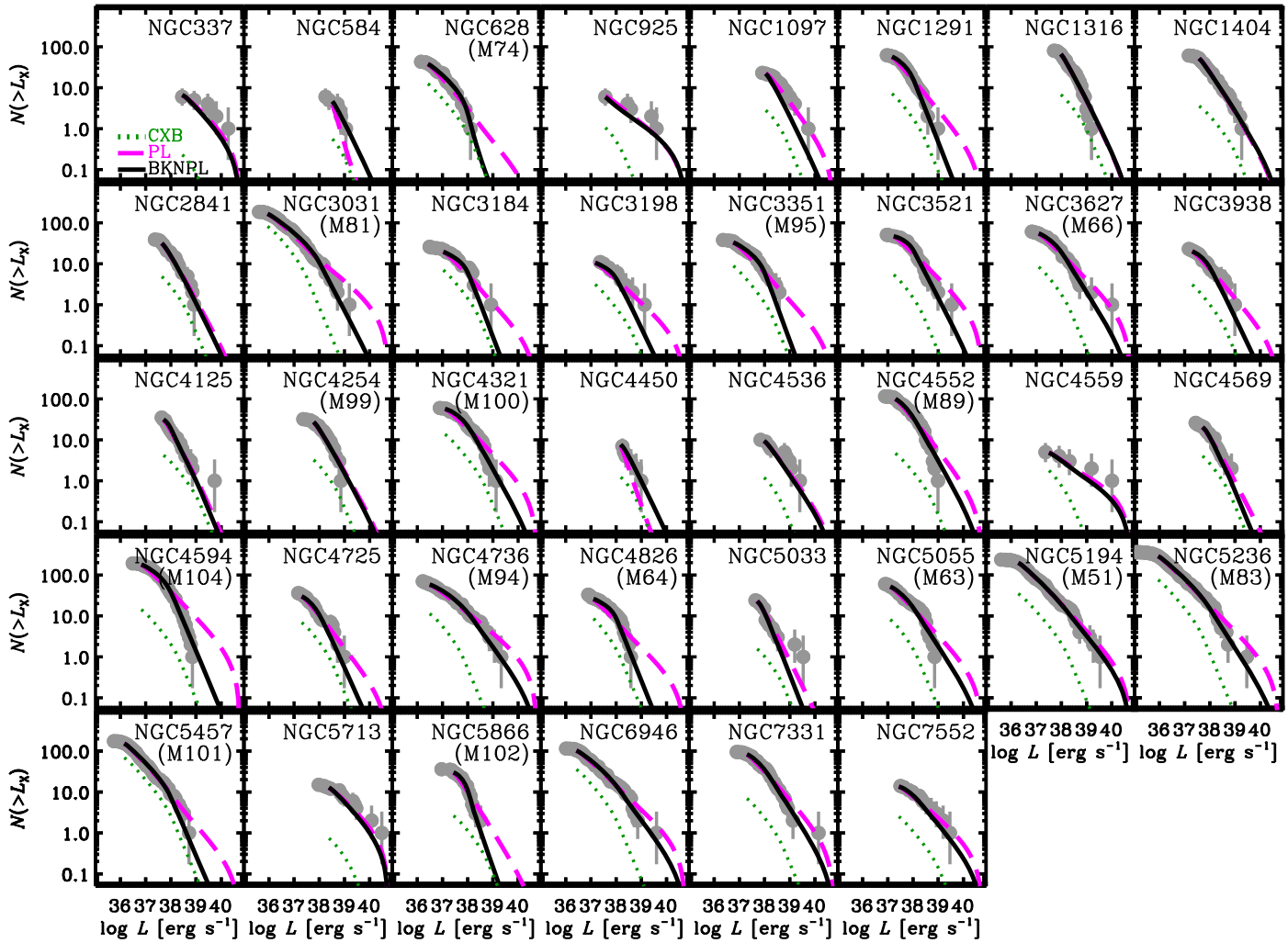


**Figure 3.** Observed cumulative XLFs for all galaxies in our sample (gray circles with $1\sigma$ error bars). These XLFs are not corrected for incompleteness, explaining the perceptible turnovers at the lowest luminosity values. Model fits, which include contributions from the CXB (green dotted curves) and intrinsic point sources, are shown for single (dashed magenta curves) and broken (black solid curves) power-law models. Displayed models (and CXB contributions) include the effects of incompleteness for the purposes of fitting the observed data (see Section 4.1 for details). All data above the 50% completeness limits, $L_{50}$, were used in our fits, and the plotted model curves are displayed going down to these limits.

where $\xi_i(L)$ is the completeness function for the $i$th annular bin and $w_i$ is the fraction of total number of galaxy-wide sources within the $i$th annular bin based on the observed point-source distributions. For all galaxies, $\xi(L)$ is very close to a monotonically increasing function, although some low-level fluctuations exist owing to the nature of our simulations. For points of reference, we quote and utilize two luminosity limits, $L_{50}$ and $L_{90}$, which correspond to the point-source luminosity at 50% and 90% completeness (i.e., $\xi(L_{50}) = 0.5$ and $\xi(L_{90}) = 0.9$). These values are tabulated in Table 3.

We thus modeled the observed XLF using a multiplicative model

$$dN/dL(\mathrm{obs}) = \xi(L)[dN/dL(\mathrm{int}) + dN/dL(\mathrm{CXB})]. \quad (7)$$

Procedurally, for each galaxy, we constructed the observed $dN/dL$(obs) using luminosity bins of constant $\delta \log L = 0.057$ dex that spanned the range of $L_{\mathrm{min}} = L_{50}$ to $L_{\mathrm{max}} = 5 \times 10^{41}$ erg s$^{-1}$. For most galaxies, the majority of the bins contained zero sources, with other bins containing small numbers of sources. As such, we evaluated the goodness of fit using a modified version of the $C$-statistic (`cstat`; Cash 1979; Kaastra 2017):

$$C = 2\sum_{i=1}^{n} M_i - N_i + N_i \ln(N_i/M_i), \quad (8)$$

where the summation takes place over the $n = 100$ bins of X-ray luminosity, and $N_i$ and $M_i$ are the observed and model counts. We note that when $N_i = 0$, $N_i \ln(N_i/M_i) = 0$, and when $M_i = 0$ (e.g., beyond the cutoff luminosity), the entire $i$th term in the summation is zero.

When fitting our data and measuring uncertainties on parameters, we made use of a Markov Chain Monte Carlo (MCMC) procedure that implemented the Metropolis–Hastings sampling algorithm (Hastings 1970). In this procedure, the fitting parameters were first given initial guesses, which we took to be the same set of values for every galaxy. The value of `cstat`, $C_{\mathrm{init}}$, was computed for this initial guess and stored. Next, the guesses were perturbed randomly in accordance with a Gaussian distribution with a user-supplied set of standard deviations for each parameter. To begin, we chose the widths of the Gaussians to be large (relative to their likely final

**Table 3**
X-Ray Luminosity Function Fits by Galaxy

| Galaxy Name (NGC) (1) | Alt Name (2) | $N_{src}$ (3) | log $L_{50}$ (erg s$^{-1}$) (4) | log $L_{90}$ (erg s$^{-1}$) (5) | Single Power Law[a] $K_{PL}$ (6) | $\alpha$ (7) | $C$ (8) | $P_{Null}$ (9) | Broken Power Law[b] $K_{BKNPL}$ (10) | $\alpha_1$ (11) | $\alpha_2$ (12) | $C$ (13) | $P_{Null}$ (14) | Model (S B) (15) | log $L_X$ (ergs s$^{-1}$) (16) |
|---|---|---|---|---|---|---|---|---|---|---|---|---|---|---|---|
| 337 | ⋯ | 6 | 38.5 | 38.7 | $6.0^{+12.6}_{-4.6}$ | $1.49^{+0.42}_{-0.31}$ | 22 | 0.944 | $8.08^{+3.74}_{-3.00}$ | 1.60[c] | 1.60[c] | 23 | 0.889 | B | 40.4 ± 0.2 |
| 584 | ⋯ | 7 | 38.5 | 38.7 | $193^{+504}_{-151}$ | $3.60^{+0.88}_{-0.99}$ | 11 | 0.686 | $21.0^{+12.4}_{-9.2}$ | 1.20[c] | 2.20[c] | 9 | 0.169 | B | 40.0 ± 0.2 |
| 628 | M74 | 43 | 36.4 | 36.6 | $1.51^{+0.67}_{-0.55}$ | $1.68^{+0.16}_{-0.14}$ | 31 | 0.106 | $4.16^{+2.16}_{-1.58}$ | 1.25 ± 0.21 | $4.05^{+0.66}_{-0.95}$ | 26 | 0.109 | B | 38.9 ± 0.2 |
| 925 | ⋯ | 7 | 37.5 | 37.7 | $1.47^{+1.02}_{-0.72}$ | $1.37^{+0.26}_{-0.24}$ | 26 | 0.785 | $1.03^{+0.82}_{-0.52}$ | $2.28^{+1.17}_{-1.30}$ | $1.30^{+0.27}_{-0.24}$ | 25 | 0.849 | S | 40.1 ± 0.4 |
| 1097 | ⋯ | 23 | 38.0 | 38.2 | $17.4^{+7.4}_{-5.6}$ | $1.75^{+0.20}_{-0.18}$ | 25 | 0.261 | $28.9^{+7.2}_{-6.3}$ | 1.20[c] | 2.20[c] | 33 | 0.387 | B | 40.1 ± 0.1 |
| 1291 | ⋯ | 62 | 37.1 | 37.3 | $9.26^{+1.77}_{-1.58}$ | $1.69^{+0.11}_{-0.09}$ | 36 | 0.162 | $21.5^{+4.7}_{-4.1}$ | $0.90^{+0.19}_{-0.20}$ | $2.60^{+0.40}_{-0.31}$ | 25 | 0.173 | B | $39.7^{+0.2}_{-0.1}$ |
| 1316 | ⋯ | 81 | 37.9 | 38.1 | $70.6^{+14.6}_{-12.3}$ | $2.21^{+0.19}_{-0.16}$ | 28 | 0.383 | $70.4^{+15.8}_{-13.1}$ | 1.20[c] | $2.20^{+0.19}_{-0.17}$ | 28 | 0.383 | S | $40.9^{+0.2}_{-0.1}$ |
| 1404 | ⋯ | 61 | 37.6 | 37.9 | $20.7^{+3.3}_{-3.1}$ | $1.99^{+0.14}_{-0.12}$ | 27 | 0.061 | $19.6^{+4.3}_{-3.8}$ | $2.09^{+0.35}_{-0.34}$ | $1.95^{+0.20}_{-0.17}$ | 27 | 0.047 | S | 40.4 ± 0.1 |
| 2841 | ⋯ | 40 | 37.6 | 37.8 | $12.2^{+2.9}_{-2.6}$ | $2.05^{+0.23}_{-0.19}$ | 24 | 0.218 | $13.9^{+4.2}_{-3.6}$ | $1.70^{+0.58}_{-0.59}$ | $2.17^{+0.34}_{-0.26}$ | 24 | 0.283 | S | 40.2 ± 0.1 |
| 3031 | M81 | 185 | 35.9 | 36.3 | $5.15^{+1.07}_{-0.93}$ | 1.43 ± 0.06 | 50 | 0.034 | $10.6^{+2.7}_{-2.4}$ | 1.18 ± 0.09 | $2.16^{+0.31}_{-0.25}$ | 43 | 0.092 | B | $39.7^{+0.3}_{-0.2}$ |
| 3184 | ⋯ | 26 | 37.0 | 37.2 | $2.17^{+0.87}_{-0.74}$ | $1.56^{+0.19}_{-0.17}$ | 37 | 0.782 | $7.25^{+3.29}_{-2.66}$ | $0.35^{+0.35}_{-0.24}$ | $2.73^{+0.87}_{-0.58}$ | 34 | 0.773 | B | 39.2 ± 0.3 |
| 3198 | ⋯ | 11 | 37.1 | 37.3 | $1.51^{+0.74}_{-0.61}$ | $1.45^{+0.22}_{-0.19}$ | 30 | 0.748 | $4.01^{+2.37}_{-1.73}$ | $0.28^{+0.37}_{-0.20}$ | $2.23^{+0.92}_{-0.48}$ | 28 | 0.851 | B | $39.2^{+0.5}_{-0.4}$ |
| 3351 | M95 | 38 | 36.7 | 36.9 | $2.88^{+0.89}_{-0.76}$ | $1.59^{+0.14}_{-0.12}$ | 23 | 0.008 | $7.92^{+3.24}_{-2.53}$ | $0.93^{+0.25}_{-0.27}$ | $2.78^{+0.87}_{-0.55}$ | 21 | 0.032 | B | $39.3^{+0.3}_{-0.2}$ |
| 3521 | ⋯ | 51 | 37.2 | 37.4 | $9.05^{+1.79}_{-1.60}$ | 1.55 ± 0.09 | 45 | 0.545 | $22.1^{+4.7}_{-4.3}$ | $0.36^{+0.27}_{-0.22}$ | $2.17^{+0.23}_{-0.21}$ | 30 | 0.267 | B | 40.0 ± 0.2 |
| 3627 | M66 | 61 | 37.1 | 37.3 | $8.43^{+1.60}_{-1.46}$ | 1.55 ± 0.09 | 45 | 0.554 | $15.5^{+3.7}_{-3.2}$ | $0.98^{+0.21}_{-0.22}$ | $1.95^{+0.20}_{-0.18}$ | 41 | 0.738 | B | 40.1 ± 0.2 |
| 3938 | ⋯ | 23 | 37.2 | 37.4 | $4.03^{+1.24}_{-1.05}$ | $1.65^{+0.17}_{-0.16}$ | 23 | 0.056 | $8.06^{+3.24}_{-2.55}$ | 0.76 ± 0.42 | $2.23^{+0.54}_{-0.35}$ | 23 | 0.219 | B | 39.5 ± 0.3 |
| 4125 | ⋯ | 35 | 37.7 | 37.9 | $15.8^{+3.6}_{-3.3}$ | $2.26^{+0.29}_{-0.23}$ | 26 | 0.458 | $20.9^{+5.6}_{-4.9}$ | 1.20[c] | $2.44^{+0.53}_{-0.35}$ | 28 | 0.796 | S | $40.3^{+0.3}_{-0.1}$ |
| 4254 | M99 | 32 | 37.7 | 37.9 | $14.9^{+3.8}_{-3.4}$ | $2.02^{+0.22}_{-0.19}$ | 16 | 0.017 | $16.4^{+4.7}_{-4.1}$ | 1.60[c] | $2.08^{+0.29}_{-0.24}$ | 15 | 0.019 | S | 40.3 ± 0.1 |
| 4321 | M100 | 60 | 37.1 | 37.3 | $8.18^{+1.70}_{-1.51}$ | $1.53^{+0.10}_{-0.09}$ | 44 | 0.363 | $17.8^{+4.3}_{-3.7}$ | $0.71^{+0.25}_{-0.26}$ | $2.04^{+0.24}_{-0.19}$ | 36 | 0.399 | B | 40.1 ± 0.2 |
| 4450 | ⋯ | 7 | 38.2 | 38.4 | $45.6^{+63.0}_{-27.2}$ | $3.47^{+1.08}_{-0.89}$ | 13 | 0.464 | $14.0^{+6.5}_{-5.3}$ | 1.20[c] | 2.20[c] | 12 | 0.148 | B | 39.8 ± 0.2 |
| 4536 | ⋯ | 10 | 38.0 | 38.1 | $6.20^{+4.41}_{-2.84}$ | $1.76^{+0.36}_{-0.28}$ | 22 | 0.604 | $6.85^{+4.94}_{-3.17}$ | 1.60[c] | $1.83^{+0.41}_{-0.30}$ | 22 | 0.693 | S | $40.1^{+0.3}_{-0.2}$ |
| 4552 | M89 | 115 | 37.2 | 37.6 | $23.3^{+2.7}_{-2.6}$ | $1.76^{+0.08}_{-0.07}$ | 40 | 0.002 | $34.9^{+5.1}_{-4.7}$ | 1.28 ± 0.16 | $2.07^{+0.15}_{-0.14}$ | 35 | 0.068 | B | 40.3 ± 0.1 |
| 4559 | ⋯ | 5 | 37.5 | 37.6 | $0.62^{+0.66}_{-0.39}$ | $1.17^{+0.28}_{-0.27}$ | 20 | 0.668 | $0.74^{+0.80}_{-0.46}$ | $0.90^{+0.90}_{-0.61}$ | $1.25^{+0.32}_{-0.29}$ | 20 | 0.768 | S | $40.1^{+0.4}_{-0.5}$ |
| 4569 | | 26 | 37.7 | 37.8 | $8.85^{+2.90}_{-2.50}$ | $2.09^{+0.29}_{-0.26}$ | 20 | 0.132 | $12.1^{+4.4}_{-3.7}$ | $1.13^{+0.78}_{-0.69}$ | $2.46^{+0.60}_{-0.39}$ | 19 | 0.255 | B | $39.7^{+0.3}_{-0.2}$ |
| 4594 | M104 | 192 | 36.8 | 37.1 | $21.3^{+2.2}_{-2.1}$ | 1.59 ± 0.05 | 59 | 0.707 | $48.0^{+5.5}_{-5.2}$ | $1.06^{+0.07}_{-0.08}$ | $2.45^{+0.20}_{-0.17}$ | 22 | 0.010 | B | 40.2 ± 0.1 |
| 4725 | ⋯ | 36 | 37.3 | 37.5 | $5.57^{+1.60}_{-1.38}$ | $1.72^{+0.17}_{-0.15}$ | 31 | 0.274 | $10.1^{+3.8}_{-3.1}$ | 1.01 ± 0.38 | $2.32^{+0.59}_{-0.36}$ | 30 | 0.694 | B | $39.6^{+0.3}_{-0.2}$ |
| 4736 | M94 | 71 | 36.5 | 36.8 | $4.97^{+1.02}_{-0.88}$ | $1.42^{+0.08}_{-0.07}$ | 55 | 0.554 | $8.82^{+2.54}_{-2.09}$ | $1.13^{+0.13}_{-0.14}$ | $1.81^{+0.21}_{-0.18}$ | 52 | 0.842 | B | 40.1 ± 0.3 |
| 4826 | M64 | 33 | 37.0 | 37.2 | $2.96^{+1.05}_{-0.89}$ | $1.51^{+0.17}_{-0.14}$ | 25 | 0.044 | $10.2^{+3.6}_{-3.1}$ | $0.29^{+0.27}_{-0.20}$ | $2.55^{+0.60}_{-0.43}$ | 17 | 0.023 | B | $39.4^{+0.3}_{-0.2}$ |
| 5033 | ⋯ | 24 | 37.7 | 37.9 | $12.5^{+3.1}_{-2.8}$ | $2.19^{+0.27}_{-0.24}$ | 30 | 0.884 | $16.3^{+5.4}_{-4.5}$ | 1.49 ± 0.74 | $2.60^{+0.91}_{-0.45}$ | 31 | 0.424 | B | $39.8^{+0.4}_{-0.2}$ |
| 5055 | M63 | 61 | 37.1 | 37.3 | $7.88^{+1.60}_{-1.40}$ | 1.59 ± 0.10 | 34 | 0.101 | $12.6^{+3.3}_{-2.8}$ | $1.17^{+0.21}_{-0.22}$ | $1.91^{+0.21}_{-0.18}$ | 33 | 0.215 | B | 40.1 ± 0.2 |
| 5194 | M51 | 237 | 36.3 | 36.6 | $10.1^{+1.5}_{-1.4}$ | 1.59 ± 0.05 | 49 | 0.034 | $11.4^{+2.4}_{-2.1}$ | 1.55 ± 0.07 | $1.71^{+0.15}_{-0.13}$ | 48 | 0.062 | B | 40.4 ± 0.2 |
| 5236 | M83 | 363 | 35.9 | 36.2 | $8.94^{+1.42}_{-1.31}$ | $1.56^{+0.05}_{-0.04}$ | 57 | 0.073 | $12.0^{+2.3}_{-2.1}$ | $1.47^{+0.06}_{-0.05}$ | $1.93^{+0.22}_{-0.18}$ | 54 | 0.182 | B | 40.1 ± 0.2 |
| 5457 | M101 | 174 | 36.1 | 36.3 | $3.90^{+1.07}_{-0.93}$ | 1.62 ± 0.08 | 38 | 0.019 | $6.14^{+2.45}_{-1.86}$ | $1.47^{+0.12}_{-0.13}$ | $2.41^{+0.78}_{-0.45}$ | 37 | 0.088 | B | $39.4^{+0.3}_{-0.2}$ |
| 5713 | ⋯ | 15 | 38.3 | 38.7 | $10.2^{+10.0}_{-5.7}$ | 1.49 ± 0.24 | 29 | 0.456 | $13.9^{+4.4}_{-3.8}$ | 1.60[c] | 1.60[c] | 30 | 0.638 | S | 40.7 ± 0.2 |
| 5866 | M102 | 36 | 37.4 | 37.6 | $8.08^{+1.95}_{-1.72}$ | $1.95^{+0.18}_{-0.17}$ | 26 | 0.214 | $19.6^{+5.1}_{-4.4}$ | $0.64^{+0.37}_{-0.34}$ | $3.30^{+0.69}_{-0.53}$ | 17 | 0.188 | B | 39.5 ± 0.1 |

**Table 3**
(Continued)

| Galaxy Name (NGC) (1) | Alt Name (2) | $N_{src}$ (3) | log $L_{50}$ (erg s$^{-1}$) (4) | log $L_{90}$ (erg s$^{-1}$) (5) | Single Power Law[a] $K_{PL}$ (6) | $\alpha$ (7) | $C$ (8) | $P_{Null}$ (9) | Broken Power Law[b] $K_{BKNPL}$ (10) | $\alpha_1$ (11) | $\alpha_2$ (12) | $C$ (13) | $P_{Null}$ (14) | Model (S B) (15) | log $L_X$ (ergs s$^{-1}$) (16) |
|---|---|---|---|---|---|---|---|---|---|---|---|---|---|---|---|
| 6946 | ⋯ | 115 | 36.4 | 36.7 | $6.01^{+1.23}_{-1.07}$ | $1.49 \pm 0.07$ | 53 | 0.289 | $8.99^{+2.49}_{-2.08}$ | $1.30^{+0.12}_{-0.11}$ | $1.78^{+0.20}_{-0.18}$ | 52 | 0.552 | B | $40.1 \pm 0.3$ |
| 7331 | ⋯ | 95 | 37.2 | 37.5 | $18.3^{+2.4}_{-2.3}$ | $1.65^{+0.08}_{-0.07}$ | 56 | 0.710 | $28.7^{+4.7}_{-4.3}$ | $1.06^{+0.19}_{-0.20}$ | $1.92^{+0.14}_{-0.13}$ | 50 | 0.703 | B | $40.4 \pm 0.2$ |
| 7552 | ⋯ | 14 | 37.4 | 37.6 | $2.95^{+1.25}_{-0.98}$ | $1.43^{+0.19}_{-0.16}$ | 28 | 0.190 | $4.72^{+2.32}_{-1.70}$ | $0.43^{+0.50}_{-0.31}$ | $1.67^{+0.28}_{-0.23}$ | 27 | 0.351 | B | $40.0^{+0.3}_{-0.4}$ |

**Notes.** All fits include the effects of incompleteness and model contributions from the CXB, following Equation (7). A full description of our model fitting procedure is outlined in Section 4.1. Cols. (1) and (2): galaxy NGC and Messier name, as reported in Table 1. Col. (3): total number of X-ray sources detected within the galactic boundaries defined in Table 1. Cols. (4) and (5): logarithm of the luminosities corresponding to the respective 50% and 90% completeness limits. Cols. (6) and (7): median and $1\sigma$ uncertainty values of the single power-law normalization and slope, respectively (see Equation (4))—our adopted "best model" consists of the median values. Col. (8): *C*-statistic, *C*, associated with the best model. Col. (9): null-hypothesis probability of the best model describing the data. The null-hypothesis probability is calculated following the prescription in Kaastra (2017) and is appropriate for the use of the *C*-statistic. Cols. (10)–(12): median and $1\sigma$ uncertainty values of the single power-law normalization and slope, respectively (see Equation (5)). Cols. (13) and (14): *C*-statistic and null-hypothesis probability, respectively, for the best broken power-law model. Col. (15): adopted model, used to calculate integrated X-ray luminosity. Here "S" and "B" are the single and broken power-law models, respectively. Col. (16): integrated X-ray luminosity, $L_X$, from Equation (9) for the adopted model.

[a] Single power-law models are derived following Equation (4) with a fixed cutoff luminosity of $L_c = 5 \times 10^{40}$ erg s$^{-1}$.

[b] Broken power-law models are derived following Equation (5) with a fixed break luminosity of $L_b = 10^{38}$ erg s$^{-1}$ and cutoff luminosity of $L_c = 5 \times 10^{40}$ erg s$^{-1}$.

[c] Parameter was fixed due to shallow *Chandra* depth.

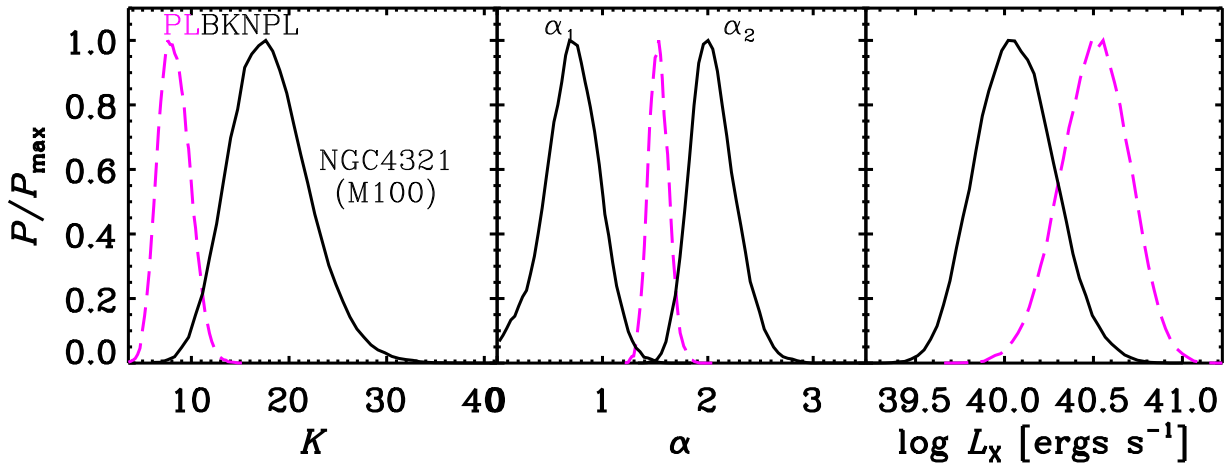


**Figure 4.** Example PDFs for single (magenta dashed curves) and broken (black solid curves) power-law parameters, based on fits to the XLF of NGC 4321 (M100). The normalization ($K$), XLF slopes, and integrated point-source luminosity, $L_X$, are displayed here. The data and best-fit models are shown in Figure 3.

distributions) so as to sample parameter space well. The `cstat` value of the model with perturbed parameters was then computed, $C_{pert}$, and compared with the value obtained from the previous run, and the likelihood ratio, $\mathcal{L}_{rat} = \exp\{-(C_{pert} - C_{init})/2\}$, was evaluated. Next, a random number, $A_{random}$, between 0 and 1, was drawn and compared with $\mathcal{L}_{rat}$. If $\mathcal{L}_{rat} > A_{random}$, then the new set of parameters was stored, and if $\mathcal{L}_{rat} \leqslant A_{random}$, then the old set of parameters was preserved for subsequent perturbations. Using the current set of stored parameters, the above procedure (i.e., perturbation of parameters, evaluation of $\mathcal{L}_{rat}$, and comparison with $A_{random}$) was then repeated 100,000 times, with each iteration using only accepted parameters, to form an initial MCMC chain.

After the 100,000 iterations, we used the initial MCMC chain to compute updated standard deviations of the accepted values and subsequently ran an additional 900,000 final MCMC iterations, using these standard deviations and the final set of parameters in the initial MCMC chain as a starting point. The distributions of parameter values from the final MCMC chain formed our probability distribution functions (PDFs). Furthermore, additional model-dependent calculated parameter PDFs can be computed by storing their values in MCMC chains. For example, for each model in the MCMC chain we compute the integrated 0.5–8 keV luminosity, $L_X$:

$$L_X \equiv \int_{L_{lo}}^{L_c} \frac{dN}{dL} L dL, \tag{9}$$

where we adopt a lower integration limit of $L_{lo} = 10^{36}$ erg $s^{-1}$.

We note that for a single power-law model PDFs can be computed with ease using grid-based sampling of the 2D parameter space (i.e., normalization and slope of the power law). We compared PDFs that were computed from such grid-based sampling with those obtained from our MCMC procedure and found essentially identical PDFs. Since we later incorporate more complex models, with up to seven free parameters (Section 4.2 below), where the computation time is too large to use a grid-based approach, we chose to use the MCMC procedure consistently throughout this paper.

Hereafter, when quoting best-fit parameter values and uncertainties, we adopt median values from each PDF with 16% and 84% confidence lower and upper limits. In Table 3, we tabulate the best-fit parameter values for the single and broken power-law fits for each each galaxy. In Figure 3, we show the best-fit single (magenta dashed curves) and broken (black solid curves) power-law model cumulative XLFs, which include contributions from the CXB (green dotted curves) and have incompleteness folded in. Goodness of fit was evaluated following the methods outlined in Kaastra (2017), which provides parameterizations of the expected $C$-statistic and its variance for a given model and data binning scheme, so that goodness of fit can be evaluated in an identical way to classical $\chi^2$ fitting. For each of our fits, the null-hypothesis probability, $P_{null}$, was calculated as the one minus the probability that the model can be rejected. The values of $P_{null}$ are listed in Table 3 for both models.

For many galaxies, a single power law provides a statistically acceptable fit to the data (e.g., $P_{null} > 0.01$), with only one of the fits being rejected at the >99.9% confidence level ($P_{null} < 0.001$). The majority of the poorest fit cases (e.g., $P_{null} < 0.05$) have a large number of sources detected, due to deep observational data sets. Visual inspection of the fits suggests that some complex structures within the XLFs themselves are not described well with power laws. Not surprisingly, the broken power-law model provides improvements to the `cstat` values of the XLFs for many cases; however, in very few cases are the fit improvements statistically significant.

Despite the lack of statistical improvement, we expect that in most cases the broken power-law fits provide more realistic estimates of the integrated total luminosity, $L_X$, than the single power-law fits. One clear example where the solutions are notably different is illustrated in Figure 4 for NGC 4321 (M100). While statistically the single and broken power-law fits have very close $P_{null}$ values to each other, the overall $C$ is notably improved by the broken power-law fit and the calculated $L_X$ values are substantially different between models. We note that this is an extreme case and that most galaxies have better agreement between $L_X$ values when both models are statistically acceptable. We therefore chose to adopt parameters derived using the broken power-law model, unless either (1) the $C$ value for the broken power law provided no improvement over the single power-law value or (2) the two slopes implied by the broken power law (i.e., $\alpha_1$ and $\alpha_2$) were within $1\sigma$ of each other. In Table 3, we indicate our adopted model and list $L_X$ based on that model.

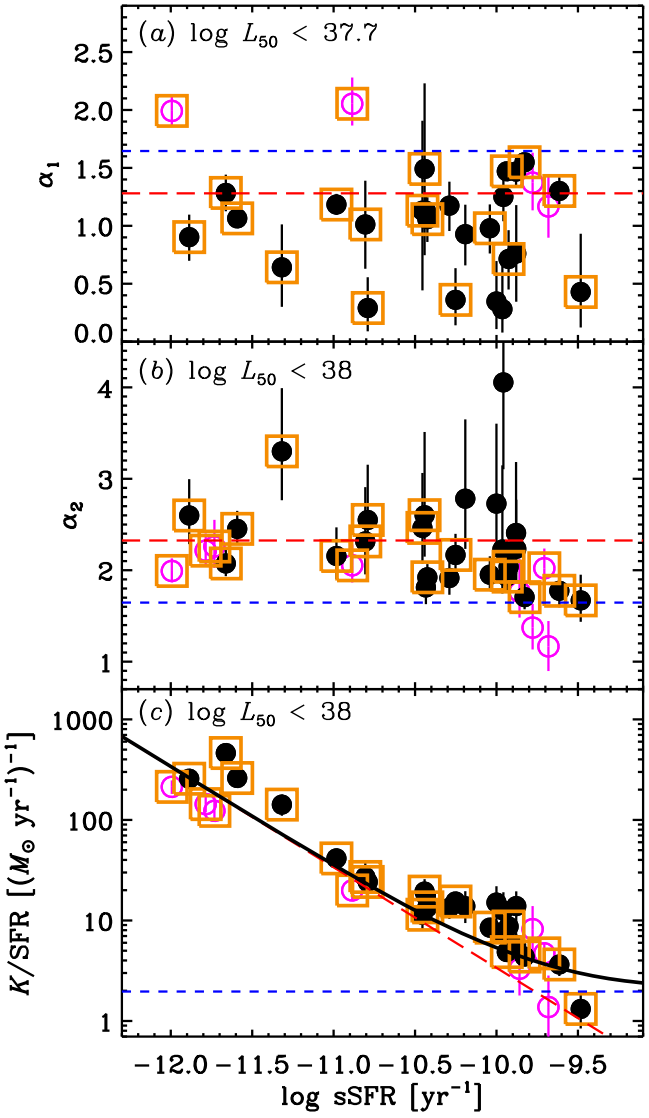


**Figure 5.** Best-fit XLF parameter values vs. sSFR for the galaxy-wide XLF fits. Solid and open magenta symbols indicate that parameter values are determined from fits to broken and single power-law models, respectively. Orange squares highlight galaxies with $M_\star > 2 \times 10^{10}\ M_\odot$ or SFR $> 2\ M_\odot$ yr$^{-1}$ to indicate sources that are least likely to suffer from variance due to poor sampling of the XLF. For $\alpha_1$, we plot only objects with faintest sources $L_{50} < 5 \times 10^{37}$ erg s$^{-1}$, where this parameter can be constrained. Similarly, we only display $\alpha_2$ and $K$ constraints for galaxies with $L_{50} < 10^{38}$ erg s$^{-1}$. For cases where the single power-law fit was used, values of $\alpha_1$ and $\alpha_2$ are set to $\alpha$. In each panel, the trends for HMXBs (blue short-dashed) and LMXBs (red long-dashed) are displayed, based on the global model fit presented in Section 4.2, and their combined trends are shown with black solid curves.

In Figure 5, we show the best-fit XLF parameter values versus sSFR for all galaxies in our sample. In terms of trends, $\alpha_1$ is consistent with being constant across all sSFR values, suggesting little variation in the low-luminosity slope of the XLF for young versus old populations. $\alpha_2$, on the other hand, exhibits an average decline with increasing sSFR (Spearman's $\rho$ correlation significance >99.95% confidence level), presumably indicating that the XRB population transitions from LMXBs to HMXBs. If we restrict the sample to massive galaxies ($\gtrsim 2 \times 10^{10}\ M_\odot$) or galaxies with substantial SFRs ($\gtrsim 2\ M_\odot$ yr$^{-1}$), so that the respective LMXB and HMXB population statistics allow for less galaxy-to-galaxy sampling stochasticity (e.g., Gilfanov 2004; Justham & Schawinski 2012; see Section 5.3 below), we get a clearer sense of this trend (see orange boxes in Figure 5). Finally, we find that the normalization per unit SFR declines with increasing sSFR, as would be expected as the population shifts from being LMXB dominated at low sSFR to more HMXB dominated at high sSFR.

In Figure 6, we show $L_X$/SFR versus sSFR for the sample. As reported by previous authors, this curve shows a clear decline of $L_X$/SFR with increasing sSFR, due to the transition from LMXBs to HMXBs (e.g., Colbert et al. 2004; Lehmer et al. 2010). From Figure 5, it can be inferred that this trend is largely driven by the decline in normalization per unit SFR of the XLF. However, for galaxies where the XLFs are expected to be well sampled (i.e., the orange squares in Figures 5 and 6), we find a larger range in $K$/SFR than $L_X$/SFR, due to the fact that the high-luminosity end XLF slope ($\alpha_2$) becomes shallower for galaxies with high sSFR (Figure 5(b)), due to the relatively shallow-sloped HMXB XLF becoming more dominant (e.g., Grimm et al. 2003; M12).

### 4.2. Global Fit to sSFR-binned Regions

As discussed above, it is expected that the decline in $L_X$/SFR with sSFR is driven by a transition from LMXB to HMXB dominance, and the rate of decline is affected by changes in *both* XLF normalizations and slopes. Here we examine XLFs in subgalactic regions, selected from the SFR and $M_\star$ maps discussed in Section 3.1, to better isolate XRB populations as a function of sSFR, and decompose the XLFs into the SFR-scaled HMXB and $M_\star$-scaled LMXB components. Hereafter, we make the assumption that the X-ray point-source population that is not part of the CXB is dominated by XRBs; however, we note that there will be some contribution from other sources, in particular supernova remnants (SNRs) and Galactic stars. Unfortunately, a clean identification of the nature of every point source in our catalog is beyond the scope of this work. However, we expect that the contributions of these sources to the XLFs will be smaller than CXB sources (see, e.g., Figure 10 of Long et al. 2014 for M83) and will therefore not have a major impact on our conclusions.

To address the above goal, we began by generating *local sSFR maps* on the pixel scale of our SFR and $M_\star$ maps. For each pixel, we computed the total SFR and $M_\star$ within a square $500 \times 500$ pc$^2$ region, centered on the pixel. Such pixels have sizes of $3.5 \times 3.5$ arcsec$^2$ pixel$^{-1}$ for the most distant galaxy in the sample, NGC 5713, to $29.5 \times 29.5$ arcsec$^2$ pixel$^{-1}$ for the nearest galaxy, M81. Thus, each pixel can be used to signify the "local" conditions surrounding a given location, all on the same physical scale. Using these maps, we sorted all pixels for all galaxies into bins of sSFR with bin width, or "resolution," of $\Delta$ log sSFR $= 0.16$ dex, which is the rms error on the SFR and $M_\star$ calibration uncertainties (see Section 2 for details). For the lowest and highest sSFR bins, we required that at least one X-ray source be detected within and placed no limits on the respective lower and upper bounds for the inclusion of sSFR pixels in those bins. In total, we identified 21 sSFR bins, continuously covering the sSFR range from $\approx 2.5 \times 10^{-13}$ yr$^{-1}$ to $\approx 1.6 \times 10^{-9}$ yr$^{-1}$. The bins contain between 14 and 260 X-ray sources per bin. For each of the sSFR bins, we selected all pixels within the galactic regions (defined in Table 1) that were within the sSFR range of

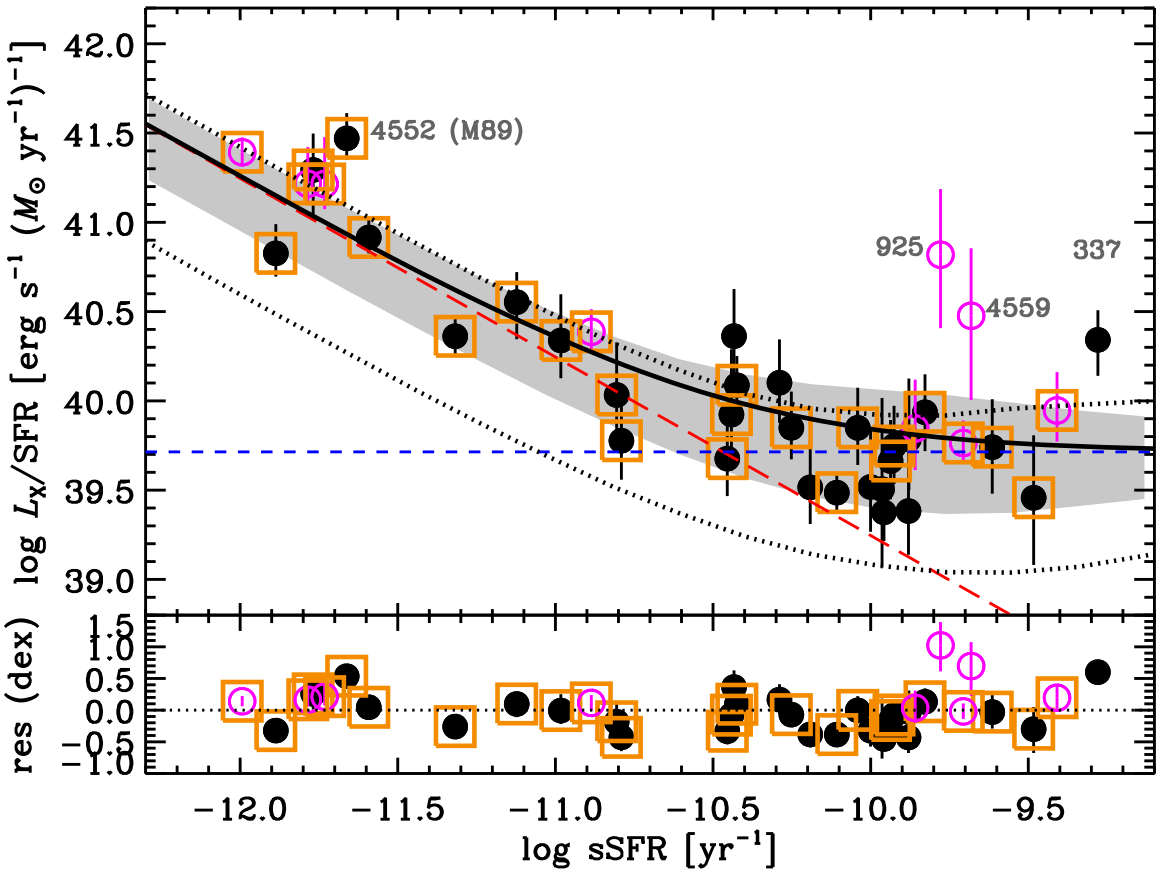


**Figure 6.** Top: integrated point-source 0.5–8 keV luminosity per unit SFR, $L_X$/SFR, vs. sSFR for the fits to the individual galaxies, as described in Section 4.1. Symbols have the same meaning as they did in Figure 5. Predictions from our best-fit global model (black solid curve; see Section 4.2), along with its contributions from LMXBs (red long-dashed curve) and HMXBs (blue short-dashed curve), are displayed and residuals between individual galaxy $L_X$ and global model prediction is plotted in the bottom panel. The gray shaded region shows the expected $1\sigma$ scatter due to XLF sampling for galaxies with the median mass $M_\star = 2 \times 10^{10}\,M_\odot$ (see Section 5.3 for details); galaxies above this limit are highlighted with orange squares. The dotted curves in the top panel show the expected $1\sigma$ scatter for galaxies with stellar masses equal to $3 \times 10^9\,M_\odot$; 95% of our galaxies are above this limit. In general, galaxy-to-galaxy scatter is comparable to that expected from XLF sampling; however, notable exceptions at low sSFR (e.g., NGC 4552) and high sSFR (e.g., NGC 337, NGC 925, and NGC 4559) are observed.

that bin and calculated the total SFR and $M_\star$ corresponding to those pixels.

In Figure 7, we show an array of observed SFR-normalized cumulative XLFs for the 21 sSFR bins. From this representation, it is clear that the XRB XLF both declines in normalization per unit SFR and becomes shallower in overall slope with increasing sSFR, as described in Section 4.1.

Assuming that these trends are driven by changes in the relative LMXB to HMXB populations, we chose to fit all 21 sSFR-binned XLFs globally using a single XLF model that self-consistently describes the contributions from each XRB population. For a given bin of sSFR, the XLF is modeled using the following set of equations:

$$\frac{dN}{dL} = \xi(L)\left[\frac{dN_{\rm LMXB}}{dL} + \frac{dN_{\rm HMXB}}{dL} + {\rm CXB}\right] \quad (10)$$

$$\frac{dN_{\rm HMXB}}{dL} = {\rm SFR}\,K_{\rm HMXB}\begin{cases} L^{-\gamma} & (L < L_c) \\ 0, & (L \geqslant L_c) \end{cases} \quad (11)$$

$$\frac{dN_{\rm LMXB}}{dL} = M_\star\,K_{\rm LMXB}\begin{cases} L^{-\alpha_1} & (L < L_b) \\ L_b^{\alpha_2-\alpha_1}L^{-\alpha_2}, & (L_b \leqslant L < L_c), \\ 0, & (L \geqslant L_c) \end{cases} \quad (12)$$

where Equations (11) and (12) mirror Equations (3) and (4), respectively. In this case, $K_{\rm HMXB}$ and $K_{\rm LMXB}$ are, respectively, normalizations per unit SFR ($[M_\odot\ {\rm yr}^{-1}]^{-1}$) and $M_\star$ ($[10^{11}\,M_\odot]^{-1}$) at $L = 10^{38}$ erg s$^{-1}$. Here, since our data set is much more expansive than for individual galaxies, we are able to perform fitting for seven parameters: $K_{\rm LMXB}$, $\alpha_1$, $L_b$, $\alpha_2$, $K_{\rm HMXB}$, $\gamma$, and $L_c$. We utilize the same statistical methodology for determining the best-fit solution and parameter uncertainties and minimize $C$ following

$$C = 2\sum_{i=1}^{n_{\rm sSFR}}\left(\sum_{j=1}^{n_{\rm X}} M_{i,j} - N_{i,j} + N_{i,j}\ln(N_{i,j}/M_{i,j})\right), \quad (13)$$

where $C$ is now determined "globally" through the double summation over all $n_{\rm sSFR} = 21$ sSFR bins ($i$th index) and $n_{\rm X} = 100$ X-ray luminosity bins ($j$th index; see Section 4.1 for details related to luminosity binning).

In Figure 8 we show the best-fit values, PDFs, and parameter correlations for the above model, and in Table 4 we tabulate parameter values from this model. Figure 9 shows the culled differential raw numbers of sources in luminosity bins of $\Delta\ \log L = 0.057$ dex, with Poisson errors plotted (derived following Gehrels 1986). This distribution is compiled from all galaxies in our sample, which have varying *Chandra* exposures, completeness functions, and properties (e.g., sSFR). In total, our data set contains 2478 X-ray-detected point sources. Our model suggests that 1230, 710, and 537 of the

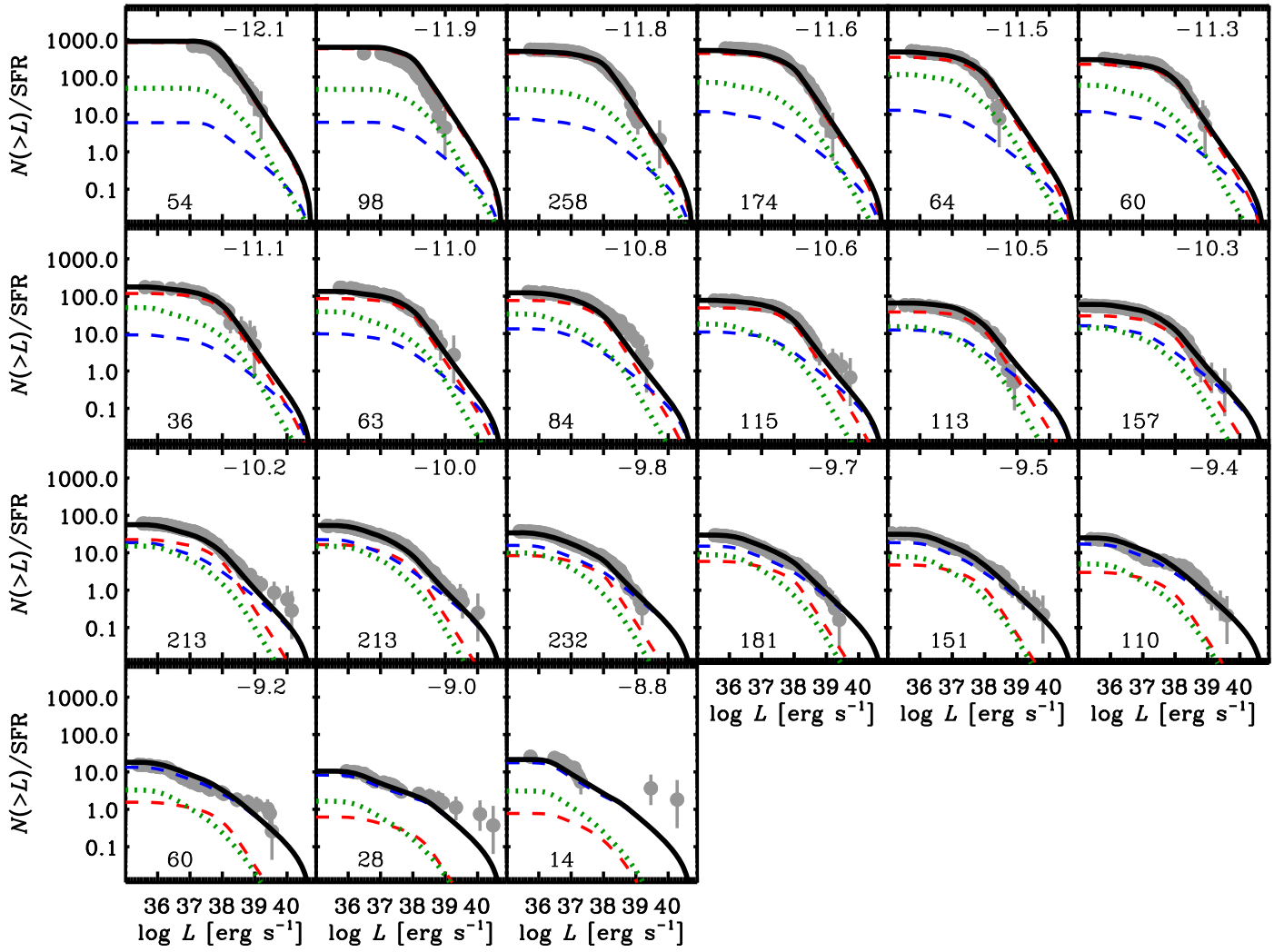


**Figure 7.** Observed SFR-normalized cumulative XLFs as a function of sSFR. In each panel, the observed XLFs (gray circles with $1\sigma$ error bars) were generated by culling X-ray sources from subgalactic regions within all the galaxies in our sample that had log sSFR ($yr^{-1}$) values annotated in the upper right corners of each panel. The numbers of X-ray-detected sources are annotated in the lower left corners of each panel. The XLFs were normalized by the cumulative SFR from the sSFR-selected subgalactic regions, as described in Section 3.2. Our best-fit global model is shown with black solid curves, and the contributions from the CXB (green dotted curves), LMXBs (red long-dashed curves), and HMXBs (blue short-dashed curves) are included. From the top left panel to the bottom right panel, the SFR-normalized XLFs both decline in normalization and become shallower in slope, as the population shifts from LMXB to HMXB dominated.

sources are LMXB, HMXB, and CXB sources, respectively. In a cumulative sense, our overall model (black curve) reproduces very well the raw distribution of source counts, including the complex contours associated with incompleteness. However, our fits are based on minimizing $C$ from Equation (13), which requires fitting a decomposition of these data into 21 such curves, binned by sSFR. Using the Kaastra (2017) prescription for evaluating goodness of fit, based on `cstat`, we find that the best-fit for the 21 sSFR and 100 $L_X$ bins is an acceptable model to the ensemble data set, with $P_{\rm null} = 0.145$.

We further present the calculated parameters,

$$\beta_{\rm HMXB} \equiv \frac{1}{\rm SFR}\int_{L_{\rm lo}}^{L_{\rm c}} \frac{dN_{\rm HMXB}}{dL}\, L\, dL = L_{\rm X}({\rm HMXB})/{\rm SFR}$$

and

$$\alpha_{\rm LMXB} \equiv \frac{1}{M_\star}\int_{L_{\rm lo}}^{L_{\rm c}} \frac{dN_{\rm LMXB}}{dL}\, L\, dL = L_{\rm X}({\rm LMXB})/M_\star, \quad (14)$$

two widely used scaling relations, in Figure 8 and Table 4. In Figure 5 we show the model-implied XLF slopes and SFR-normalized XLF normalizations for HMXB and LMXB populations, and in Figure 6 we display the implied $L_X$/SFR versus sSFR relation based on the $\alpha_{\rm LMXB}$ and $\beta_{\rm HMXB}$ model values. For the galaxies where we expect the XLFs to be well sampled (i.e., those with $M_\star > 2\times10^{10}$ $M_\odot$ or SFR $> 2$ $M_\odot$ $yr^{-1}$; orange boxes in Figures 5 and 6), we find that the galaxy-by-galaxy XLF parameters follow the global model expectation, in which the high-luminosity slopes ($\alpha_2$), SFR-normalized XLF normalizations ($K$/SFR), and $L_X$/SFR transition from LMXB-like at low sSFR to HMXB-like at high sSFR. Galaxies with lower $M_\star$ or SFR show more significant scatter away from the average trend, and in Section 5.3 below we examine closely the significance of this scatter.

In Figure 7, we display the sSFR-dependent best-fit cumulative XLF model fits to the data, including contributions from LMXB, HMXB, and CXB components. Our model

reproduces the trends and basic shapes of these curves well, going from a low-sSFR XLF with relatively high normalization per SFR and broken power-law shape to a high-sSFR XLF with low normalization per SFR and single-sloped power-law shape.

In Figure 10, we show the cumulative XLFs for all 38 galaxies in our sample (same as Figure 3) with the predicted XLFs from our global model overlaid. That is, the modeled XLF for a given galaxy is generated using our best global solution, which is based on simultaneous fitting to the 21 sSFR-selected subgalactic regions, along with the galaxy-wide completeness function, SFR, $M_\star$, and sky area. As such, the X-ray data for a given galaxy are not used in these models, aside from its minor influence on the global model solution itself (see below). In Table 5, we provide the `cstat` value and null-hypothesis probability, $P_{\rm Null}^{\rm global}$, for the X-ray data for each galaxy, and for convenience of comparison, we retabulate the $P_{\rm Null}$ values from the best-fit single and broken power-law models (Cols. (12) and (14), respectively). With a few notable exceptions, which we will discuss in Section 5.2 below, the global XLF model predicts very well the XLFs of several galaxies (considering the model is not tuned to any one galaxy individually). In fact, for several cases (24 out of the 38), the global model produces an equivalent or better statistical characterization (in terms of $P_{\rm Null}$; compare Col. (4) with Cols. (12) and (14) of Table 5) of the X-ray data than the best-fit power-law models in Section 3.2! Some notable cases include NGC 3031 (M81), NGC 5194 (M51), NGC 5236 (M83), and NGC 5457 (M101), all of which include more than 100 X-ray sources detected and are better characterized by our global model due to the somewhat complex contours that naturally result from the varying contributions from HMXBs and LMXBs.

To test the level of agreement between our global model and the observed XLFs of each galaxy, we fit a "scaled" version of the global model to each of our galaxies. In this model, we fixed the shape of the model XLF, implied by the global model and the SFR and $M_\star$ of the galaxy, but varied the normalization of the XLF by a constant factor, $\omega$, such that

$$\frac{dN_{\rm XRB}}{dL}|_{\rm scaled} = \omega\left(\frac{dN_{\rm LMXB}}{dL} + \frac{dN_{\rm HMXB}}{dL}\right). \quad (15)$$

An $\omega = 1$ implies that no additional scaling of the global model is needed. Using this form of the XRB XLF in the overall model provided in Equation (10), we fit for only $\omega$ following the procedures defined above. In Figure 11, we display the value of the scaling constant versus NGC name. We find that all but three galaxies (NGC 337, NGC 925, and NGC 4552) have $\omega$ consistent with unity to within a factor of two. For the rest of the galaxies, there is some scatter in $\omega$ around unity (as required by the global model fit itself) of $\approx$0.14 dex, which is consistent with the SFR and $M_\star$ calibration uncertainty (i.e., $\approx$0.16 dex; see gray band in Figure 11). The three galaxies with substantial deviations will be analyzed in more detail in Section 5.2.

Since the global model describes well the majority of the galaxy XLFs in our sample, it is unlikely that our average XLF scalings suffer from major galaxy sample variance. However, to test for any notable variations between subsets, we divided our sample into two subsets, retaining the NGC ordering in Table 1, and reran our global XLF calculations. In Table 4, we present the results from this run (see "First Subsample" and "Second Subsample" parameters). Although some minor differences are found, the parameters and computed properties ($\alpha_{\rm LMXB}$ and $\beta_{\rm HMXB}$) are consistent between subsamples at the $1\sigma$ level.

## 5. Discussion

### 5.1. Comparison with Previous Results and Population Synthesis Models

Our constraints on the HMXB and LMXB XLFs are similar in form to those presented in past works (see, e.g., Section 1 and references therein). However, as mentioned in Section 1, this is the first systematic attempt to decompose the XLF into LMXB and HMXB components for a sample of mainly late-type galaxies, regardless of their galaxy-wide sSFR. Furthermore, our XLF analyses contain a somewhat larger sample of galaxies and include ultradeep data from several galaxies that were not available in past studies. Notably, this provides (1) a unique characterization of the LMXB XLF appropriate for late-type galaxies, which may not necessarily be consistent with the LMXB XLF derived from elliptical galaxies (see Section 1), and (2) a cleaner characterization of the HMXB XLF shape, down to faint limits. Here we examine the differences between our XLFs and those reported in the literature.

For the HMXB XLFs, we chose to compare with M12, who derive HMXB parameters based on 1055 X-ray sources (including $\approx$700 XRBs) in a sample of 29 nearby galaxies with sSFR $> 10^{-10}$ yr$^{-1}$ in an attempt to avoid LMXB contributions. For the LMXB XLF, we compare with the Z12 study of 20 elliptical galaxies, including a total of 1626 X-ray sources (including $\approx$1580 XRBs).[15] We note that the Z12 LMXB XLF uses a broken power-law model with two breaks at $L_{\rm b,1} \approx 5 \times 10^{37}$ erg s$^{-1}$ and $L_{\rm b,2} \approx 6 \times 10^{38}$ erg s$^{-1}$, instead of the one break at $\approx 5 \times 10^{37}$ erg s$^{-1}$ that is used in our model. We experimented with an LMXB XLF that involved two breaks but found poor constraints on the two separate break locations and no improvement to the overall quality of the fits to our data. As such, we compare our LMXB XLF parameters $\alpha_1$, $\alpha_2$, and $L_b$ with the Z12 parameters derived below their $L_{b,2}$ (e.g., our $L_b$ is compared with their $L_{b,1}$).

In Figure 8, we highlight comparison parameter values from the literature with blue crosses, representing $1\sigma$ error bars, as reported in the literature; these comparisons are tabulated in Table 4. We find that the parameters of our LMXB XLF are similar to those of Z12, except that we favor a somewhat higher normalization and steeper faint-end slope ($\alpha_1$). These differences, combined with our lack of a third steep power-law component at high $L$, yield a somewhat larger estimate for the integrated LMXB X-ray luminosity per unit mass, $\alpha_{\rm LMXB}$;

[15] We note that the M12 and Z12 XLFs were derived using a Salpeter (1955) IMF, which produces SFR and $M_\star$ values that differ from our Kroupa (2001) IMF by factors of 1.56 and 1.24, respectively. When making comparisons, we have corrected published values by these factors. We also note that the assumed conversion factors that we use here to compute physical properties (e.g., UV plus IR tracer of SFR) differ somewhat from those used by M12 and Z12. M12 make use of Bell (2003) when determining SFR, and Z12 utilize Bell & de Jong (2001) for $M_\star$, while we use Hao et al. (2011) and Zibetti et al. (2009) for SFR and $M_\star$, respectively. The only non-negligible differences come from the $M_\star$ conversion factors for the bluest regions, where the Bell & de Jong (2001) $M/L_K$ is up to a factor of $\sim$10 times higher (although typically much less discrepant) than that used by Zibetti et al. (2009). We have chosen to not make adjustments based on these conversion factors, when comparing XLF properties, due to the complex form and nontrivial influence on the results; however, we point out that some discrepancies between results may in part be due to these assumptions.

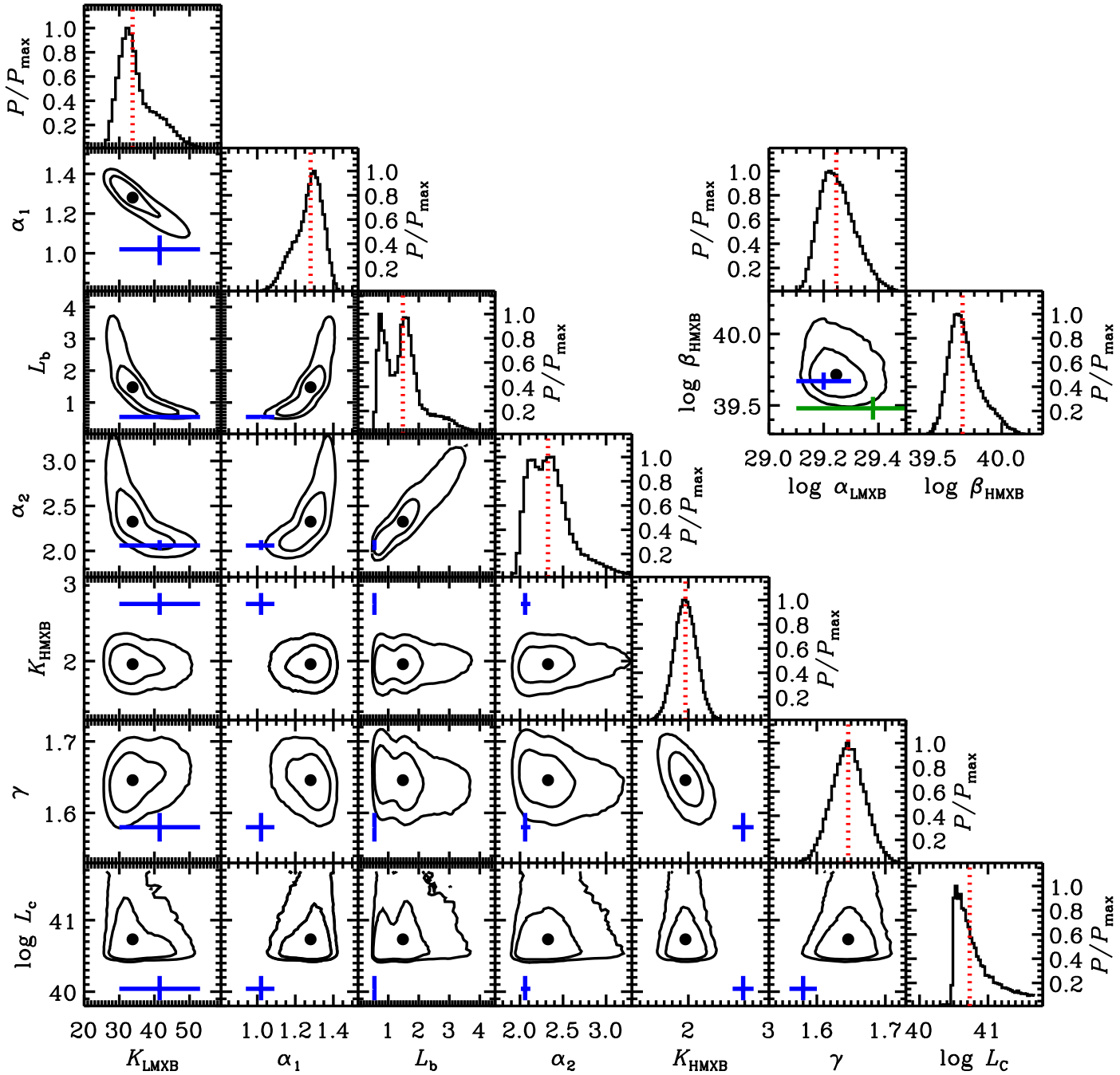


**Figure 8.** PDFs ($P/P_{max}$) and confidence contours for parameter pairs (showing 68% and 95% confidence contours drawn) for our best-fit global model, which is based on fits to 21 sSFR-selected subgalactic regions (see Section 4.2 for complete details). The vertical red dotted lines and filled black points indicate the median values of each parameter, which are adopted as our best global model. The 2D parameter correlation distributions include the seven free parameters ($K_{LMXB}$, $\alpha_1$, $L_b$, $\alpha_2$, $K_{HMXB}$, $\gamma$, and $L_c$) that were fit with our global model. The distribution functions for the integrated $L_X(LMXB)/M_\star$ ($\alpha_{LMXB}$) and $L_X(HMXB)/SFR$ ($\beta_{HMXB}$), implied by our model, are shown in the top right panels. Comparison values and $1\sigma$ errors from M12 and Z12 for HMXB and LMXB parameters are indicated with blue crosses, and the Chandra Deep Field-South independent estimates of $\alpha_{LMXB}$ and $\beta_{HMXB}$ from Lehmer et al. (2016) are shown with a green cross representing the $1\sigma$ range.

however, our estimates are consistent with those of Z12 within the uncertainties (see top right panel of Figure 8). For the HMXBs, our fit parameters significantly differ from those reported by M12, due primarily to a preference for a steeper slope ($\gamma$) and lower normalization ($K_{HMXB}$) for our sample. These parameters are anticorrelated in such a way that the integrated X-ray luminosity per unit SFR $\beta_{SFR}$ is in good agreement with that of M12.

To reveal any unmodeled complex features in the shapes of the XLFs and more clearly compare differences with those from M12 and Z12, we created Figure 12, which shows our HMXB and LMXB XLFs in differential form. These "clean" HMXB and LMXB XLFs were created by (1) extracting the observed XLFs from regions with sSFR $> 10^{-10}$ yr$^{-1}$ and sSFR $< 3 \times 10^{-11}$ yr$^{-1}$, respectively; (2) subtracting the low-level model components related to LMXB and HMXB

**Table 4**
Best-fit Parameters for Global Fits

| Parameter Name (1) | Units (2) | First Subsample (3) | Second Subsample (4) | Cleaned Sample (5) | Full Sample (6) | M12/Z12 Value (7) |
|---|---|---|---|---|---|---|
| SFR | $M_\odot$ yr$^{-1}$ | 18.5 | 26.9 | 40.9 | 45.4 | ... |
| $M_\star$ | $10^{11}$ $M_\odot$ | 7.97 | 4.50 | 10.21 | 12.47 | ... |
| log sSFR | log yr$^{-1}$ | $-10.63$ | $-10.22$ | $-10.40$ | $-10.44$ | ... |
| $N_{\rm det}$ | | 852 | 1626 | 2071 | 2478 | ... |
| | | | Parameter Fit Values | | | |
| $K_{\rm LMXB}$ | $(10^{11}\ M_\odot)^{-1}$ | $32.3^{+5.7}_{-5.7}$ | $39.6^{+2.1}_{-2.0}$ | $26.0^{+3.4}_{-2.4}$ | $33.8^{+7.3}_{-3.6}$ | $41.5 \pm 11.5$ |
| $\alpha_1$ | ... | $1.21^{+0.08}_{-0.08}$ | $1.31^{+0.03}_{-0.04}$ | $1.31^{+0.05}_{-0.07}$ | $1.28^{+0.06}_{-0.09}$ | $1.02^{+0.07}_{-0.08}$ |
| $L_b$ | $10^{38}$ erg s$^{-1}$ | $0.77^{+0.39}_{-0.16}$ | $3.27^{+0.51}_{-0.55}$ | $2.16^{+1.39}_{-0.71}$ | $1.48^{+0.70}_{-0.66}$ | $0.546^{+0.043}_{-0.037}$ |
| $\alpha_2$ | ... | $2.15^{+0.15}_{-0.11}$ | $3.15^{+0.56}_{-0.42}$ | $2.57^{+0.54}_{-0.28}$ | $2.33^{+0.27}_{-0.21}$ | $2.06^{+0.06}_{-0.05}$ |
| $L_{b,2}$[a] | $10^{38}$ erg s$^{-1}$ | ... | ... | ... | ... | $5.99^{+0.95}_{-0.67}$ |
| $\alpha_3$[a] | ... | ... | ... | ... | ... | $3.63^{+0.67}_{-0.49}$ |
| $K_{\rm HMXB}$ | $(M_\odot\ {\rm yr}^{-1})^{-1}$ | $2.43^{+0.27}_{-0.27}$ | $1.48^{+0.14}_{-0.14}$ | $2.06^{+0.16}_{-0.15}$ | $1.96^{+0.14}_{-0.14}$ | $2.68 \pm 0.13$ |
| $\gamma$ | ... | $1.53^{+0.05}_{-0.05}$ | $1.71^{+0.03}_{-0.03}$ | $1.66^{+0.02}_{-0.02}$ | $1.65^{+0.03}_{-0.02}$ | $1.58 \pm 0.02$ |
| log $Lc$ | log erg s$^{-1}$ | $40.5^{+0.4}_{-0.1}$ | $41.0^{+0.5}_{-0.3}$ | $40.8^{+0.5}_{-0.2}$ | $40.7^{+0.4}_{-0.2}$ | $40.04^{+0.18}_{-0.16}$ |
| $C$ | ... | 1014 | 1185 | 1331 | 1410 | ... |
| $P_{\rm null}$ | ... | 0.705 | 0.017 | 0.177 | 0.145 | ... |
| | | | Calculated Parameters | | | |
| log $\alpha_{\rm LMXB}$ | log erg s$^{-1}$ $M_\odot^{-1}$ | $29.14^{+0.07}_{-0.06}$ | $29.31^{+0.05}_{-0.04}$ | $29.15^{+0.07}_{-0.05}$ | $29.25^{+0.07}_{-0.06}$ | $29.2 \pm 0.1$ |
| log $\beta_{\rm HMXB}$ | log erg s$^{-1}$ $(M_\odot\ {\rm yr}^{-1})^{-1}$ | $39.89^{+0.15}_{-0.11}$ | $39.56^{+0.15}_{-0.13}$ | $39.73^{+0.15}_{-0.10}$ | $39.71^{+0.14}_{-0.09}$ | $39.67 \pm 0.06$ |

**Notes.** Cols. (1) and (2): parameter and units. Cols. (3)–(6): value of each parameter for the first subsample, second subsample, "'cleaned" sample, and full sample of sources. The two subsamples represent fits based on simply dividing the full sample in half, when ordered by NGC name. The first and second subsamples include NGC 337–4321 and NGC 4450–7552, respectively. The cleaned sample excludes galaxies with low metallicity (NGC 337, NGC 925, NGC 3198, NGC 4536, and NGC 4559) and galaxies with relatively large GC $S_N$ (NGC 1404, NGC 4552, and NGC 4594). Col. (7): comparison values of HMXB and LMXB scaling relations from M12 and Z12, respectively.
[a] Parameter was used in Z12, but not in our study.

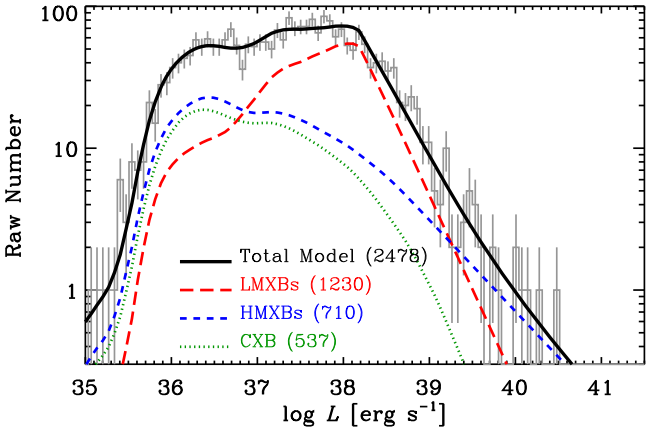


**Figure 9.** Raw number of sources detected as a function of X-ray luminosity $L$, in bins of $\Delta$ log $L = 0.057$ dex. The shape of this curve is dependent on the XRB XLFs, contributions from the CXB, and varying depths of *Chandra* observations across the galaxy sample. The cumulative model, based on summing contributions from all sSFR bins, is shown as a solid curve, with HMXB (blue short-dashed), LMXB (red long-dashed), and CXB (green dotted) components indicated. The total number of sources predicted by each model component is annotated in the key. For comparison, the total number of sources detected in the sample above $10^{35}$ erg s$^{-1}$ is 2478, which is very close to that predicted (see annotation).

populations, respectively, as well as the CXB model components; and (3) unfolding our data using the completeness functions generated in Section 3.3. The data points in Figure 12 represent the unfolded data and $1\sigma$ Poisson errors in the top panels and the ratio of the data to our best-fit models in the bottom panels. We further display the M12 and Z12 models for comparison.

Clearly, the sSFR $> 10^{-10}$ yr$^{-1}$ HMXB data (Figure 12(a)) show a complex shape beyond that described by a simple power-law model. The HMXB XLF can be better described as rapidly declining ($\gamma > 1.6$) between $L = 10^{36}$ and $10^{38}$ erg s$^{-1}$ and following a more exponential-like decline above $L = 10^{38}$ erg s$^{-1}$. We found that this shape was preserved when changing our sSFR selection limits. For example, the HMXB XLFs for regions with log sSFR$= -10$ to $-9.5$ and log sSFR $> -9.5$ both show the same basic shapes (see bottom panels of Figure 12(a)). Such a change in slope of the HMXB XLF has been predicted by previous population synthesis models (e.g., Tzanavaris et al. 2013; Zuo et al. 2014; Artale et al. 2018) and is potentially due to a dominance in wind-fed, young ($\lesssim$20 Myr) BH-HMXBs.

The sSFR $< 10^{-10}$ yr$^{-1}$ LMXB data (Figure 12(b)) appear to be generally consistent with the model across the full luminosity range. However, when we examine the data over different sSFR intervals, we see that the residuals are somewhat more complex and indicate that the high-luminosity ($L \gtrsim 3 \times 10^{37}$ erg s$^{-1}$) LMXB XLF slope gets shallower with increasing sSFR (see bottom panels of Figure 12(b)). This is consistent with a scenario where higher-sSFR regions harbor younger populations of LMXBs that reach higher luminosities than older LMXB populations (e.g., Fragos et al. 2008; Kim & Fabbiano 2010; Lehmer et al. 2014, 2017).

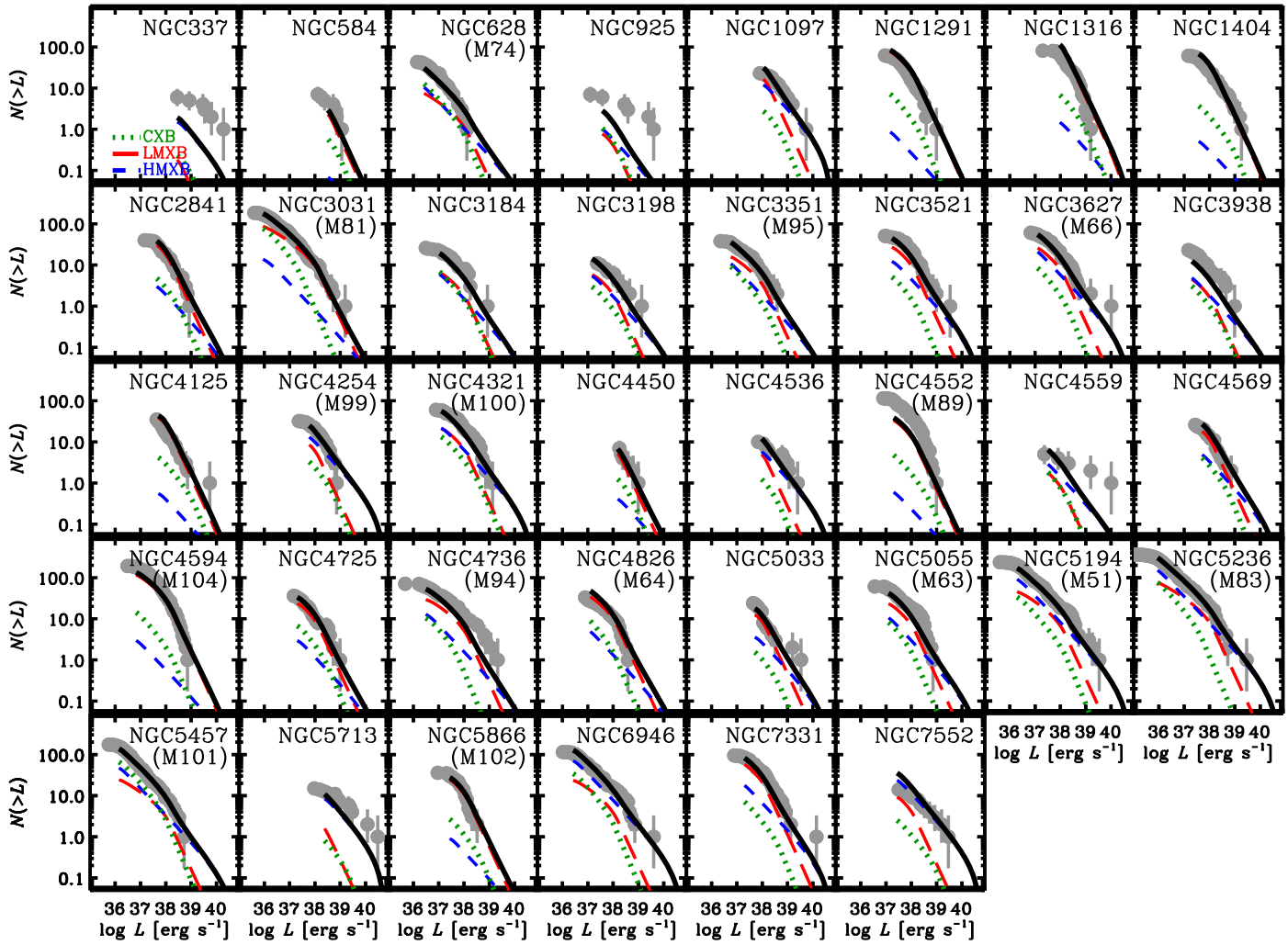


**Figure 10.** Observed galaxy-wide cumulative XLFs (gray points with $1\sigma$ Poisson error bars), displayed the same as in Figure 3, but with our global decomposition model predictions plotted (black solid curves). Our model is detailed in Section 4.2 and consists of contributions from the CXB (green dotted curves), LMXBs (red long-dashed curves), and HMXBs (blue short-dashed curves), the normalizations of which scale with galaxy area, $M_{\star}$, and SFR, respectively. For all cases, the global XLF model provides a good description of the overall XLF shapes, with the exceptions where the XLF data are elevated over the model, which we suspect is due to anomalously low metallicity (e.g., NGC 4559) or a relatively large population of GC LMXBs (e.g., NGC 4552).

### 5.2. Variations in the Galaxy-wide XLFs

As described in Section 4.2, there are a few galaxies for which the global model does not provide a good description of the data (see $P_{\rm Null}$ in Col. (4) of Table 5). For many of these galaxies, the differences between the model and data are within the uncertainties of the SFR or stellar mass calibrations (see Figure 11), but there are three examples (NGC 337, NGC 925, and NGC 4552) where the XLFs are dramatically discrepant with the model, $P_{\rm Null} < 0.01$, resulting in galaxy luminosities that are dramatically offset from the average relation shown in Figure 6. As detailed by Gilfanov et al. (2004) and Justham & Schawinski (2012), a shallow-sloped XLF can produce large variations in the distributions of bright XRBs, and thus $L_{\rm X}$, if the XLF is poorly sampled. Such poor XLF sampling is likely to be prevalent in low-SFR galaxies, where the shallow-sloped HMXB XLF will be poorly sampled at the high-$L$ end. To a less important degree, low-$M_{\star}$ galaxies, which are dominated by LMXBs (i.e., with low sSFRs), may also suffer from poor XLF sampling, but this is less important than it is for HMXBs, due to the steep XLF slope at high $L$. Nonetheless, it is instructive to quantify to what degree the XRB XLFs and implied integrated $L_{\rm X}$ of our galaxies can be influenced by simple statistical sampling scatter of the HMXB and LMXB XLFs, so that we can identify objects that are clear outliers.

For each galaxy in our sample, we performed a 1000-trial Monte Carlo analysis to construct probability distributions of the summed point-source X-ray luminosity, $L_{\rm ps}$, as well as the cumulative number of sources detected above $10^{38}$ and $10^{39}$ erg s$^{-1}$, $N_{38}$ and $N_{39}$, respectively, assuming that the XRBs in the galaxy follow our global model XLF (e.g., the black curves in Figure 10). For a given Monte Carlo trial, we first perturbed the SFR and $M_{\star}$ values of a given galaxy (starting with the values in Cols. (11) and (12) of Table 1) in accordance with a Gaussian distribution of fractional $1\sigma$ uncertainties of 0.1 and 0.13 dex, respectively, corresponding to the uncertainties on the calibrations (see Section 3.1). We note that distance-related uncertainties could affect our calculations of SFR, $M_{\star}$ and $L$. The median distance-related uncertainty on these quantities is $\approx$0.06 dex (with a range of 0.004–0.2 dex), which is the size of our X-ray luminosity bins and significantly smaller than the calibration uncertainties on SFR and $M_{\star}$. Furthermore, since distance-related errors affect SFR and $M_{\star}$ in the same way that they affect $L$ (and integrated $L_{\rm X}$), the impact of the distance-related uncertainties is

**Table 5**
Global X-Ray Luminosity Function Fits by Galaxy

| Galaxy Name (NGC) (1) | Alt Name (2) | Global Model | | | | | Scaled Global Model | | | Power Law | | | |
|---|---|---|---|---|---|---|---|---|---|---|---|---|---|
| | | $C$ (3) | $P_{\rm Null}$ (4) | $P(L_{\rm ps})$ (5) | $P(N_{38})$ (6) | $P(N_{39})$ (7) | $\omega$ (8) | $C$ (9) | $P_{\rm Null}$ (10) | $C$ (11) | $P_{\rm Null}^{\rm PL}$ (12) | $C$ (13) | $P_{\rm Null}^{\rm BKNPL}$ (14) |
| 337 | ⋯ | 29 | <0.001 | 0.034 | … | 0.005 | $3.82^{+1.57}_{-1.22}$ | 23 | 0.440 | 22 | 0.944 | 23 | 0.889 |
| 584 | ⋯ | 9 | 0.899 | 0.719 | … | 0.189 | $1.68^{+0.97}_{-0.71}$ | 9 | 0.478 | 11 | 0.686 | 9 | 0.169 |
| 628 | M74 | 32 | 0.543 | 0.720 | 0.852 | 0.360 | $1.52^{+0.37}_{-0.32}$ | 30 | 0.239 | 31 | 0.106 | 26 | 0.109 |
| 925 | ⋯ | 33 | <0.001 | 0.045 | 0.067 | 0.004 | $3.28^{+1.44}_{-1.12}$ | 30 | 0.067 | 26 | 0.785 | 25 | 0.849 |
| 1097 | ⋯ | 32 | 0.730 | 0.742 | … | 0.308 | $0.69^{+0.17}_{-0.15}$ | 29 | 0.814 | 25 | 0.261 | 33 | 0.387 |
| 1291 | ⋯ | 37 | 0.853 | 0.924 | 0.942 | 0.776 | $0.66^{+0.10}_{-0.09}$ | 27 | 0.389 | 36 | 0.162 | 25 | 0.173 |
| 1316 | ⋯ | 54 | 0.001 | 0.995 | … | 0.938 | $0.55 \pm 0.07$ | 29 | 0.852 | 28 | 0.383 | 28 | 0.383 |
| 1404 | ⋯ | 36 | 0.517 | 0.715 | 0.930 | 0.385 | $0.77^{+0.11}_{-0.10}$ | 32 | 0.781 | 27 | 0.061 | 27 | 0.047 |
| 2841 | ⋯ | 25 | 0.630 | 0.774 | 0.724 | 0.781 | $0.82^{+0.17}_{-0.15}$ | 24 | 0.585 | 24 | 0.218 | 24 | 0.283 |
| 3031 | M81 | 44 | 0.503 | 0.362 | 0.567 | 0.206 | $0.90 \pm 0.12$ | 43 | 0.486 | 50 | 0.034 | 43 | 0.092 |
| 3184 | ⋯ | 35 | 0.527 | 0.428 | 0.049 | 0.440 | $1.20^{+0.38}_{-0.33}$ | 35 | 0.670 | 37 | 0.782 | 34 | 0.773 |
| 3198 | ⋯ | 31 | 0.639 | 0.392 | 0.230 | 0.139 | $0.74^{+0.30}_{-0.25}$ | 30 | 0.477 | 30 | 0.748 | 28 | 0.851 |
| 3351 | M95 | 20 | 0.035 | 0.609 | 0.471 | 0.507 | $1.03^{+0.23}_{-0.20}$ | 20 | 0.034 | 23 | 0.008 | 21 | 0.032 |
| 3521 | | 39 | 0.642 | 0.386 | 0.091 | 0.494 | $1.04^{+0.17}_{-0.15}$ | 39 | 0.666 | 45 | 0.545 | 30 | 0.267 |
| 3627 | M66 | 44 | 0.498 | 0.221 | 0.215 | 0.282 | $1.04^{+0.16}_{-0.14}$ | 44 | 0.516 | 45 | 0.554 | 41 | 0.738 |
| 3938 | ⋯ | 27 | 0.790 | 0.294 | 0.118 | 0.470 | $1.96^{+0.50}_{-0.43}$ | 23 | 0.244 | 23 | 0.056 | 23 | 0.219 |
| 4125 | ⋯ | 33 | 0.511 | 0.506 | 0.949 | 0.498 | $0.69^{+0.14}_{-0.12}$ | 29 | 0.794 | 26 | 0.458 | 28 | 0.796 |
| 4254 | M99 | 16 | 0.036 | 0.823 | 0.287 | 0.917 | $1.13^{+0.25}_{-0.22}$ | 16 | 0.027 | 16 | 0.017 | 15 | 0.019 |
| 4321 | M100 | 42 | 0.697 | 0.497 | 0.073 | 0.563 | $1.03^{+0.17}_{-0.15}$ | 42 | 0.712 | 44 | 0.363 | 36 | 0.399 |
| 4450 | | 12 | 0.485 | 0.823 | … | 0.548 | $1.18^{+0.54}_{-0.42}$ | 12 | 0.399 | 13 | 0.464 | 12 | 0.148 |
| 4536 | ⋯ | 23 | 0.953 | 0.568 | … | 0.254 | $0.83^{+0.32}_{-0.25}$ | 23 | 0.819 | 22 | 0.604 | 22 | 0.693 |
| 4552 | M89 | 99 | <0.001 | 0.062 | <0.001 | 0.603 | $2.83^{+0.29}_{-0.27}$ | 32 | 0.675 | 40 | 0.002 | 35 | 0.068 |
| 4559 | ⋯ | 26 | 0.203 | 0.053 | 0.455 | 0.017 | $0.82^{+0.54}_{-0.39}$ | 25 | 0.142 | 20 | 0.668 | 20 | 0.768 |
| 4569 | ⋯ | 20 | 0.280 | 0.860 | 0.703 | 0.771 | $0.77^{+0.21}_{-0.18}$ | 19 | 0.259 | 20 | 0.132 | 19 | 0.255 |
| 4594 | M104 | 40 | 0.944 | 0.401 | 0.234 | 0.814 | $1.39^{+0.11}_{-0.10}$ | 26 | 0.071 | 59 | 0.707 | 22 | 0.010 |
| 4725 | ⋯ | 30 | 0.938 | 0.495 | 0.687 | 0.591 | $0.91^{+0.21}_{-0.18}$ | 30 | 0.952 | 31 | 0.274 | 30 | 0.694 |
| 4736 | M94 | 57 | 0.077 | 0.165 | 0.089 | 0.047 | $1.15^{+0.18}_{-0.16}$ | 57 | 0.115 | 55 | 0.554 | 52 | 0.842 |
| 4826 | M64 | 31 | 0.672 | 0.861 | 0.672 | 0.613 | $0.49^{+0.13}_{-0.12}$ | 20 | 0.143 | 25 | 0.044 | 17 | 0.023 |
| 5033 | | 33 | 0.226 | 0.339 | 0.513 | 0.124 | $1.31^{+0.30}_{-0.25}$ | 32 | 0.453 | 30 | 0.884 | 31 | 0.424 |
| 5055 | M63 | 35 | 0.988 | 0.376 | 0.043 | 0.682 | $1.33^{+0.21}_{-0.19}$ | 33 | 0.637 | 34 | 0.101 | 33 | 0.215 |
| 5194 | M51 | 53 | 0.895 | 0.427 | 0.319 | 0.215 | $1.18^{+0.10}_{-0.09}$ | 50 | 0.751 | 49 | 0.034 | 48 | 0.062 |
| 5236 | M83 | 52 | 0.650 | 0.597 | 0.274 | 0.652 | $0.95 \pm 0.07$ | 51 | 0.635 | 57 | 0.073 | 54 | 0.182 |
| 5457 | M101 | 38 | 0.288 | 0.553 | 0.373 | 0.649 | $1.18^{+0.17}_{-0.15}$ | 37 | 0.207 | 38 | 0.019 | 37 | 0.088 |
| 5713 | ⋯ | 32 | 0.142 | 0.135 | … | 0.167 | $1.20^{+0.37}_{-0.30}$ | 32 | 0.259 | 29 | 0.456 | 30 | 0.638 |
| 5866 | M102 | 21 | 0.322 | 0.810 | 0.492 | 0.562 | $1.13^{+0.23}_{-0.20}$ | 21 | 0.282 | 26 | 0.214 | 17 | 0.188 |
| 6946 | ⋯ | 60 | 0.237 | 0.481 | 0.271 | 0.602 | $0.74 \pm 0.10$ | 54 | 0.415 | 53 | 0.289 | 52 | 0.552 |
| 7331 | ⋯ | 50 | 0.117 | 0.216 | 0.137 | 0.518 | $1.04^{+0.12}_{-0.11}$ | 50 | 0.126 | 56 | 0.710 | 50 | 0.703 |
| 7552 | ⋯ | 47 | 0.148 | 0.803 | 0.934 | 0.519 | $0.36^{+0.12}_{-0.10}$ | 30 | 0.803 | 28 | 0.190 | 27 | 0.351 |

**Note.** Goodness of fit assessments for all galaxies, based on our global model, scaled global model, and power-law fits. Cols. (1) and (2): galaxy NGC and Messier name, as reported in Table 1. Cols. (3) and (4): $C$-statistic and null-hypothesis probability for the best global model (see Section 4.2 for details), which is based on only the SFR and $M_\star$ of the galaxy. Cols. (5)–(7): probabilities of observing the total detected point-source luminosity $L_{\rm ps}$, total number of sources brighter than $L = 10^{38}$ erg s$^{-1}$, and total number of sources brighter than $L = 10^{39}$ erg s$^{-1}$, respectively, if the data are drawn from the global model. The probabilities are based on Monte Carlo simulations, which include the effects of statistical variance and uncertainty in SFR and $M_\star$ calibrations (see Section 5.2 for detailed description). Col. (8): constant scaling factor $\omega$ and its $1\sigma$ error. The constant scaling factor for a given galaxy multiplies by the XLF predicted by the global model, following Equation (15). A value of $\omega = 1$ indicates consistency with the global model. Cols. (9) and (10): $C$-statistic and null-hypothesis probability for the scaled global model. Cols. (11)–(14): $C$-statistic and null-hypothesis probability pairs for power-law and broken power-law models. These columns are retabulations of Cols. (8)–(9) and Cols. (13)–(14) from Table 3.

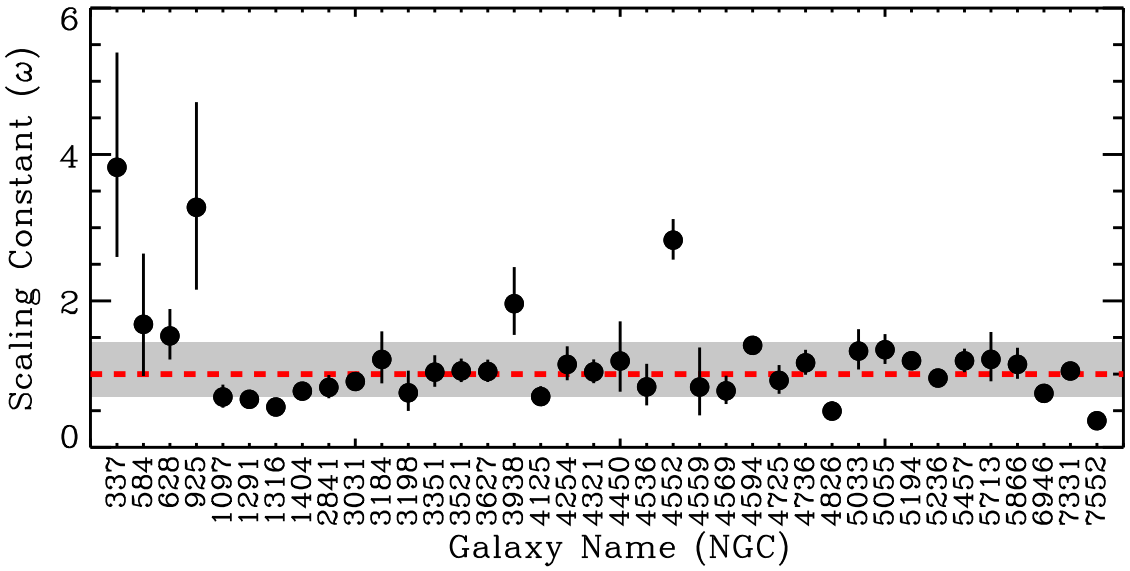


**Figure 11.** Best-fitting global model scaling constant, $\omega$, vs. NGC-designated galaxy name. The red dashed line at $\omega = 1$ and gray band of width 0.16 dex, respectively, indicate the expected value from the global model and the combined calibration uncertainty of the SFR and $M_\star$. Only a few galaxies, NGC 337, NGC 925, and NGC 4552, are clear outliers with $\omega > 2$ (see discussion of these sources in Section 5.2).

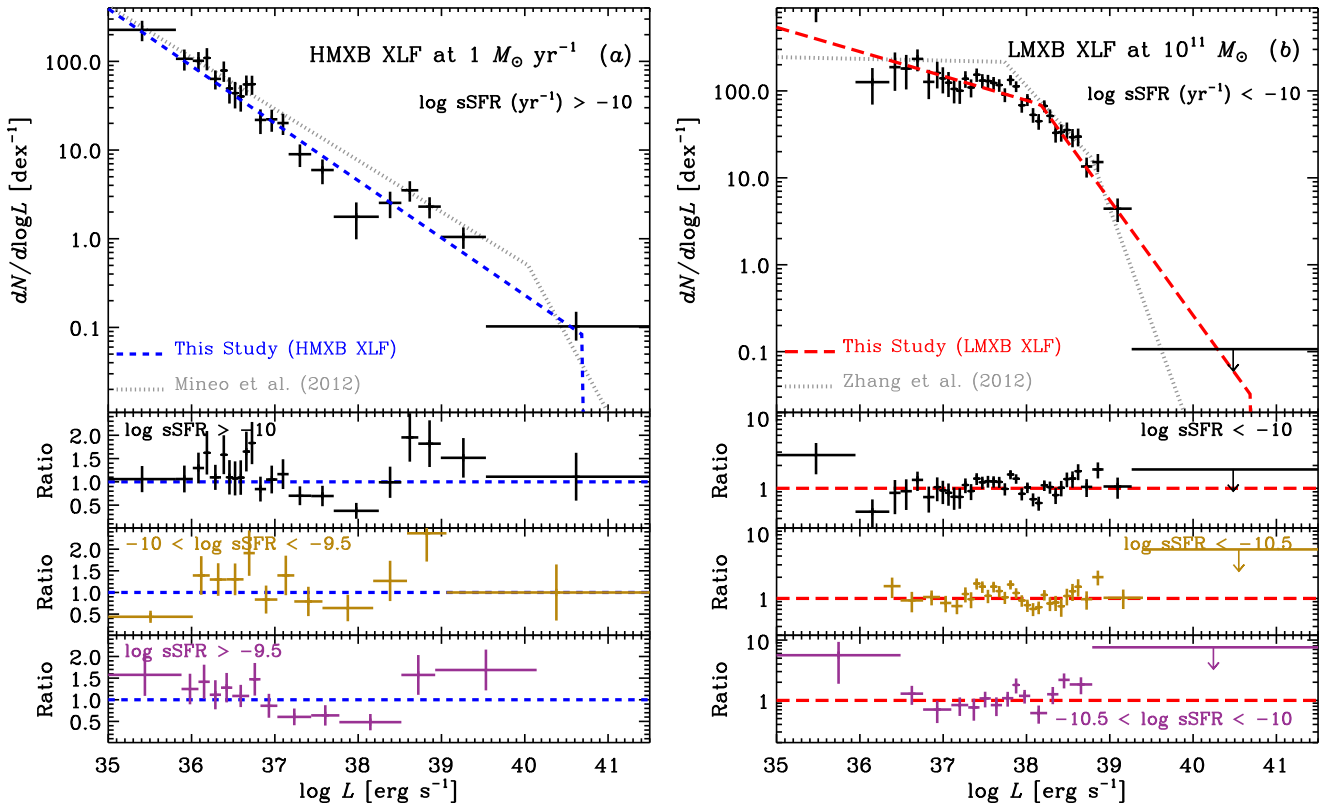


**Figure 12.** (a) Top: constraints on the HMXB XLF, based on subgalactic regions with sSFR $> 10^{-10}$ yr$^{-1}$. The data points and $1\sigma$ Poisson error bars represent completeness-corrected and CXB and LMXB model-subtracted constraints on the HMXB XLF, normalized to an SFR $= 1$ $M_\odot$ yr$^{-1}$. The blue short-dashed curve shows our best-fit model, and the dotted curve shows the Mineo et al. (2012b) constraint. Bottom panels show the data-to-model ratio, based on different sSFR ranges (see annotations). (b) Top: constraints on the LMXB XLF, based on subgalactic regions with sSFR $< 10^{-10}$ yr$^{-1}$. The data points and $1\sigma$ Poisson error bars represent completeness-corrected and CXB and HMXB model-subtracted constraints on the LMXB XLF, normalized to $M_\star = 10^{11}$ $M_\odot$. The red long-dashed curve shows our best-fit model, and the dotted curve shows the Zhang et al. (2012) constraint from elliptical galaxies. Bottom panels show the data-to-model ratio, based on different sSFR ranges (see annotations).

substantially reduced. We therefore ignore these uncertainties in our simulations. Using the perturbed values of SFR and $M_\star$, along with our best-fit global model, CXB estimates, and completeness functions, we calculated the numbers of HMXBs, LMXBs, and CXB sources with $L > 10^{36}$ erg s$^{-1}$ that we would expect to detect.

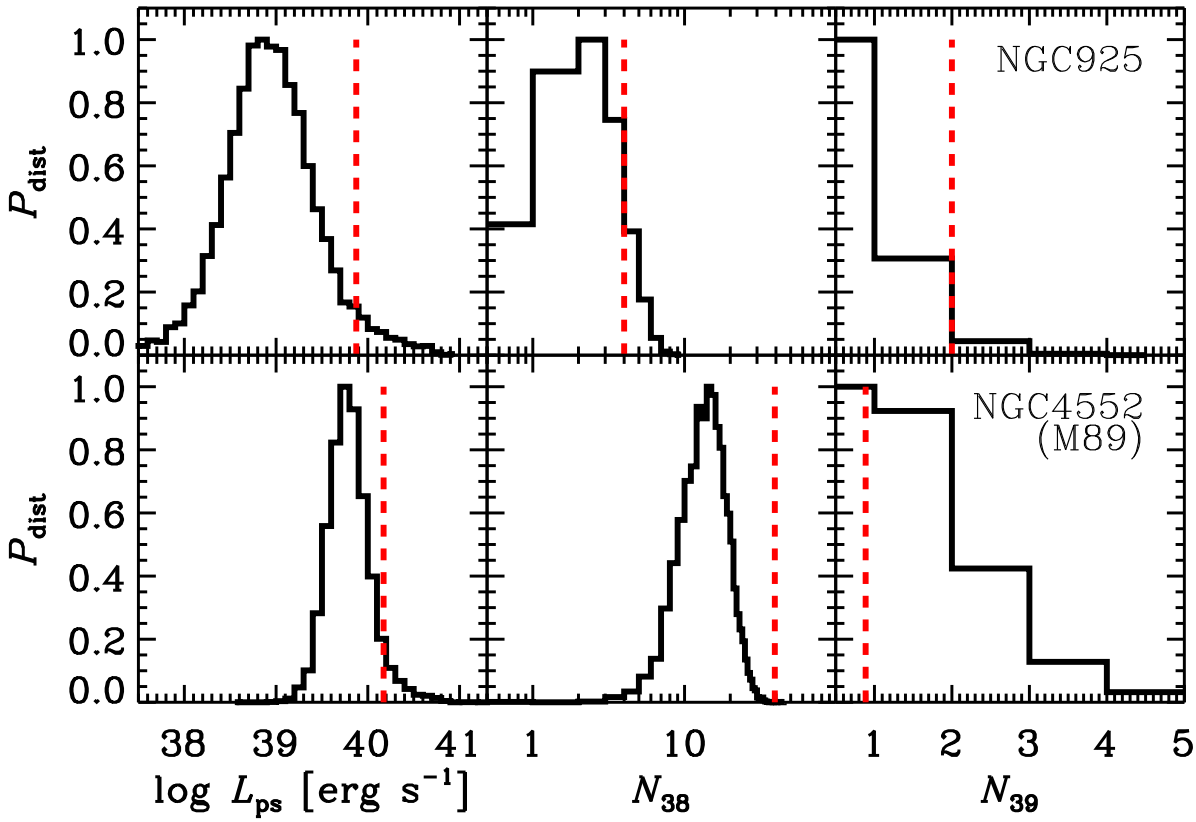


**Figure 13.** Sample of Monte Carlo *predicted* probability distributions of point-source luminosities we would expect to detect ($L_{ps}$; left panels), and numbers of such sources above $10^{38}$ erg s$^{-1}$ ($N_{38}$; middle panels) and $10^{39}$ erg s$^{-1}$ ($N_{39}$; right panels), based on our global best-fit models of NGC 925 (top) and NGC 4552 (bottom). The observed values of each parameter are shown as vertical red dashed lines. These galaxies exhibit the most statistically significant deviations away from the global model, beyond statistical scatter (see Table 5 for specific probability values). For NGC 925 an excess of $L > 10^{39}$ erg s$^{-1}$ sources are observed, potentially due to the galaxy's relatively low metallicity (see Section 5.2.1). For NGC 4552, an excess of $L > 10^{38}$ erg s$^{-1}$ sources is observed, potentially due to a correspondingly large population of GC LMXBs (see Section 5.2.2).

We perturbed these numbers using Poisson statistics and calculated numbers of HMXBs, LMXBs, and CXB sources ($N^{\rm MC}_{\rm HMXB}$, $N^{\rm MC}_{\rm LMXB}$, and $N^{\rm MC}_{\rm CXB}$) for the Monte Carlo trial. Using the integrated HMXB, LMXB, and CXB XLF components as probability distributions, we assigned each of the $N^{\rm MC}_{\rm HMXB}$, $N^{\rm MC}_{\rm LMXB}$, and $N^{\rm MC}_{\rm CXB}$ sources luminosity values to construct a simulated list of X-ray point sources for the trial. The simulated list provides a simulation of the observed XLF, $N_{\rm ps}(L)$ (e.g., equivalent to the gray data points in Figure 10), and the source list luminosities can be summed to yield expected total point-source luminosities: $L^{\rm MC}_{\rm ps} = L^{\rm MC}_{\rm LMXB} + L^{\rm MC}_{\rm HMXB} + L^{\rm MC}_{\rm CXB}$.

Our Monte Carlo procedure, run 1000 times per galaxy, thus provides probability distributions of $N_{\rm ps}(L)$ and $L_{\rm ps}$. To identify potential outliers, we computed three quantities: $P(L_{\rm ps})$, $P(N_{38})$, and $P(N_{39})$, which are the probabilities of observing a population of sources above the measured $L_{\rm ps}$, $N_{38}$, and $N_{39}$, respectively, given the model. The values of these probabilities are provided for each galaxy in Cols. (5)–(7) of Table 5.

Given that there are 38 galaxies in our full sample, we expect that these probability values may span $0.03 \lesssim P \lesssim 0.97$ due to random scatter. Sources outside of this range are good candidates for outliers that do not follow the relation owing to some inherently different physical property beyond just statistical variance. For our sample, we find four cases where $P < 0.03$: NGC 337, NGC 925, NGC 4552, and NGC 4559. NGC 337, NGC 925, and NGC 4559 are high-sSFR galaxies that show an excess of $L > 10^{39}$ erg s$^{-1}$ point sources, while NGC 4552 is a low-sSFR elliptical galaxy that shows a significant excess of $L > 10^{38}$ erg s$^{-1}$ point sources. Figure 13 shows example probability distributions for the three quantities for NGC 925 and NGC 4552, along with their observed values. Comparisons of the properties of these galaxies with the rest of the sample reveal two compelling physical reasons why these galaxies would be offset from the global model distribution: the effects of low metallicity on HMXB formation or large contributions from GC LMXB populations. Below, we discuss each of these scenarios in turn.

#### 5.2.1. Enhanced HMXBs in Low-metallicity Galaxies

In terms of metallicity, NGC 337, NGC 925, and NGC 4559 are among the five galaxies with the lowest metallicities in our sample, together with NGC 3198 and NGC 4536. These five galaxies have metallicities that are around $\approx 1/2\ Z_{\odot}$, factors of 0.4–0.5 times the median metallicity of our sample, and all have relatively small values of $P(N_{39})$, indicating a likely excess of luminous sources within the subpopulation. Within this subsample, we detected 12 X-ray point sources with $L > 10^{39}$ erg s$^{-1}$, whereas $\approx$4 were expected from our global model. From our Monte Carlo simulations, the probability of obtaining 12 sources with $L > 10^{39}$ erg s$^{-1}$ is $\approx$0.2%, suggesting that the low-metallicity sample as a whole contains an excess of luminous point sources. For comparison, the total point-source luminosity $L_{\rm ps}$ and number of sources with

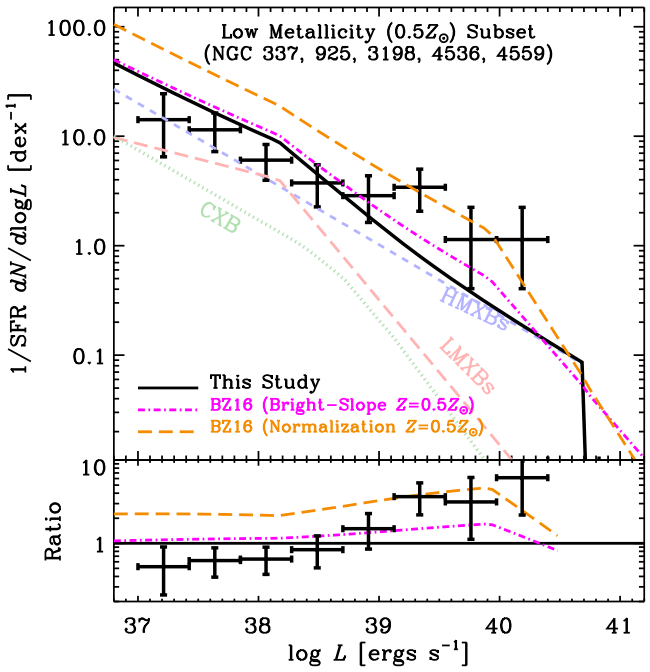


**Figure 14.** Top: SFR-normalized total XLF for the five lowest-metallicity galaxies in our sample (NGC 337, NGC 925, NGC 3198, NGC 4536, and NGC 4559), which have metallicities of $\approx$0.5 $Z_\odot$. The data points and 1$\sigma$ error bars are corrected for completeness but include contributions from HMXBs, LMXBs, and CXB sources. The black curve shows our global model prediction for this population, including HMXB, LMXB, and CXB contributions in faded blue, red, and green, respectively. Enhancements in the $L \gtrsim 10^{39}$ erg s$^{-1}$ source population are clearly observed. The BZ16 model predictions for enhancements of 0.5 $Z_\odot$ HMXB populations are overlaid for scenarios where the canonical M12 HMXB XLF normalization increases (orange dashed curve) or bright-end slope flattens (magenta dotted–dashed curve) with decreasing metallicity (see Section 5.2.1 for details). Bottom: ratio of data and BZ16 models with respect to our best-fit global model prediction.

$L > 10^{38}$ erg s$^{-1}$ are consistent with expectations from the global model, $P(L_{\rm ps}) = 7\%$ and $P(N_{38}) = 55\%$, respectively, suggesting that the enhanced population is limited to the most luminous sources.

A more detailed view of the low-metallicity XLF is displayed in Figure 14, which shows the combined completeness-corrected, SFR-normalized XLF for the five lowest-metallicity galaxies in our sample. In Figure 14, we overlay our best-fit global model XLF, which includes contributions from HMXBs, LMXBs, and CXB sources (faded blue, red, and green curves). The global model predicts that the XLF of the low-metallicity galaxies is dominated by HMXBs above $L \sim 10^{38}$ erg s$^{-1}$. A factor of $\approx$2–10 times excess of sources over the global model is observed for $L \gtrsim 5 \times 10^{38}$ erg s$^{-1}$ for the low-metallicity subset, with the largest and most significant excess measured around $3 \times 10^{39}$ erg s$^{-1}$. Thus, the HMXB XLF of low-metallicity galaxies takes on an enhanced "hump" above the global model at $L \gtrsim 10^{39}$ erg s$^{-1}$.

Qualitatively similar enhancements were observed by Basu-Zych et al. (2016, BZ16) in the $L \gtrsim 10^{40}$ erg s$^{-1}$ XLFs of low-metallicity Lyman break analog (LBA) galaxies Haro 11 and VV 114, and the relatively nearby low-metallicity galaxy NGC 3310 (e.g., Miralles-Caballero et al. 2014) appears to show a similar excess of $L \gtrsim 10^{38}$ erg s$^{-1}$ sources compared to the M12 relation (see, e.g., Figure 14 of M12). Using the LBA observations, combined with measurements of $L_{\rm X}$/SFR versus metallicity from the literature (Basu-Zych et al. 2013a; Brorby et al. 2014; Douna et al. 2015), BZ16 constructed two model scenarios for the low-metallicity XLF consistent with the data. These models include an HMXB XLF that (1) flattens or extends the shallow high-luminosity slope to brighter limits ($\gtrsim 10^{40}$ erg s$^{-1}$; hereafter "bright-slope") or (2) increases in normalization, as the metallicity decreases. Both scenarios result in a rise in $L_{\rm X}$/SFR with decreasing metallicity consistent with the $L > 10^{40}$ erg s$^{-1}$ LBA XLFs, the HMXB XLF of typical galaxies (based on M12), and the observed $L_{\rm X}$/SFR versus metallicity correlation, which is also consistent with the Fragos et al. (2013b) population synthesis predictions for the $L_{\rm X}$/SFR versus metallicity relation.

In Figure 14, we show both BZ16 predictions (i.e., varying bright slope and normalization with metallicity) for the $\approx 1/2\ Z_\odot$ HMXB XLF, with model contributions from LMXB and CXB sources added for fair comparison with our data. The bottom panel of Figure 14 shows the ratio of the low-metallicity galaxy data from this study and BZ16 models compared to our best-fit global model. While the BZ16 models produce elevated HMXB XLF predictions, neither scenario describes well our overall XLF constraints for the $\approx 1/2\ Z_\odot$ galaxies in our sample. As noted above, the excess of sources in the low-metallicity sample appears to begin at $L \gtrsim 10^{39}$ erg s$^{-1}$, roughly an order of magnitude below that in the BZ16 bright-slope model (magenta dotted–dashed curve). Furthermore, the BZ16 enhanced normalization model nicely fits the enhanced $L > 10^{39}$ erg s$^{-1}$ hump but does not predict the return to the global XLF level at $L \lesssim 10^{39}$ erg s$^{-1}$. It is currently not clear if the overall observed trend of increasing $L_{\rm X}$/SFR with declining metallicity can be attributed to a smooth development and enhancement of the XLF hump we observe here. It is also possible that more complex changes occur in the HMXB XLF shape with metallicity. Despite this, a more systematic study of how the HMXB XLF varies as a function of metallicity is tractable but would require a sample of galaxies that span a broader range of metallicity compared to those in this study. Such an investigation, as well as its implications for XRB population synthesis models, will be the subject of future work.

### 5.2.2. Enhanced LMXBs in Massive Elliptical Galaxies

In addition to the statistically significant enhancement of $N_{39}$ for HMXBs in the lowest-metallicity galaxies in our sample, we also find enhancements in the LMXB populations for some of the early-type galaxies. Most notably, NGC 4552, which has an E-type morphology, is observed to have a statistically significant excess of low-luminosity LMXBs, $N_{38}$, compared to the global model prediction (see bottom panels of Figure 13). For massive early-type galaxies like NGC 4552, it has been shown by several authors (e.g., Harris 1991; Bekki et al. 2006; Peng et al. 2008; Harris et al. 2013) that the number of GCs per unit stellar mass can be enhanced and vary significantly from galaxy to galaxy. In such galaxies, the contributions from dynamically formed LMXBs coincident with GCs can dominate the XLF of the galaxy (see, e.g., Kim & Fabbiano 2004; Irwin 2005; Juett 2005; Lehmer et al. 2014; Peacock et al. 2017). Although all galaxies in our sample are expected to contain some contributions from GC LMXBs, and our global model will include an average contribution from these GCs that is characteristic of the average number of GCs per unit mass, our global model will not accurately predict the LMXB XLF for galaxies with strong deviations from this average. As previous studies have shown, the

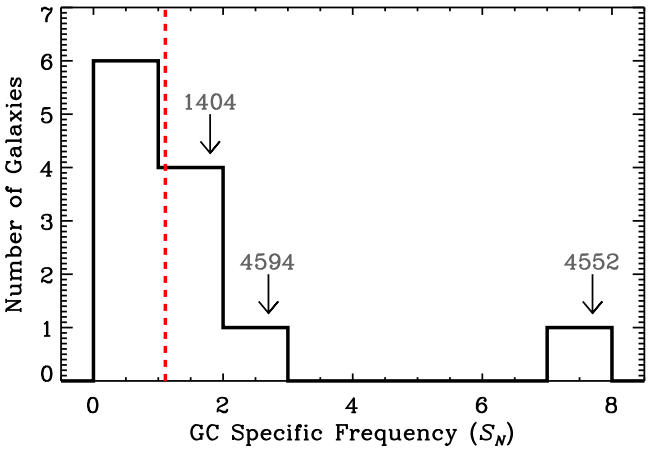


**Figure 15.** Distribution of GC specific frequencies, $S_N$, for 12 out of the 38 galaxies in our sample, based on published values from Harris et al. (2013). The locations and names of the three galaxies with the highest $S_N$ values have been annotated. NGC 4552 has the largest $S_N$ value of our sample and has a statistically significant excess of LMXBs compared to our global model expectation, suggesting that GC LMXBs dominate the XLF in this galaxy.

galaxies that are most likely to show deviations are massive ellipticals with relatively large dark matter halos (see, e.g., Harris et al. 2013).

To investigate the relative levels that GC LMXBs are likely contributing to the XLFs in each galaxy, we made use of the Harris et al. (2013) catalog of GC specific frequencies for nearby galaxies. The specific frequency, $S_N$, for a given galaxy is defined as

$$S_N \equiv N_{\rm GC} \times 10^{0.4(M_V^T+15)}, \quad (16)$$

where $N_{\rm GC}$ is the number of GCs in the galaxy and $M_V^T$ is the galaxy-wide total $V$-band absolute magnitude. In a broad sense, $S_N$, is a proxy for the number of GCs per unit mass. The Harris et al. (2013) catalog contains measurements of the GC populations, including $S_N$, for a comprehensive sample of 422 nearby galaxies. We found entries for 12 of the 38 galaxies in our sample, and we have added the $S_N$ values of these galaxies to Table 1. Not surprisingly, measurements were available for the nearest and most massive galaxies in the sample. Given general trends of $S_N$ versus $M_\star$, we would expect that the galaxies with available $S_N$ measurements would be biased toward high-mass galaxies, which tend to have high $S_N$. In Figure 15, we display the distribution of $S_N$ values for the sample, with the median value of $S_N^{\rm median} = 1.1$ indicated. Ten out of the 12 galaxies have $S_N < 2$, while the most significant outlier, NGC 4552, has an $S_N = 7.7$, far above the next highest $S_N = 2.7$ for NGC 4594.

In terms of deviations from the global LMXB XLF, it is interesting to note that the three galaxies with the highest $S_N$ values, NGC 1404, NGC 4552, and NGC 4594, all have elevated values of $N_{38}$, with the most extreme galaxy (in $S_N$ terms), NGC 4552, having a statistically significant enhancement of low-luminosity LMXBs. Given the known enhancements in LMXB populations generated by GC LMXBs, the above strongly implicates contributions from GC LMXBs as being responsible for the observed excess of LMXBs in NGC 4552 and possibly some of the other galaxies (e.g., NGC 1404 and NGC 4594). A more detailed analysis involving direct identification of GC counterparts (see, e.g., Kim & Fabbiano 2010; Lehmer et al. 2014; Peacock et al. 2017) would be required to quantify the level of influence GCs have on these galaxies. Such a paper is the subject of work currently in preparation (A. P. Ferrell et al. 2019, in preparation).

### 5.3. Characterizing the Statistical Scatter of the Global Model

The above analyses indicate that there are several galaxies that show statistically significant deviations of their XRB populations compared to the global model predictions; however, these deviations are strongly suggested to be attributed to unmodeled dependencies in metallicity and GC LMXB population contributions. In spite of these examples, the global model provides a good characterization of the XLFs for the majority of the galaxies in our sample (see Table 5). We can therefore use the global model to provide good estimates of the typical emission and scatter-related uncertainty from XRB populations in galaxies, given their SFR and $M_\star$ values. However, we note that these calculations are appropriate for galaxies with metallicities and GC specific frequencies close to the average values of our sample: $\langle Z \rangle \approx Z_\odot$ and $\langle S_N \rangle \approx 1.5$, respectively.

As a practical matter, for galaxies that are much more distant than those studied here, only the integrated $L_{\rm X}$ can be measured. In this section, we make use of our global XRB XLF model to predict $L_{\rm X}$ values, as well as their potential variations due to scatter, given only SFR and $M_\star$ values. As discussed at the beginning of Section 5.2, low-SFR or low-$M_\star$ populations are subject to large variations in measured $L_{\rm X}$ due to poorly populated HMXB and LMXB XLFs. For galaxies in these categories, the average scaling relations, $\alpha_{\rm LMXB} \equiv L_{\rm X}({\rm LMXB})/M_\star$ and $\beta_{\rm HMXB} \equiv L_{\rm X}({\rm HMXB})/{\rm SFR}$, are unlikely to give correct estimates of the integrated XRB population luminosities, since these are only accurate when the XLFs are fully populated.

To determine how $L_{\rm X}$ and its scatter would vary with SFR and $M_\star$, we followed closely the Monte Carlo procedure outlined above in Section 5.2. We first generated a grid of 15 sSFR values covering log sSFR ($\rm yr^{-1}$) $= -12.5$ to $-8.5$ and six $M_\star$ values ranging from log $M_\star(M_\odot) = 9$ to 11.5. These ranges cover broader ranges of galaxy properties than those found in our sample. For a given pairing of sSFR and $M_\star$, we ran our Monte Carlo simulation (see Section 5.2 for details) to generate simulated HMXB and LMXB source lists down to a luminosity limit of $L = 10^{35}$ erg $\rm s^{-1}$. Here we did not include completeness functions, as we had done in Section 5.2 above, since we are interested in the total intrinsic luminosity. Summing the luminosities of the populations gives Monte Carlo–based estimates of $L_{\rm X}$(HMXB), $L_{\rm X}$(LMXB), and $L_{\rm X}$ (i.e., the sum of HMXBs and LMXBs). For a given pair of sSFR and $M_\star$, we generated a total of 1000 $L_{\rm X}$(HMXB), $L_{\rm X}$(LMXB), and $L_{\rm X}$ values each and constructed PDFs.

In Figures 16(a) and (b), we display the $L_{\rm X}$(HMXB) versus SFR and $L_{\rm X}$(LMXB) versus $M_\star$, respectively, including the expected median (black solid curves) and scatter (i.e., gray shaded regions) in the relations, as well as the $\beta_{\rm HMXB}$ and $\alpha_{\rm LMXB}$ scaling relations for fully populated XLFs. For comparison, we include the locations of galaxies that are expected to be HMXB and LMXB dominant, based on having log sSFR ($\rm yr^{-1}$) $> -9.5$ and log sSFR ($\rm yr^{-1}$) $< -11.5$, respectively. As expected, the scatter and the deviations of

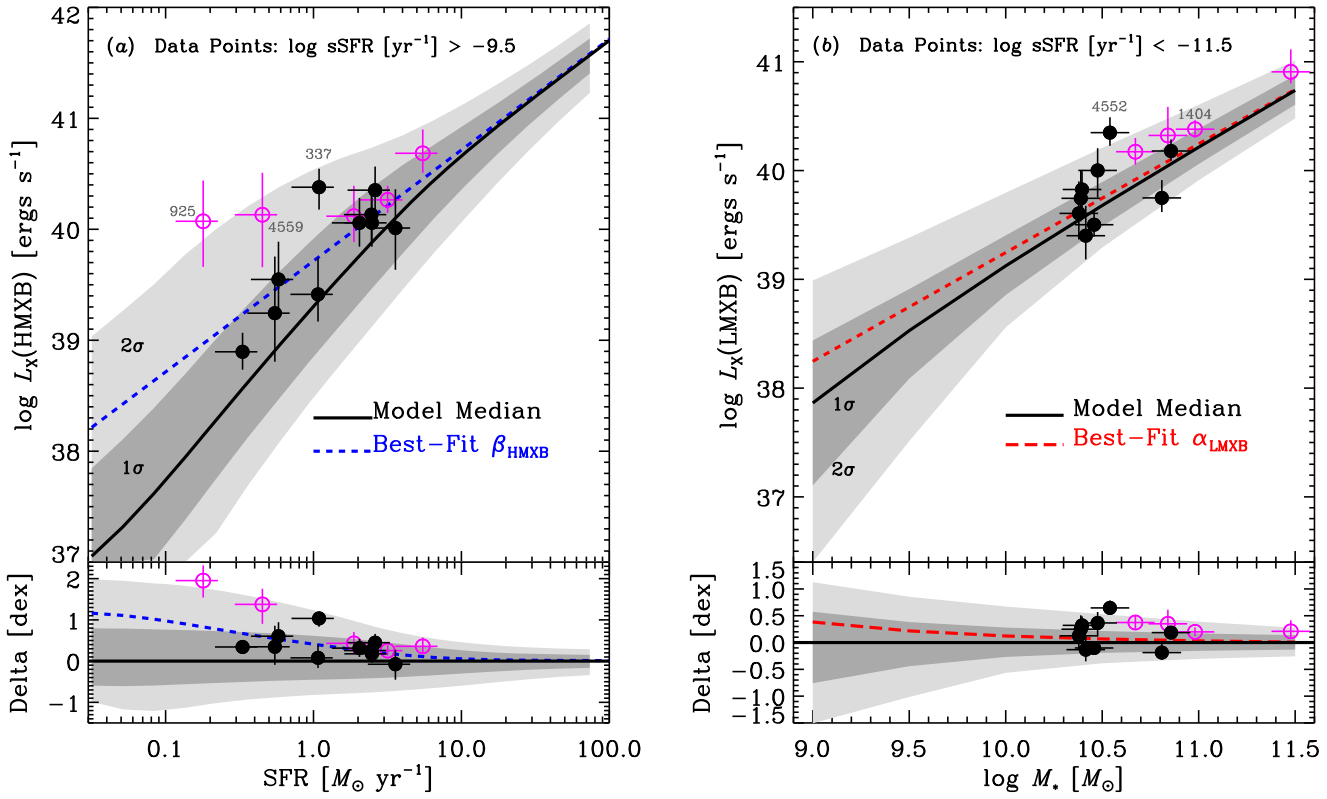


**Figure 16.** $L_X$(HMXB)–SFR (panel (a), top) and $L_X$(LMXB)–$M_\star$ (panel (b), top) relations based on our global model. The blue dashed and red long-dashed curves provide scaling relation predictions based on integration of the HMXB and LMXB XLFs, respectively: the $\beta_{HMXB}$ and $\alpha_{LMXB}$ values calculated from our global model (see Table 4). The predicted median values are shown as solid curves with 16%–84% (1$\sigma$; dark gray) and 2.5%–97.5% (2$\sigma$; light gray) confidence regions related to statistical scatter indicated. These values were calculated using Monte Carlo simulations of data sets generated by the global model and are described in detail in Sections 5.2 and 5.3. For reference, galaxies in our sample that are predicted to be dominated by HMXBs (log sSFR/yr$^{-1}$ > −9.5) and LMXBs (log sSFR/yr$^{-1}$ < −11.5) are shown, with known outliers annotated. The bottom panels show the log-scale residuals of all quantities with respect to the median relation, illustrating the level of scatter and relationship with SFR and $M_\star$. Note that the deviation of $\beta_{HMXB}$ and $\alpha_{LMXB}$ with respect to the median grows to larger than a factor of two for SFR $\lesssim 2\ M_\odot\ yr^{-1}$ and $M_\star \lesssim 3 \times 10^9\ M_\odot$.

the median $L_X$ from the respective relations grow with decreasing SFR or $M_\star$ owing to the XLF becoming less populated. These effects are larger in the HMXB–SFR scaling than for the LMXB-$M_\star$ scaling, since the relatively shallow-sloped HMXB XLF leads to large variations in $L_X$(HMXB), when the XLF is poorly populated. For HMXBs, the median $L_X$(HMXB) is lower than that implied by $\beta_{HMXB}$ by more than a factor of two for SFR $\lesssim 2\ M_\odot\ yr^{-1}$; all but seven of our galaxies have SFR values in this range. For LMXBs, the median $L_X$(LMXB) is a factor of two lower than that implied by $\alpha_{LMXB}$, only for galaxies with $M_\star \lesssim 3 \times 10^9\ M_\odot$; only four of our galaxies have stellar masses in this range. The scatter itself is in the range of ≈0.3–0.7 dex for HMXBs across SFR = 0.1–10 $M_\odot\ yr^{-1}$ and ≈0.2–0.4 for LMXBs across log $M_\star(M_\odot)$ = 9.5–11.

In Table 6, we tabulate the results of our Monte Carlo simulations. For a broad range of sSFR and $M_\star$ combinations, we provide the median (50%), 16%, and 84% confidence ranges for the total $L_X$, which contains contributions from both HMXBs and LMXBs. In Figure 6, we display the 16% and 84% ranges of $L_X$/SFR versus sSFR based on these results for the median stellar mass of our sample $M_\star = 2 \times 10^{10}\ M_\odot$ (gray shaded region) and for a low stellar mass bin at $M_\star = 3 \times 10^9\ M_\odot$ (dotted curves), above which 36 out of the 38 galaxies in our sample lie. As we examined in Section 5.2.1, the most significant outliers, like NGC 337, NGC 925, NGC 4552, and NGC 4559, are apparent owing to their enhanced $L_X$/SFR values over these ranges. Nevertheless, given values of $M_\star$ and SFR (and thus sSFR), the tabulated values in Table 6 can be used on a galaxy-by-galaxy basis to obtain a realistic estimate of the expected XRB $L_X$ and scatter-related uncertainty. As alluded to throughout all of Section 5, these parameterizations will be improved in the future with studies of how the XLF varies with additional physical properties, such as metallicity and $S_N$.

## 6. Summary

In this paper, we have utilized 5.8 Ms of *Chandra* data, combined with UV-to-IR observations, for 38 nearby ($D \lesssim 30$ Mpc) galaxies to revisit scaling relations of the HMXB and LMXB XLFs with SFR and $M_\star$, respectively. We make novel use of the local environment to isolate XRB populations in a variety of sSFR bins, which allows us to cleanly determine the HMXB and LMXB XLF shapes and normalizations. In addition to providing new details on XRB XLF scaling relations, which can be applied to a variety of astrophysical problems, this work presents several new data products and results, which we summarize below.

1. We present publicly available *Chandra* data products and catalogs, as well as SFR and $M_\star$ maps for all 38 galaxies in our sample. These products are constructed carefully following the procedures detailed in Section 3.

**Table 6**
Expected Statistical Scatter for Global Model

| | log $M_\star/M_\odot$ | | | | | |
|---|---|---|---|---|---|---|
| | (9.0) | (9.5) | (10.0) | (10.5) | (11.0) | (11.5) |
| log sSFR ($yr^{-1}$) | log $L_X$ (erg $s^{-1}$) | log $L_X$ (erg $s^{-1}$) | log $L_X$ (erg $s^{-1}$) | log $L_X$ (erg $s^{-1}$) | log $L_X$ (erg $s^{-1}$) | log $L_X$ (erg $s^{-1}$) |
| −12.5 | $37.86^{+0.76}_{-0.57}$ | $38.53^{+0.44}_{-0.38}$ | $39.13^{+0.27}_{-0.28}$ | $39.68^{+0.19}_{-0.22}$ | $40.22^{+0.15}_{-0.17}$ | $40.74^{+0.13}_{-0.14}$ |
| −12.3 | $37.86^{+0.75}_{-0.58}$ | $38.53^{+0.44}_{-0.39}$ | $39.13^{+0.27}_{-0.28}$ | $39.68^{+0.20}_{-0.22}$ | $40.22^{+0.15}_{-0.17}$ | $40.74^{+0.13}_{-0.14}$ |
| −12.1 | $37.86^{+0.76}_{-0.58}$ | $38.53^{+0.44}_{-0.39}$ | $39.13^{+0.27}_{-0.28}$ | $39.69^{+0.19}_{-0.22}$ | $40.22^{+0.16}_{-0.17}$ | $40.75^{+0.13}_{-0.14}$ |
| −11.9 | $37.86^{+0.75}_{-0.58}$ | $38.54^{+0.44}_{-0.39}$ | $39.13^{+0.27}_{-0.28}$ | $39.69^{+0.19}_{-0.22}$ | $40.23^{+0.15}_{-0.17}$ | $40.75^{+0.13}_{-0.14}$ |
| −11.7 | $37.88^{+0.76}_{-0.57}$ | $38.54^{+0.43}_{-0.39}$ | $39.14^{+0.27}_{-0.29}$ | $39.70^{+0.20}_{-0.22}$ | $40.24^{+0.16}_{-0.18}$ | $40.76^{+0.13}_{-0.14}$ |
| −11.4 | $37.88^{+0.75}_{-0.57}$ | $38.55^{+0.43}_{-0.39}$ | $39.14^{+0.27}_{-0.29}$ | $39.71^{+0.19}_{-0.23}$ | $40.25^{+0.16}_{-0.18}$ | $40.78^{+0.13}_{-0.14}$ |
| −11.2 | $37.89^{+0.75}_{-0.58}$ | $38.56^{+0.43}_{-0.39}$ | $39.16^{+0.27}_{-0.29}$ | $39.72^{+0.19}_{-0.23}$ | $40.27^{+0.16}_{-0.19}$ | $40.80^{+0.13}_{-0.14}$ |
| −11.0 | $37.90^{+0.73}_{-0.57}$ | $38.58^{+0.42}_{-0.39}$ | $39.18^{+0.26}_{-0.30}$ | $39.75^{+0.20}_{-0.24}$ | $40.30^{+0.16}_{-0.20}$ | $40.84^{+0.14}_{-0.15}$ |
| −10.8 | $37.93^{+0.72}_{-0.57}$ | $38.61^{+0.41}_{-0.40}$ | $39.22^{+0.27}_{-0.31}$ | $39.79^{+0.20}_{-0.27}$ | $40.35^{+0.17}_{-0.22}$ | $40.89^{+0.14}_{-0.15}$ |
| −10.6 | $37.97^{+0.68}_{-0.56}$ | $38.66^{+0.40}_{-0.41}$ | $39.27^{+0.27}_{-0.34}$ | $39.85^{+0.21}_{-0.30}$ | $40.43^{+0.18}_{-0.23}$ | $40.97^{+0.14}_{-0.15}$ |
| −10.4 | $38.04^{+0.64}_{-0.56}$ | $38.72^{+0.38}_{-0.42}$ | $39.34^{+0.27}_{-0.37}$ | $39.95^{+0.22}_{-0.33}$ | $40.53^{+0.19}_{-0.24}$ | $41.07^{+0.15}_{-0.14}$ |
| −10.2 | $38.14^{+0.59}_{-0.56}$ | $38.82^{+0.37}_{-0.45}$ | $39.45^{+0.28}_{-0.41}$ | $40.07^{+0.24}_{-0.35}$ | $40.67^{+0.20}_{-0.22}$ | $41.20^{+0.15}_{-0.14}$ |
| −10.0 | $38.27^{+0.53}_{-0.55}$ | $38.96^{+0.35}_{-0.49}$ | $39.61^{+0.29}_{-0.44}$ | $40.25^{+0.26}_{-0.34}$ | $40.83^{+0.21}_{-0.20}$ | $41.35 \pm 0.14$ |
| −9.8 | $38.44^{+0.48}_{-0.57}$ | $39.13^{+0.35}_{-0.52}$ | $39.81^{+0.32}_{-0.46}$ | $40.45^{+0.28}_{-0.30}$ | $41.01^{+0.20}_{-0.18}$ | $41.52 \pm 0.14$ |
| −9.6 | $38.65^{+0.44}_{-0.60}$ | $39.35^{+0.37}_{-0.55}$ | $40.04^{+0.33}_{-0.42}$ | $40.66^{+0.27}_{-0.25}$ | $41.20^{+0.18}_{-0.16}$ | $41.70^{+0.14}_{-0.13}$ |
| −9.3 | $38.89^{+0.43}_{-0.61}$ | $39.61^{+0.38}_{-0.53}$ | $40.28^{+0.33}_{-0.37}$ | $40.87^{+0.24}_{-0.21}$ | $41.39^{+0.17}_{-0.15}$ | $41.89^{+0.14}_{-0.13}$ |
| −9.1 | $39.16^{+0.42}_{-0.60}$ | $39.88^{+0.38}_{-0.48}$ | $40.53^{+0.31}_{-0.29}$ | $41.08^{+0.21}_{-0.18}$ | $41.59^{+0.15}_{-0.14}$ | $42.09 \pm 0.13$ |
| −8.9 | $39.45^{+0.42}_{-0.58}$ | $40.15^{+0.37}_{-0.41}$ | $40.77^{+0.28}_{-0.23}$ | $41.29^{+0.19}_{-0.16}$ | $41.79^{+0.15}_{-0.14}$ | $42.29 \pm 0.13$ |
| −8.7 | $39.75^{+0.41}_{-0.52}$ | $40.42^{+0.34}_{-0.33}$ | $40.98^{+0.23}_{-0.20}$ | $41.50^{+0.17}_{-0.15}$ | $42.00^{+0.14}_{-0.13}$ | $42.50 \pm 0.13$ |
| −8.5 | $40.04^{+0.39}_{-0.45}$ | $40.67^{+0.30}_{-0.26}$ | $41.20^{+0.20}_{-0.17}$ | $41.71^{+0.15}_{-0.14}$ | $42.21^{+0.14}_{-0.13}$ | $42.71 \pm 0.13$ |

**Note.** The expected integrated XRB luminosity for a variety of sSFR (by row) and $M_\star$ (by column) values. Each quoted $L_X$ value represents the median expected from our global model, with error bars representing the 16% and 84% confidence values that are expected for a given combination of sSFR and $M_\star$. These values were obtained using the Monte Carlo simulations discussed in Section 5.2.

2. We report new fits to the XRB XLFs of all 38 galaxies in our sample, including estimates of CXB sources and the intrinsic source populations. We explore how the XLF normalizations, slopes, and calculated XRB luminosities depend on galaxy SFR and $M_\star$ (see Figure 5; Table 3). We find that the XLFs show a clear decline in normalization per unit SFR and a decrease in the $L > 10^{38}$ erg $s^{-1}$ XLF slope with increasing sSFR (i.e., SFR/$M_\star$), as the dominant XRB population shifts from LMXBs to HMXBs. As a corollary, the integrated XRB luminosity, $L_X$, per unit SFR declines with increasing sSFR (see Figure 6).
3. When analyzing XRB XLFs from subgalactic regions, selected in bins of sSFR, we clearly see the transition in XLF shape and normalization per SFR from the almost "pure" HMXB XLF at sSFR $\approx 5 \times 10^{-10}$ $yr^{-1}$ to the nearly pure LMXB XLF at sSFR $\approx 10^{-12}$ $yr^{-1}$ (see Figure 7). We present a global model that characterizes the scaling of the HMXB XLF with SFR and LMXB XLF with $M_\star$ that describes well the data for all 38 galaxies (model curves in Figures 7 and 9 and Table 4). The parameters of these models and uncertainties are determined using an MCMC procedure and are reported (see Figure 8 and Table 4).
4. We find basic agreement between the HMXB XLF shape and scaling with SFR, as presented in past papers (e.g., M12); however, our HMXB XLF reveals new complex features, beyond the previously reported power-law shape (see Figure 12(a)). These features include a steep power-law slope between $L \approx 10^{36}$ and $10^{38}$ erg $s^{-1}$, a "bump" or "flattening" between $L \approx 10^{38}$ and $10^{40}$ erg $s^{-1}$, and a rapid falloff at higher luminosities. These features are highly significant and are robustly identified in independent subsets of our data. Similar features have been reported in some XRB population synthesis models of the HMXB XLF.
5. We further find qualitatively good agreement between our LMXB XLF and the previously reported LMXB XLF from Z12, which was based on elliptical galaxies. However, our fits to the data, which are mainly driven by late-type galaxies, prefer a somewhat shallower slope at $L \gtrsim 10^{39}$ erg $s^{-1}$ and a steeper slope at $L \lesssim 10^{38}$ erg $s^{-1}$. We further find evidence that the LMXB XLF in higher-sSFR subsets is shallower at $L \gtrsim 10^{39}$ erg $s^{-1}$ and steeper at $L \lesssim 10^{38}$ erg $s^{-1}$ compared with our total-sample average (see Figure 12(b)). We speculate that this is plausibly due to a stellar age effect, in which the LMXB XLF is dominated by older stellar populations at low sSFR compared to those at high sSFR. This would imply that, compared to older LMXB XLFs, the LMXB XLF for younger populations contains excesses of LMXBs at all luminosities except $L \approx 10^{38}$–$10^{39}$ erg $s^{-1}$. Some features of this trend (e.g., more high-$L$ sources) have been predicted in population synthesis models.
6. We use our global model and Monte Carlo simulations to identify galaxies that have outlier XLF populations that are statistically significant. We identify four such galaxies: NGC 337, NGC 925, NGC 4552 (M89), and NGC 4559. Scrutiny of these objects indicates that NGC 337, NGC 925, and NGC 4559 are among the lowest-metallicity objects in our sample, and NGC 4552 contains a significant excess of GCs per unit optical

luminosity (i.e., specific frequency) over all other galaxies in our sample (Section 5.2).

7. To examine the effects of metallicity on the XLFs, we constructed the XLF for the lowest-metallicity galaxies in our sample (NGC 337, NGC 925, NGC 3198, NGC 4536, and NGC 4559). We find statistically significant evidence that the HMXB XLF in low-metallicity ($\approx 0.5 Z_{\odot}$) galaxies contains an excess of $L \gtrsim 10^{39}$ erg s$^{-1}$ sources, but comparable numbers of $\lesssim 10^{39}$ erg s$^{-1}$ sources, compared to the global average HMXB XLF for our sample, which has a median metallicity $\approx Z_{\odot}$ (see Figure 14). This result is in line with other studies that characterize how the integrated X-ray luminosity per SFR is anticorrelated with metallicity (e.g., Basu-Zych et al. 2016; Brorby et al. 2016). Our result provides a first characterization of the $\approx 0.5\ Z_{\odot}$ HMXB XLF from $\log L$ (ergs s$^{-1}$) = 37–41.
8. We conclude that our global model is appropriate for galaxies that are of roughly solar metallicity and have low GC specific frequencies. Finally, with this caveat, we use the global model, along with Monte Carlo simulations, to calculate the scatter in the integrated X-ray luminosities of HMXB and LMXB populations as a function of SFR and $M_{\star}$. Such a quantity is useful, for example, for X-ray data sets that detect only the total X-ray emission from the galaxy without resolving the XRB populations. We show that the median HMXB and LMXB integrated luminosities deviate substantially (by more than a factor of two) from the XLF-integrated average scaling relations, $L_{\rm X}$(HMXB)/SFR and $L_{\rm X}$(LMXB)/$M_{\star}$, at SFR $\lesssim 2\ M_{\odot}$ yr$^{-1}$ and $M_{\star} \lesssim 3 \times 10^{9}\ M_{\odot}$, respectively (see Figure 16). The corresponding 16%–84% scatter ranges from $\approx$0.3 to 0.7 dex for HMXBs across SFR = 0.1–10 $M_{\odot}$ yr$^{-1}$ and $\approx$0.2–0.4 for LMXBs across $\log M_{\star}(M_{\odot})$ = 9.5–11. Characterization of the XRB scatter is provided in Table 6.
9. Future investigations are underway to quantitatively assess how metallicity, stellar age, and GC specific frequency affect the XRB XLFs. These studies will provide expansive new constraints on close binary population synthesis models that are used to understand a variety of close binary populations (e.g., XRBs, gravitational-wave sources, and millisecond pulsars) and the role of XRBs in environments that are not yet observable (e.g., during the epoch of heating when HMXBs are thought to dominate the X-ray emissivity of the universe).

We thank the anonymous referee for their helpful suggestions, which have improved the quality of this paper. We gratefully acknowledge support from the National Aeronautics and Space Administration (NASA) Astrophysics Data Analysis Program (ADAP) grant NNX13AI48G (B.D.L., R.T.E., A.Z.) and Chandra X-ray Center grant GO8-19039X (B.D.L. and A. P.). A.Z. acknowledges funding from the European Union's Seventh Framework Programme (FP/2007–2013)/ERC grant agreement No. 617001.

Our work includes observations made with the NASA *Galaxy Evolution Explorer* (*GALEX*). *GALEX* is operated for NASA by the California Institute of Technology under NASA contract NAS5-98034. This publication makes use of data products from the Two Micron All Sky Survey, which is a joint project of the University of Massachusetts and the Infrared Processing and Analysis Center/California Institute of Technology, funded by NASA and the National Science Foundation (NSF). This work is based on observations made with the *Spitzer Space Telescope*, obtained from the NASA/IPAC Infrared Science Archive, both of which are operated by the Jet Propulsion Laboratory, California Institute of Technology, under a contract with the National Aeronautics and Space Administration.

*Facilities:* *Chandra*, *GALEX*, Sloan, 2MASS, *Spitzer*, *Herschel.*

*Software:* ACIS Extract (v2016sep22; Broos et al. 2010, 2012), MARX (v5.3.2; Davis et al. 2012), CIAO (v4.8; Fruscione et al. 2006), xspec (v12.9.1; Arnaud 1996).

## Appendix
## X-Ray Point-source Catalog

In Table 7, we provide the X-ray point-source catalogs, based on the analyses presented in Sections 3.2 and 3.3. The columns represent the following: Col. (1): name of the host galaxy. Col. (2): point-source identification number within the galaxy. Cols. (3) and (4): R.A. and decl. of the point source. Col. (5): offset of the point source with respect to the average aim point of the *Chandra* observations. Cols. (6) and (7): 0.5–7 keV net counts (i.e., background subtracted) and $1\sigma$ errors. Cols. (8)–(9) and (10)–(11): best-fit column density $N_{\rm H}$ and photon index $\Gamma$, respectively, along with their respective $1\sigma$ errors, based on spectral fits to an absorbed power-law model (`TBABS × POW` in `xspec`). For sources with small numbers of counts (<20 net counts), we adopted Galactic absorption appropriate for each galaxy and a photon index of $\Gamma = 1.7$. Cols. (12) and (13): the respective 0.5–8 keV flux and luminosity of the source. Col. (14): flag indicating the location of the source within the galaxy. Flag = 1 indicates that the source is within the $K_s$-band footprint adopted in Table 1 and outside a central region of avoidance, if applicable. All XLF calculations are based on Flag = 1 sources. Flag = 2 indicates that the source is within the $K_s$-band footprint but has a luminosity of $L < 10^{35}$ erg s$^{-1}$ and was thus excluded from our XLF analysis. Flag = 3 indicates that the source is outside the 20 mag arcsec$^{-2}$ $K_s$-band ellipse of the galaxy, but within the "total" $K_s$-band ellipse. Flag = 4 indicates that the source is located in the central region of avoidance owing to either the presence of an AGN or very high levels of source confusion. Flag = 5 indicates that the source is outside the "total" $K_s$-band ellipse.

**Table 7**
X-Ray Point-source Catalog and Properties

| Galaxy (1) | ID (2) | $\alpha_{J2000}$ (deg) (3) | $\delta_{J2000}$ (deg) (4) | $\theta$ (arcmin) (5) | $N_{FB}$ (counts) (6)–(7) | $N_H$ ($10^{22}$ cm$^{-2}$) (8)–(9) | $\Gamma$ (10)–(11) | log $F_{FB}$ (erg cm$^{-2}$ s$^{-1}$) (12) | log $L_{FB}$ (erg s$^{-1}$) (13) | Location Flag (14) |
|---|---|---|---|---|---|---|---|---|---|---|
| NGC 337 | 1 | 00 59 43.53 | −07 35 01.33 | 1.7 | 7.8 ± 4.2 | 0.056 | 1.7 | −14.1 | 38.6 | 4 |
| | 2 | 00 59 47.50 | −07 34 16.68 | 0.8 | 41.0 ± 7.9 | 0.109 ± 0.154 | <3.06 | −13.7 | 39.1 | 2 |
| | 3 | 00 59 48.51 | −07 34 56.71 | 0.5 | 65.3 ± 9.7 | 0.314 ± 0.381 | 1.98 ± 0.74 | −13.2 | 39.5 | 1 |
| | 4 | 00 59 49.48 | −07 34 35.66 | 0.2 | 106.8 ± 12.1 | 0.308 ± 0.326 | 1.60 ± 0.53 | −13.0 | 39.8 | 1 |
| | 5 | 00 59 49.49 | −07 35 23.53 | 0.7 | 22.3 ± 6.2 | 0.779 ± 0.410 | <3.06 | −13.8 | 38.9 | 2 |
| | 6 | 00 59 50.40 | −07 34 45.67 | 0.1 | 4.7 ± 2.2 | 0.056 | 1.7 | −14.3 | 38.5 | 1 |
| | 7 | 00 59 50.40 | −07 34 54.18 | 0.2 | 42.8 ± 8.1 | 0.647 ± 0.796 | 1.57 ± 0.90 | −13.3 | 39.5 | 1 |
| | 8 | 00 59 50.56 | −07 34 58.08 | 0.3 | 300.5 ± 19.5 | 0.136 ± 0.155 | 1.40 ± 0.29 | −12.5 | 40.3 | 1 |
| | 9 | 00 59 51.90 | −07 34 57.71 | 0.5 | 14.4 ± 5.2 | 0.056 | 1.7 | −13.8 | 39.0 | 1 |
| | 10 | 00 59 52.29 | −07 34 47.38 | 0.6 | 43.3 ± 8.1 | 0.405 ± 0.510 | 2.17 ± 0.97 | −13.4 | 39.3 | 2 |
| | 11 | 00 59 53.31 | −07 34 56.49 | 0.8 | 4.9 ± 2.2 | 0.056 | 1.7 | −14.3 | 38.5 | 2 |
| | 12 | 00 59 53.32 | −07 35 20.76 | 1.0 | 27.3 ± 6.7 | 0.477 ± 0.787 | 1.67 ± 1.12 | −13.5 | 39.2 | 2 |
| NGC 584 | 1 | 01 31 09.45 | −06 54 34.08 | 3.7 | 12.1 ± 4.9 | 0.036 | 1.7 | −13.8 | 38.9 | 4 |
| | 2 | 01 31 17.83 | −06 54 34.75 | 2.6 | 5.9 ± 2.4 | 0.036 | 1.7 | −14.1 | 38.6 | 4 |
| | 3 | 01 31 18.02 | −06 51 48.29 | 0.7 | 8.8 ± 4.4 | 0.036 | 1.7 | −13.8 | 38.9 | 1 |
| | 4 | 01 31 18.73 | −06 52 06.49 | 0.5 | 1.9 ± 1.4 | 0.036 | 1.7 | −14.5 | 38.1 | 1 |
| | 5 | 01 31 19.28 | −06 51 50.26 | 0.4 | 3.9 ± 2.0 | 0.036 | 1.7 | −14.2 | 38.4 | 1 |
| | 6 | 01 31 19.54 | −06 52 03.87 | 0.3 | 2.9 ± 1.7 | 0.036 | 1.7 | −14.4 | 38.3 | 1 |
| | 7 | 01 31 20.00 | −06 52 07.07 | 0.2 | 19.6 ± 5.9 | 0.036 | 1.7 | −13.6 | 39.1 | 1 |
| | 8 | 01 31 20.14 | −06 51 41.03 | 0.4 | 3.9 ± 2.0 | 0.036 | 1.7 | −13.9 | 38.8 | 1 |

**Note.** The full version of this table contains 4442 sources. An abbreviated version of the table is displayed here to illustrate its form and content. A description of the columns is provided in the Appendix.

(This table is available in its entirety in machine-readable form.)

## ORCID iDs

Bret D. Lehmer https://orcid.org/0000-0003-2192-3296
Rafael T. Eufrasio https://orcid.org/0000-0002-2987-1796
Panayiotis Tzanavaris https://orcid.org/0000-0001-5737-5055
Andreas Zezas https://orcid.org/0000-0001-8952-676X
Andrew Ptak https://orcid.org/0000-0001-5655-1440

## References

Abbott, B. P., Abbott, R., Abbott, T. D., et al. 2016, PhRvL, 116, 061102
Abbott, B. P., Abbott, R., Abbott, T. D., et al. 2017, PhRvL, 119, 161101
Aird, J., Coil, A. L., & Georgakakis, A. 2017, MNRAS, 465, 3390
Anastasopoulou, K., Zezas, A., Gkiokas, V., & Kovlakas, K. 2019, MNRAS, 483, 711
Antoniou, V., & Zezas, A. 2016, MNRAS, 459, 528
Antoniou, V., Zezas, A., Drake, J. J., et al. 2019, arXiv:1901.01237
Arnaud, K. A. 1996, in ASP Conf. Ser. 101, Astronomical Data Analysis Software and Systems V, ed. G. H. Jacoby & J. Barnes (San Francisco, CA: ASP), 17
Artale, M. C., Giacobbo, N., Mapelli, M., & Esposito, P. 2018, arXiv:1811.06291
Basu-Zych, A. R., Lehmer, B., Fragos, T., et al. 2016, ApJ, 818, 140
Basu-Zych, A. R., Lehmer, B. D., Hornschemeier, A. E., et al. 2013a, ApJ, 774, 152
Basu-Zych, A. R., Lehmer, B. D., Hornschemeier, A. E., et al. 2013b, ApJ, 762, 45
Bekki, K., Yahagi, H., & Forbes, D. A. 2006, ApJL, 645, L29
Belczynski, K., Askar, A., Arca-Sedda, M., et al. 2018, A&A, 615, A91
Belczynski, K., Holz, D. E., Bulik, T., & O'Shaughnessy, R. 2016, Natur, 534, 512
Bell, E. F. 2003, ApJ, 586, 794
Bell, E. F., & de Jong, R. S. 2001, ApJ, 550, 212
Blanton, M. R., Hogg, D. W., Bahcall, N. A., et al. 2003, ApJ, 592, 819
Blanton, M. R., & Moustakas, J. 2009, ARA&A, 47, 159
Boroson, B., Kim, D.-W., & Fabbiano, G. 2011, ApJ, 729, 12
Bresolin, F., Ryan-Weber, E., Kennicutt, R. C., & Goddard, Q. 2009, ApJ, 695, 580
Brodie, J. P., & Strader, J. 2006, ARA&A, 44, 193
Broos, P. S., Townsley, L. K., Feigelson, E. D., et al. 2010, ApJ, 714, 1582
Broos, P. S., Townsley, L. K., Getman, K. V., & Bauer, F. E. 2012, AE: ACIS Extract, Astrophysics Source Code Library, ascl:1203.001
Brorby, M., Kaaret, P., & Prestwich, A. 2014, MNRAS, 441, 2346
Brorby, M., Kaaret, P., Prestwich, A., & Mirabel, I. F. 2016, MNRAS, 457, 4081
Cash, W. 1979, ApJ, 228, 939
Cheng, Z., Li, Z., Xu, X., & Li, X. 2018a, ApJ, 858, 33
Cheng, Z., Li, Z., Xu, X., et al. 2018b, ApJ, 869, 52
Clark, G. W. 1975, ApJL, 199, L143
Colbert, E. J. M., Heckman, T. M., Ptak, A. F., Strickland, D. K., & Weaver, K. A. 2004, ApJ, 602, 231
Das, A., Mesinger, A., Pallottini, A., Ferrara, A., & Wise, J. H. 2017, MNRAS, 469, 1166
Davis, J. E., Bautz, M. W., Dewey, D., et al. 2012, Proc. SPIE, 8443, 84431A
de Vaucouleurs, G., de Vaucouleurs, A., Corwin, H. G., Jr., et al. 1991, Third Reference Catalogue of Bright Galaxies, Vol. I, II, and III (New York: Springer)
Dickey, J. M., & Lockman, F. J. 1990, ARA&A, 28, 215
Douna, V. M., Pellizza, L. J., Mirabel, I. F., & Pedrosa, S. E. 2015, A&A, 579, A44
Elbaz, D., Daddi, E., Le Borgne, D., et al. 2007, A&A, 468, 33
Eufrasio, R. T., Lehmer, B. D., Zezas, A., et al. 2017, ApJ, 851, 10
Fabian, A. C., Pringle, J. E., & Rees, M. J. 1975, MNRAS, 172, 15p
Fornasini, F. M., Civano, F., Fabbiano, G., et al. 2018, ApJ, 865, 43
Fragos, T., Kalogera, V., Belczynski, K., et al. 2008, ApJ, 683, 346
Fragos, T., Lehmer, B., Tremmel, M., et al. 2013a, ApJ, 764, 41
Fragos, T., Lehmer, B. D., Naoz, S., Zezas, A., & Basu-Zych, A. 2013b, ApJL, 776, L31
Fruscione, A., McDowell, J. C., Allen, G. E., et al. 2006, Proc. SPIE, 6270, 62701V
Galametz, M., Kennicutt, R. C., Calzetti, D., et al. 2013, MNRAS, 431, 1956
Garofali, K., Williams, B. F., Hillis, T., et al. 2018, MNRAS, 479, 3526
Gehrels, N. 1986, ApJ, 303, 336
Georgakakis, A., Nandra, K., Laird, E. S., Aird, J., & Trichas, M. 2008, MNRAS, 388, 1205
Gilfanov, M. 2004, MNRAS, 349, 146
Gilfanov, M., Grimm, H.-J., & Sunyaev, R. 2004, MNRAS, 351, 1365
Greig, B., & Mesinger, A. 2018, MNRAS, 477, 3217
Grimm, H.-J., Gilfanov, M., & Sunyaev, R. 2003, MNRAS, 339, 793

Guo, Q., White, S., Boylan-Kolchin, M., et al. 2011, MNRAS, 413, 101
Hao, C.-N., Kennicutt, R. C., Johnson, B. D., et al. 2011, ApJ, 741, 124
Harris, W. E. 1991, ARA&A, 29, 543
Harris, W. E., Harris, G. L. H., & Alessi, M. 2013, ApJ, 772, 82
Hastings, W. K. 1970, Biometrika, 57, 97
Hickox, R. C., & Alexander, D. M. 2018, ARA&A, 56, 625
Hu, N., Wang, E., Lin, Z., et al. 2018, ApJ, 854, 68
Irwin, J. A. 2005, ApJ, 631, 511
Jarrett, T. H., Chester, T., Cutri, R., Schneider, S. E., & Huchra, J. P. 2003, AJ, 125, 525
Juett, A. M. 2005, ApJL, 621, L25
Justham, S., & Schawinski, K. 2012, MNRAS, 423, 1641
Kaaret, P. 2014, MNRAS, 440, L26
Kaaret, P., Schmitt, J., & Gorski, M. 2011, ApJ, 741, 10
Kaastra, J. S. 2017, A&A, 605, A51
Karim, A., Schinnerer, E., Martínez-Sansigre, A., et al. 2011, ApJ, 730, 61
Kennicutt, R. C., & Evans, N. J. 2012, ARA&A, 50, 531
Kennicutt, R. C., Jr., Armus, L., Bendo, G., et al. 2003, PASP, 115, 928
Kewley, L. J., & Ellison, S. L. 2008, ApJ, 681, 1183
Kim, D.-W., & Fabbiano, G. 2004, ApJ, 611, 846
Kim, D.-W., & Fabbiano, G. 2010, ApJ, 721, 1523
Kim, D.-W., Fabbiano, G., Brassington, N. J., et al. 2009, ApJ, 703, 829
Kim, M., Wilkes, B. J., Kim, D.-W., et al. 2007, ApJ, 659, 29
Kobulnicky, H. A., & Kewley, L. J. 2004, ApJ, 617, 240, (KK04)
Kroupa, P. 2001, MNRAS, 322, 231
Kruckow, M. U., Tauris, T. M., Langer, N., Kramer, M., & Izzard, R. G. 2018, MNRAS, 481, 1908
Kuntz, K. D., & Snowden, S. L. 2010, ApJS, 188, 46
Lehmer, B. D., Alexander, D. M., Bauer, F. E., et al. 2010, ApJ, 724, 559
Lehmer, B. D., Basu-Zych, A. R., Mineo, S., et al. 2016, ApJ, 825, 7
Lehmer, B. D., Berkeley, M., Zezas, A., et al. 2014, ApJ, 789, 52
Lehmer, B. D., Brandt, W. N., Alexander, D. M., et al. 2007, ApJ, 657, 681
Lehmer, B. D., Eufrasio, R. T., Markwardt, L., et al. 2017, ApJ, 851, 11
Linden, T., Kalogera, V., Sepinsky, J. F., et al. 2010, ApJ, 725, 1984
Long, K. S., Kuntz, K. D., Blair, W. P., et al. 2014, ApJS, 212, 21
Madau, P., & Fragos, T. 2017, ApJ, 840, 39
Mandel, I., & de Mink, S. E. 2016, MNRAS, 458, 2634
Mapelli, M., & Giacobbo, N. 2018, MNRAS, 479, 4391
Mapelli, M., Ripamonti, E., Zampieri, L., Colpi, M., & Bressan, A. 2010, MNRAS, 408, 234
Marchant, P., Langer, N., Podsiadlowski, P., et al. 2017, A&A, 604, A55
McQuinn, K. B. W., Skillman, E. D., Dolphin, A. E., Berg, D., & Kennicutt, R. 2016, ApJ, 826, 21
Mesinger, A., Ferrara, A., & Spiegel, D. S. 2013, MNRAS, 431, 621
Mineo, S., Gilfanov, M., & Sunyaev, R. 2012a, MNRAS, 419, 2095, (M12)
Mineo, S., Gilfanov, M., & Sunyaev, R. 2012b, MNRAS, 426, 1870
Mirabel, I. F., Dijkstra, M., Laurent, P., Loeb, A., & Pritchard, J. R. 2011, A&A, 528, 149
Miralles-Caballero, D., Díaz, A. I., Rosales-Ortega, F. F., Pérez-Montero, E., & Sánchez, S. F. 2014, MNRAS, 440, 2265
Moustakas, J., Kennicutt, R. C., Jr., Tremonti, C. A., et al. 2010, ApJS, 190, 233
Nataf, D. M. 2015, MNRAS, 449, 1171
Noeske, K. G., Weiner, B. J., Faber, S. M., et al. 2007, ApJL, 660, L43
Pacucci, F., Mesinger, A., Mineo, S., & Ferrara, A. 2014, MNRAS, 443, 678
Peacock, M. B., Zepf, S. E., Kundu, A., et al. 2017, ApJ, 841, 28
Peng, E. W., Jordán, A., Côté, P., et al. 2008, ApJ, 681, 197
Pettini, M., & Pagel, B. E. J. 2004, MNRAS, 348, L59, (PP04)
Prestwich, A. H., Tsantaki, M., Zezas, A., et al. 2013, ApJ, 769, 92
Ranalli, P., Comastri, A., & Setti, G. 2003, A&A, 399, 39
Salpeter, E. E. 1955, ApJ, 121, 161
Sazonov, S., & Khabibullin, I. 2017a, MNRAS, 466, 1019
Sazonov, S., & Khabibullin, I. 2017b, MNRAS, 468, 2249
Sivakoff, G. R., Jordán, A., Sarazin, C. L., et al. 2007, ApJ, 660, 1246
Tuffs, R. J., Popescu, C. C., Völk, H. J., Kylafis, N. D., & Dopita, M. A. 2004, A&A, 419, 821
Tully, R. B., Courtois, H. M., Dolphin, A. E., et al. 2013, AJ, 146, 86
Tzanavaris, P., Fragos, T., Tremmel, M., et al. 2013, ApJ, 774, 136
Tzanavaris, P., Hornschemeier, A. E., Gallagher, S. C., et al. 2016, ApJ, 817, 95
Voss, R., Gilfanov, M., Sivakoff, G. R., et al. 2009, ApJ, 701, 471
Whitaker, K. E., Franx, M., Leja, J., et al. 2014, ApJ, 795, 104
Zhang, Z., Gilfanov, M., & Bogdán, Á. 2012, A&A, 546, A36, (Z12)
Zibetti, S., Charlot, S., & Rix, H.-W. 2009, MNRAS, 400, 1181
Zuo, Z.-Y., Li, X.-D., & Gu, Q.-S. 2014, MNRAS, 437, 1187